People's Democratic Republic of Algeria
Ministry of Higher Education and Scientific Research
Abderrahmane Mira University of Bejaia

جامعة بجاية
Tasdawit n Bgayet
Université de Béjaïa

Faculty of Technology
Electrical Engineering Department
Industrial Technology and Information Laboratory (LTII)

THESIS WITH A VIEW TOWARDS OBTAINING THE DIPLOMA OF DOCTORATE

Domain: Science and Technology Branch: Electromechanical
Specialty: Electromechanical

Presented by
SAYEH Karim Fathi

Theme

CONTRIBUTION TO THE DEVELOPMENT OF CONTROL ALGORITHMS FOR THE CONTROL OF RENEWABLE ENERGY SYSTEMS

Defended on: July 10,2025 **In front of the Jury composed of:**

Last and first name	**Grade**		
Mr REKIOUA Toufik	Professor	Univ. of Bejaia	President
Mr TAMALOUZT Salah	Professor	Univ. of Bejaia	Supervisor
Mr ZIANE Djamel	MCB	Univ. of Tizi Ouzou	Co-Supervisor
Mr CHAIBA Azeddine	Professor	Univ. of Batna2	Examiner
Mr HAMOUDI Farid	Professor	Univ. of Bejaia	Examiner
Mr DJERMOUNI Kamel	MCA	Univ. of Bejaia	Examiner

University year : 2024/2025

République Algérienne Démocratique et Populaire
Ministère de l'Enseignement Supérieur et de la Recherche Scientifique
Université A.MIRA-BEJAIA

جامعة بجاية
Tasdawit n Bgayet
Université de Béjaïa

Faculté de Technologie
Département de Génie Électrique
Laboratoire de Technologie Industrielle et de l'Information (LTII)

THÈSE EN VUE DE L'OBTENTION DU DIPLOME DE DOCTORAT

Domaine : Sciences et Technologies Filière : Électromécanique
Spécialité : Électromécanique

Présentée par
SAYEH Karim Fathi

Thème

CONTRIBUTION AU DÉVELOPPEMENT D'ALGORITHMES DE COMMANDE POUR LE CONTRÔLE DES SYSTÈMES D'ÉNERGIES RENOUVELABLES

Soutenue le : 10 juillet 2025 **Devant le Jury composé de :**

Nom et Prénom	**Grade**		
Mr REKIOUA Toufik	Professeur	Univ. de Bejaia	President
Mr TAMALOUZT Salah	Professeur	Univ. de Bejaia	Rapporteur
Mr ZIANE Djamel	MCB	Univ. de Tizi Ouzou	Co-Rapporteur
Mr CHAIBA Azeddine	Professeur	Univ. de Batna2	Examinateur
Mr HAMOUDI Farid	Professeur	Univ. de Bejaia	Examinateur
Mr DJERMOUNI Kamel	MCA	Univ. de Bejaia	Examinateur

Année Universitaire : 2024/2025

ACKNOWLEDGEMENT

I begin by expressing my profound gratitude to **Allah** for granting me the faith, patience, perseverance, and courage necessary to embark upon and complete this challenging yet rewarding endeavor. All praise and thanks belong to Him.

This doctoral journey, culminating in the completion of this thesis, has been profoundly shaped by the guidance, support, and encouragement of many esteemed individuals. I am deeply grateful for their invaluable contributions.

My foremost gratitude goes to my principal supervisor, **Prof. Salah Tamalouzt**. His unwavering guidance, profound intellectual insights, and steadfast belief in my potential were the cornerstones of this research. He not only illuminated complex pathways but also instilled in me a deeper understanding and passion for the subject, transforming what could have been arduous into an enriching and stimulating endeavor. His mentorship has been pivotal to my academic and personal development.

I am equally indebted to my co-supervisor, **Dr. Djamel Ziane**, whose timely involvement during my third year proved instrumental in the successful completion of this dissertation. His generous support, unparalleled hospitality, and meticulous guidance during my research period in France were truly indispensable. He created a welcoming and supportive environment that facilitated my work and made my experience abroad incredibly productive.

My sincere appreciation extends to the esteemed members of my defense jury: **Prof. Toufik Rekioua** for graciously agreeing to chair, and **Prof**. **Farid Hamoudi, Dr**. **Kamel Djermouni and Prof. Azeddine Chaiba** for dedicating their valuable time to review this manuscript and providing insightful critiques and constructive feedback that significantly enhanced its quality.

I am also profoundly grateful to all the university professors whose inspiring lectures and profound knowledge laid the foundation for my academic curiosity. A special mention of thanks to **Prof. Sofia Lalouni Belaid** and **Prof. Djamal Aouzellag** for their consistent encouragement and support throughout my studies.

The collaborative spirit and technical assistance provided by the members of the IREENA laboratory were invaluable. I extend my particular thanks to **Dr. Houari Azeddine**, **Dr. Mohamed Fouad Benkhoris**, **Dr. Abdelhakim Saim**, and **Dr. Seydali Ferahtia** for their expertise, the generous sharing of resources and equipment, and their insightful advice, which were crucial to the practical aspects of my research.

Furthermore, I extend my heartfelt appreciation to **Dr. Ahmed Mouissi, Dr. Abdellah Bekhiti, Dr. Youcef Belkhier,** and **Dr. Younes Sahri**. Their insightful contributions and dedicated support were pivotal in enhancing my research articles and facilitating their publication in high-impact journals. Their expertise in this regard has been invaluable.

Finally, this journey would have been impossible without the unwavering love, endless sacrifices, and steadfast encouragement of **my Beloved Parents**. Their unwavering belief in my abilities and their constant support have been a boundless source of strength. My profound gratitude also goes to my family and friends, whose patience, understanding, and encouragement were vital throughout this process. To every individual who offered a kind word, a supportive smile, or a heartfelt prayer, your gestures, big or small, were deeply cherished and profoundly appreciated.

إهداء

اللهم لك الحمد على توفيقك،

اللهم لك الحمد على نعمك التي لا تُعد ولا تُحصى،

اللهم لك الحمد حمدًا يليق بجلال وجهك وعظيم سلطانك.

إلى أمي الغالية، التي ربتني وغمرتني بحنانها، وغرست في نفسي معاني الحياة.

إلى أبي العزيز، الذي بذل من أجلي الجهد والسهر والتضحية.

إلى إخوتي وأخواتي الأحباء: محمد الأمين، نور الإسلام، نسرين، وريمة، الذين كانوا دوما سندي، ودعموني بكل حب وصدق.

إلى أقاربي الكرام، الذين كان لوجودهم ودعائهم الصادق الأثر الكبير في نفسي.

إلى أصدقائي الأوفياء، الذين لم يتخلّوا عني وشاركوا مسيرتي بحب،

وخاصة: **العربي ميلود، بخيتي عبدالله، عيدي موسى، عيساوي جمال، قواس بهاء، مويسي أحمد، ونجمة عبد اللطيف.**

وإلى الأصدقاء الذين تعرفت عليهم خلال رحلتي هذه،

وبشكل خاص: **عيساوي أحمد، دفاف إبراهيم،خذيري توفيق، عبد العزيز الحسن والحسين، وبلحوي ياسين.**

أهدي هذا العمل المتواضع لكل من ساندني، وأتقدم إليهم جميعا بخالص الشكر والامتنان.

LIST OF SCIENTIFIC CONTRIBUTIONS

[1] **K. F. Sayeh**, S. Tamalouzt, D. Ziane, N. Benyahia, S. Lalouni Belaid, and Y. Belkhier. "Real-time fuzzy logic-based direct power control for wind energy systems." Engineering Applications of Artificial Intelligence 154 (2025): 110968. Doi: https://doi.org/10.1016/j.engappai.2025.110968 [**IF: 7.5, Q1**]

[2] **K. F. Sayeh**, S. Tamalouzt, Y. Sahri, S. Lalouni Belaid, and A. Bekhiti, Artificial Intelligence-Based Direct Power Control for Power Quality Improvement in a WT-DFIG System via Neural Networks: Prediction and Classification Techniques, Journal of the Franklin Institute, 362 (1), 107401, 2025. Doi: https://doi.org/10.1016/j.jfranklin.2024.107401 [**IF: 3.7, Q1**]

[3] **K. F. Sayeh**, S. Tamalouzt, D. Ziane, A. Bekhiti, and Y. Belkhier, Utilizing Fuzzy Logic Control and Neural Networks Based on Artificial Intelligence Techniques to Improve Power Quality in Doubly Fed Induction Generator-Based Wind Turbine System, International Journal of Energy Research, 2025 (1), 5985904. Doi: https://doi.org/10.1155/er/5985904 [**IF: 4.3, Q1**]

[4] **K. F. Sayeh,** S. Tamalouzt, D. Ziane, B. Deffaf, S. Lalouni Belaid, Y. Belkhier, M. Bajaj, and V. Blazek, Fuzzy Logic-Enhanced Direct Power Control for Wind Turbines with Doubly Fed Induction Generators, Results in Engineering, 5, 103557, 2024. Doi: https://doi.org/10.1016/j.rineng.2024.103557 [**IF: 6.0, Q1**]

[5] A. Lahlou, S. Tamalouzt, K. Djermouni, and **K. F. Sayeh,** Enhancing Photovoltaic Array Performance through Optimizing Power during Mismatch Conditions under Series-parallel (SP) and Total Cross-Tied (TCT) Configurations, Journal of Renewable Energies, 1, 1, pp. (79–86), 2024. Doi: https://doi.org/10.54966/jreen.v1i1.1176 [**IF: /, Q4**]

[6] **K. F. Sayeh,** S. Tamalouzt, D. Ziane, Y. Sahri, B. Deffaf, and S. Lalouni Belaid, Control of a Wind Turbine based on DFIG by Improved Direct Torque Control using Fuzzy Logic, Journal of Renewable Energies, 1, 1, pp. (71–78), 2024. Doi: https://doi.org/10.54966/jreen.v1i1.1173 [**IF: /, Q4**]

[7] **K. F. Sayeh,** S. Tamalouzt, and Y. Sahri, Improvement of power quality in WT-DFIG systems using novel direct power control based on fuzzy logic control under randomness conditions, International Journal of Modelling and Simulation, pp. (1-13), 2023. Doi: https://doi.org/10.1080/02286203.2023.2270757 [**IF: /, Q1**]

TABLE OF CONTENTS

Acknowledgement i
Dedication ii
List of Scientific Contributions iii
Table of Contents iv
Table of Figures vii
Table of Tables xi
List of Abbreviations and Symbols xii
General Introduction 1

Context and Motivation 1
Research Objectives and Contributions 2
Thesis Organization 3

I Introduction to Renewable Energy Systems and Advanced Control Strategies 6

I.1. Introduction 6
I.2. Global Energy Challenges and the Renewable Imperative 6
I.2.1. Historical Perspective 6
I.2.2. The Renewable Energy Transition 7
I.2.3. Motivation for AI-Based Control Strategies 8
I.3. Overview of Renewable Energy Sources 9
I.3.1. Wind Energy 9
I.3.2. Solar Energy 12
I.3.3. Integration of Renewable Energy Systems into Microgrids 15
I.4. Fuel Cells 15
I.4.1. Working Principle 16
I.4.2. Types of Fuel Cells 16
I.5. Energy Storage Systems 17
I.5.1. Electrochemical Storage (Batteries) 17
I.5.2. Overview of Other Energy Storage System Technologies 18
I.6. DFIG-Based Wind Energy Systems and Control Challenges 20
I.6.1. System Components and Advantages 20
I.6.2. Limitations of Classical Control Strategies 21
I.6.3. AI-Based Control Strategies for DFIG Systems 22
I.7. Microgrids 22
I.7.1. Microgrid Operating Modes 23
I.7.2. Microgrid Configurations 23
I.7.3. Energy Management Systems 24
I.8. Studied DC-Microgrid Configuration 24
I.8.1. Literature Review on DC-Microgrid 25
I.8.2. Proposed DC-Microgrid System 25
I.9. Conclusion 27

II Modeling of Microgrid Components 28

II.1. Introduction 28
II.2. Wind Turbine Based on Double Fed Induction Generator Modeling 28
II.2.1. Mechanical Subsystem Modeling 28
II.2.2. Electrical Subsystem Modeling 32
II.3. Photovoltaic System Modeling 36
II.3.1. PV Cell Equivalent Circuit Model 36
II.3.2. Main Operational Parameters: Short-Circuit Current and Open-Circuit Voltage 37
II.3.3. PV Module and Array Modeling 38
II.3.4. Effect of Environmental Parameters 39

II.4. Battery Energy Storage System Modeling 39
II.4.1. RC Equivalent Circuit Model 40
II.4.2. State of Charge 41
II.5. Fuel Cell System Modeling 41
II.5.1. PEMFC Electrochemical Model 42
II.5.2. Fuel Cell Stack 44
II.6. Power Converter Modeling 44
II.6.1. AC/DC/AC Back-to-Back Converter Model 44
II.6.2. DC/DC Converters 45
II.7. Conclusion 47
III Classical Control Strategies for DFIG-Based Wind Turbine Systems 48
III.1. Introduction 48
III.2. System Configuration and Overall Control Structure 49
III.3. Wind Power Optimization and Limitation Control 50
III.3.1. Turbine Operation Zones 50
III.3.2. Maximum Power Point Tracking 50
III.3.3. Pitch Angle Control 51
III.4. Classical Control of the Rotor Side Converter using C-DPC 51
III.4.1. Control Objectives and Strategy 52
III.4.2. Principle of Direct Power Control 52
III.4.3. Implementation Components 55
III.4.4. Advantages and Disadvantages 57
III.5. Classical Control of the Grid Side Converter using C-DPC 57
III.5.1. Control Objectives and Strategy 58
III.5.2. Principle of Direct Power Control 59
III.5.3. Implementation Components 60
III.6. Simulation Results and Performance Analysis of the Classical System 61
III.7. Critical Analysis of the Classical Control System 66
III.8. Conclusion 67
IV AI-Enhanced Direct Power Control of WT-DFIG Rotor Side Converter 68
IV.1. Introduction 68
IV.2. Fundamentals of Fuzzy Logic 70
IV.2.1. Fuzzy Sets and Membership Functions 70
IV.2.2. FLC Architecture and Operation 71
IV.2.3. Fuzzy Logic Suitability for DPC Enhancement 73
IV.3. Fundamentals of Artificial Neural Networks 73
IV.3.1. Data Preparation and Input Scaling 74
IV.3.2. Neuron Model and Feed forward 75
IV.3.3. Activation Functions 75
IV.3.4. Backpropagation 76
IV.3.5. ANN Suitability for DPC Enhancement 77
IV.4. AI-Enhanced DPC Strategy 1: Hysteresis Comparators Replacement 77
IV.4.1. Fuzzy Hysteresis DPC (FH-DPC) 77
IV.4.2. Neural Hysteresis DPC (NH-DPC) 80
IV.5. AI-Enhanced DPC Strategy 2: Direct Voltage Vector Selection 82
IV.5.1. Prediction Neural Network DPC (PNN-DPC) 82
IV.5.2. Classification Neural Network DPC (CNN-DPC) 84
IV.6. Comprehensive Performance Evaluation and Comparative Analysis 87
IV.6.1. Simulation Setup 87
IV.6.2. Scenario 1: Step Wind Profile Analysis (Reference Tracking) 87
IV.6.3. Scenario 2: Random Wind Profile Analysis (Robustness) 95
IV.6.4. Discussion on Performance, Implementation, and Trade-offs 99

IV.7. Conclusion 100
V Management and Control of the proposed DC-Microgrid 102
V.1. Introduction 102
V.2. Detailed DC-Microgrid System Description 103
V.2.1. Overall Topology and Component Interconnections 103
V.2.2. Control Hierarchy Overview 104
V.3. Component Description and Sizing 105
V.3.1. Wind Turbine System: Description and Sizing 105
V.3.2. Photovoltaic System: Description and Sizing 106
V.3.3. Battery Energy Storage System : Description and Sizing 107
V.3.4. Fuel Cell System: Description and Sizing 108
V.3.5. DC Load Profile: Description and Parameters 109
V.4. Local Control Strategies for Individual Microgrid Components 109
V.4.1. Wind Turbine Based On DFIG System Control 109
V.4.2. Photovoltaic System MPPT Control 112
V.4.3. Battery Energy Storage System Control 113
V.4.4. Fuel Cell System Control 115
V.5. Energy Management System Design 115
V.6. Results and Discussion 118
V.7. Conclusion 123
General Conclusion and Perspectives 126
References 129
Appendix 139

TABLE OF FIGURES

Figure I-1:Global Energy Consumption by Source (1965-2023) [13]..... 7
Figure I-2:Global Installed Electricity Capacity by Technology (2000-2024)[20]. 8
Figure I-3: Process of Horizontal-Axis Wind Turbine Operation. 9
Figure I-4: Types of Wind Turbines. 10
Figure I-5: AC grid-connected wind turbine generator configurations— (a) Doubly-Fed Induction Generator (DFIG), (b) Permanent Magnet Synchronous Generator (PMSG), (c) Squirrel Cage Induction Generator (SCIG). 12
Figure I-6: Working principle of the PV cell. 13
Figure I-7: Solar PV System Configurations. 15
Figure I-8 : Fuel cell working principle. 16
Figure I-9 : Basic working principle of a battery. 17
Figure I-10 : Microgrid Configuration. 22
Figure I-11: Proposed DC Microgrid. 26
Figure II-1: Schematic of Wind Turbine Mechanical Components 29
Figure II-2: Characteristic Power Coefficient (Cp) Curves as a Function of Tip-Speed Ratio (λ) and Pitch Angle (β). 30
Figure II-3 : Simplified Drivetrain Model. 31
Figure II-4:Block Diagram Representation of the Wind Energy Conversion System (WECS) Mechanical Model. 31
Figure II-5: Schematic Diagram of Doubly-Fed Induction Generator (DFIG) Windings. 32
Figure II-6 : Single-Diode Equivalent Circuit Model of a Photovoltaic (PV) Cell. 36
Figure II-7: Typical I-V and P-V Characteristic Curves of a PV cell. 38
Figure II-8 : Influence of (a) Irradiance and (b) Temperature on PV cell I-V Characteristics. 38
Figure II-9 : Hierarchical Structure of a Photovoltaic System (Cell, Module, Array). 39
Figure II-10 :First-Order RC (Thevenin) Equivalent Circuit Model of a Battery. 40
Figure II-11 : Battery State of Charge (SOC) Levels and Recommended Operating Range. 41
Figure II-12 :Equivalent Electrical Circuit Model of a PEM Fuel Cell. 42
Figure II-13 : AC/DC/AC Back-to-Back Converter Configuration for DFIG. 44
Figure II-14 : DC/DC Boost Converter Circuit Topology. 46
Figure II-15 : Bidirectional DC/DC Converter Topology. 46

Figure III-1 : Overall Classical Control System Architecture. 49
Figure III-2 : Wind Turbine Operating Zones. 50
Figure III-3 : Block Diagram of RSC C-DPC Implementation. 52
Figure III-4 : Vectors of output rotor voltage for GSC. 55
Figure III-5 : RSC Active and reactive powers hysteresis comparators output errors. 56
Figure III-6 : Block Diagram of GSC C-DPC Implementation. 58
Figure III-7 : Vectors of output rotor voltage for GSC. 60
Figure III-8 : GSC Active and reactive powers hysteresis comparators output errors. 61
Figure III-9: Wind and DFIG speed 62
Figure III-10 : Cp, λ and β 63
Figure III-11 :Generated active power 63
Figure III-12 : Local reactive power. 64
Figure III-13 : DC link voltage. 64
Figure III-14 : Grid active power. 65
Figure III-15 : Grid reactive power. 65
Figure III-16 : Stator current waveforms. Figure III-17: Rotor current waveforms. 66
Figure III-18 : Grid current exchanged with the AC grid via the GSC waveforms. 66
Figure IV-1 : FL Architecture Block Diagram. 71
Figure IV-2: General architecture of a multi-input and multi-output neural network. 74
Figure IV-3 Operating principle of a neuron. 74
Figure IV-4: WT-DFIG system controlled with FH-DPC. 78
Figure IV-5: Scheme of FH-DPC. 78
Figure IV-6 : MFs of generated active power error. 78
Figure IV-7 : MFs of compensated local reactive power error. 78
Figure IV-8 : MFs of digital error powers. 79
Figure IV-9 : WT-DFIG system controlled with NH-DPC. 80
Figure IV-10 : Architecture of hysteresis neural network. 81
Figure IV-11 : Performance of trained NH. 81
Figure IV-12 : WT-DFIG system controlled with PNN-DPC. 82
Figure IV-13 : Architecture of prediction neural network. 83
Figure IV-14 : Performance of trained PNN. 84
Figure IV-15 : WT-DFIG system controlled with CNN-DPC. 85
Figure IV-16 : Architecture of classification neural network. 85

Figure IV-17 : Confusion matrix of the overall data based on trained CNN. 86
Figure IV-18 : Wind profile and DFIG speed. 88
Figure IV-19 : Generated active power with its reference, (a) using FH/NH-DPC, (b) using PNN/CNN-DPC. 88
Figure IV-20 : Compensated local reactive power with its reference, (a) using FH/NH-DPC, (b) using PNN/CNN-DPC. 88
Figure IV-21 : Comparison of generated active power using FH/NH and PNN/CNN references across operating modes, (a) Super-synchronous (FH/NH-DPC), (b) Sub-synchronous (PNN/CNN-DPC), (c) Synchronous (FH/NH-DPC), (d) Synchronous (PNN/CNN-DPC), (e) Sub-synchronous (FH/NH-DPC), (f) Super-synchronous (PNN/CNN). 89
Figure IV-22: Compensated local reactive power over operating modes using FH/NH-DPC, (a) In sub-synchronous mode (b) In synchronous mode, QAC is consumed and generated, while in super-synchronous mode, QAC is null. (c) In super-synchronous mode, QAC is generated and consumed, while in synchronous mode, QAC is null. 90
Figure IV-23 : Compensated local reactive power over operating modes using PNN/CNN-DPC, (a) In sub-synchronous mode (b) In synchronous mode, QAC is consumed and generated. (c) In synchronous mode, QAC is consumed and generated, QAC is null. (d) In super-synchronous mode. 90
Figure IV-24 : Waveforms of currents generated by the WT-DFIG, using the proposed techniques: The C-DPC, NH-DPC, and FH-DPC, (a) generated currents (b) from sub- to synchronous mode. (c) . from super- to synchronous mode. 92
Figure IV-25 : Waveforms of currents generated by the WT-DFIG, using the proposed techniques: The C-DPC, PNN-DPC, and CNN-DPC, (a) generated currents (b) from sub- to synchronous mode. (c) from super-to synchronous mode. 93
Figure IV-26 : Generated current of phase (a) and its harmonic spectrum in in Sub-, Super-, and Synchronous Modes for, (a) C-DPC, (b) FH-DPC, (c) NH-DPC, (d) PNN-DPC, (e) CNN-DPC. 94
Figure IV-27 : Wind speed profile and DFIG speed 95
Figure IV-28 : λ, β and Cp 95
Figure IV-29 : Generated active power with its reference, (a) using FH/NH-DPC, (b) using PNN/CNN-DPC. 96
Figure IV-30 : Local reactive power with its reference using, (a) FH/NH-DPC, (b) PNN/CNN-DPC. 97

Figure IV-31 : Waveforms currents generated by the WT-DFIG, using the proposed techniques: The C-DPC, NH-DPC, and FH-DPC, (a) generated currents, (b) overspeed mode, (c) synchronous mode, (d) from super-to sub-synchronous mode. 97
Figure IV-32 : Waveforms currents generated by the WT-DFIG, using the proposed techniques: The C-DPC, PNN-DPC, and CNN-DPC, (a) generated currents, (b) overspeed mode, (c) synchronous mode, (d) from super- to sub-synchronous mode. 98
Figure V-1: Overall scheme of proposed DC-MG. 103
Figure V-2 : Hierarchical control architecture. 104
Figure V-3 : Block diagram of GSC Fuzzy-DPC implementation. 111
Figure V-4 : Overall scheme of PV and its Fuzzy-MPPT. 112
Figure V-5 : Global structure of BESS control. 114
Figure V-6 : Global structure of FC control. 115
Figure V-7 : SOC Thresholds and Hysteresis Transitions in BESS. 116
Figure V-8: Flowchart of EMS. 117
Figure V-9 : Wind and DFIG speed and irradiation. 118
Figure V-10 : DC load power and local reactive power demands. 119
Figure V-11 $Cp, \lambda \; and \; \beta$ responses. 119
Figure V-12 : Generated power by WT-DFIG. 120
Figure V-13 : Local compensated reactive power. 120
Figure V-14 : Power of DFIG's rotor. 121
Figure V-15 : PV power. 121
Figure V-16 : Available power at DC-Microgrid. 121
Figure V-17 : Battery power. 121
Figure V-18 : Fuel cell power. 122
Figure V-19 : Power exchange between the DC-MG and AC grid at GSC. 122
Figure V-20 : Battery and DC bus voltages. 122
Figure V-21 : State of Charge of battery. 122
Figure V-22 : Pg with reference using F-DPC. 123
Figure V-23 : Qg with reference using F-DPC 123
Figure V-24 : AC grid power. 123

TABLE OF TABLES

Table I-1: Comparison of HAWTs and VAWTs 11
Table I-2: Comparison of Major PV Technologies 14
Table III-1 : RSC DPC switching table. 56
Table III-2 : GSC DPC switching table. 61
Table IV-1:Fuzzy Rule of FH-DPC. 79
Table IV-2 : Switching table of FH/NH-DPC for RSC. 79
Table IV-3 : Neural network's training samples. 81
Table IV-4: Neural network's training samples. 83
Table IV-5 : Summary of the CNN-DPC training results. 86
Table IV-6 :Comparison of different control techniques for active power ripple. 91
Table IV-7 :Comparison of different control methods for local reactive power compensation ripple. 91
Table IV-8 : Comparison of different control techniques for the current generated THD. 92
Table IV-9 : Comparative Summary and Trade-offs of Proposed AI-DPC Strategies. 100
Table V-1 : GSC Fuzzy-DPC rule. 111
Table V-2 : Fuzzy-MPPT rule. 113

LIST OF NOMENCLATURE / SYMBOLS

A_t	Rotor swept area (wind turbine), m^2
β	Blade pitch angle (wind turbine), degrees (°)
C_{bat}	Battery equivalent capacitance, F
C_{DC}	DC link capacitance, F
C_{dl}	Double-layer capacitance (PEMFC), F
C_{O_2}	Oxygen concentration (PEMFC), mol/m^3
$C_p, C_{p,max}$	Power coefficient and maximum power coefficient (wind turbine), dimensionless
$d, \Delta D$	Duty cycle of DC/DC converter switches and change in duty cycle (PV MPPT), dimensionless
δ_r, γ	Angle between rotor and stator flux in $\alpha - \beta$ frame, radians
E_0	Battery electromotive force (no-load voltage), V
$E(k), \Delta E(k)$	Error and change in error for PV MPPT, V
E_{Nernst}	Nernst voltage (PEMFC), V
$E_{\text{powers}}, E_1 \dots E_6$	Digital error output and membership functions from FH-DPC/NH-DPC, dimensionless
$eP_g, eQ_g, eP_s, eQ_{AC}$	Active and reactive power errors (GSC and RSC contexts), W and VAR
f_v / f_{vis}	Viscous friction, N·m·s/rad
G	Gearbox gain (dimensionless) or solar irradiance, W/m^2
G_{ref}	Reference irradiance (1000 W/m^2)
$HP_g, HQ_g, HP_s, HQ_{AC}$	Digitized error signals from hysteresis comparators (GSC and RSC), dimensionless
I, I_0, I_{ph}	Cell output current, diode reverse saturation current, light-generated photocurrent (PV), A
$I_{bat}, I_{bat-ref}$	Battery current and current reference, A
i_c	Current through DC link capacitor, A
i_{dc-ref}	DC current reference, A
I_{FC}, I_{FC-ref}	Fuel cell current and setpoint, A
$i_g, i_{g\alpha}, i_{g\beta}$	Grid current vector and components in stationary frame (GSC), A
I_L	Inductor current, A
$i_{rd}, i_{rq}, i_{r\alpha}, i_{r\beta}, i_{ra}, i_{rb}, i_{rc}$	Rotor currents in d-q, stationary, and three-phase frames, A
I_{sc-ref}	Short-circuit current at STC (PV), A
$i_{sd}, i_{sq}, i_{s\alpha}, i_{s\beta}, i_{sa}, i_{sb}, i_{sc}$	Stator currents in d-q, stationary, and three-phase frames, A
J, J_{max}	Current density and maximum current density (PEMFC), A/m^2
J_t, J_g	Turbine and generator inertia, $kg \cdot m^2$
k	Boltzmann constant ($1.3806 \cdot 10^{-23}$ J/K)
K_i	Temperature coefficient of short-circuit current (PV), A/K
$L, L_f, L_m, L_{rr}, L_{ss}, L_{s\sigma}, L_{r\sigma}$	Inductances : general, filter, mutual, rotor and stator self- and leakage inductances, H
λ, λ_{opt}	Tip speed ratio and optimal tip speed ratio (wind turbine), dimensionless
M, M_{sr}, M_{rs}	Mutual inductance matrices (H)
N	Sector number of stator/rotor flux or grid voltage, integer
n_{cells}	Number of cells in PEMFC stack, integer
Ω_t, Ω_{mec}	Turbine and mechanical angular speed, rad/s
ω_s, ω_r	Stator and rotor electrical angular pulsations, rad/s
$P_{AC}, P_g, P_{g-ref}, P_s, P_{s-ref}, P_{load}, P_{net}, P_{PV}, P_{FC}, P_{FC-max}$	Active power terms: AC side, grid, stator, load, net DC, PV, fuel cell, W
$P_{bat-max}^{charge}$, $P_{bat-low}^{discharge}$, $P_{bat-max}^{discharge}$, $P_{bat-ref}$	Battery power limits and references, W

P_{H_2}, P_{O_2}	Partial pressures of hydrogen and oxygen (PEMFC), atm or Pa
$\varphi_r, \varphi_{rd}, \varphi_{rq}, \varphi_{r\alpha}, \varphi_{r\beta}, \varphi_{ra}, \varphi_{rb}, \varphi_{rc}$	Rotor flux linkages in various frames, Wb
$\varphi_s, \varphi_{sd}, \varphi_{sq}, \varphi_{s\alpha}, \varphi_{s\beta}, \varphi_{sa}, \varphi_{sb}, \varphi_{sc}$	Stator flux linkages in various frames, Wb
q	Electron charge ($1.6022 \cdot 10^{-19}$ C)
$Q_{AC}, Q_{AC-ref}, Q_g, Q_{g-ref}$	Reactive power terms (RSC and GSC), VAR
Q_n	Nominal battery capacity, Ah
R	Blade radius (wind turbine), m
$R_{bat}, R_c, R_f, R_m, R_r, R_s, R_{sh}, R_{bit}, R_{FC_{share}}$	Resistances: battery internal, electronic (PEMFC), filter, ionic (PEMFC), rotor, stator, shunt (PV), power sharing ratios (Ω, dimensionless)
ρ	Air density, kg/m^3
$S_j(S_a, S_b, S_c)$	Boolean switching functions for converter legs (dimensionless)
$SOC, SOC_{min}, SOC_{max}, SOC_{high}, SOC_{normal}$	Battery State of Charge and thresholds, %
T, T_{ref}	Cell junction temperature and reference temperature (PV), K
τ	Time constant (PEMFC), s
$T_{em}, T_{mec}, T_t, T_{ref}$	Electromagnetic, mechanical, turbine torque and temperature references, N·m, K
θ, θ_g	Instantaneous electrical rotor angle and grid voltage angle, radians or degrees
v	Wind velocity, m/s
$V_0 \dots V_7, V_{act}, V_{bat}, V_{Cb}, V_{cell}, V_{con}, V_d, V_{dc}, V_{dc-ref}, V_{FC,stack}, V_{g\alpha}, V_{g\beta}, V_{in}, V_{out}, V_{mpp}, V_n, V_{ohm}, V_s, V_t$	Voltages : converter vectors, activation, concentration, ohmic losses, battery, DC link, PEMFC stack, grid voltages, Boost converter voltages, MPP voltage, thermal voltage, V
$v_c, v_{rd}, v_{rq}, v_{r\alpha}, v_{r\beta}, v_{ra}, v_{rb}, v_{rc}, v_{sd}, v_{sq}, v_{s\alpha}, v_{s\beta}, v_{sa}, v_{sb}, v_{sc}$	Voltages in various frames (GSC, rotor, stator, phases), V
$\xi_1, \xi_2, \xi_3, \xi_4$	Empirical PEMFC activation loss coefficients, dimensionless

LIST OF ACRONYMS

AC	Alternating Current
AFC	Alkaline Fuel Cell
AI	Artificial Intelligence
ANN	Artificial Neural Network
a-Si	Amorphous Silicon (PV)
BC	Backstepping Control
BC-DPC	Backstepping Control Direct Power Control
BEM	Blade Element Momentum
BESS	Battery Energy Storage System
CAES	Compressed Air Energy Storage
C-DPC	Conventional Direct Power Control
CdTe	Cadmium Telluride (PV)
CE	Cross-Entropy (ANN training)
CIGS	Copper Indium Gallium Selenide (PV)
CNN-DPC	Classification Neural Network Direct Power Control
c-Si	Crystalline Silicon PV
DC	Direct Current
DC-MG	DC Microgrid
DFIG	Doubly Fed Induction Generator
DPC	Direct Power Control
DPC-SVM	Direct Power Control with Space Vector Modulation
DTC	Direct Torque Control
ECM	Equivalent Circuit Model (battery)
EDLCs	Electrochemical Double-Layer Capacitors
EMS	Energy Management System
ESS	Energy Storage System
FC	Fuel Cell
FES	Flywheel Energy Storage
FH-DPC	Fuzzy-Hysteresis Direct Power Control
FLC	Fuzzy Logic Control

FOC	Field-Oriented Control
Fuzzy-MPPT	Fuzzy Logic-Based Maximum Power Point Tracking
GSC	Grid Side Converter
GWEC	Global Wind Energy Council
HAWT	Horizontal-Axis Wind Turbine
HIL	Hardware-in-the-Loop
IGBT	Insulated Gate Bipolar Transistor
IPCC	Intergovernmental Panel on Climate Change
IRENA	International Renewable Energy Agency
MF	Membership Function (Fuzzy Logic)
MLP	Multi-Layer Perceptron (ANN)
MPC	Model Predictive Control
MPPT	Maximum Power Point Tracking
MSE	Mean Squared Error (ANN training)
NaS	Sodium-Sulfur (battery)
NH-DPC	Neural-Hysteresis Direct Power Control
Ni-Cd	Nickel-Cadmium (battery)
Ni-MH	Nickel-Metal Hydride (battery)
NN	Neural Networks
NOAA	National Oceanic and Atmospheric Administration
P&O	Perturb and Observe (MPPT algorithm)
PEMFC	Proton Exchange Membrane Fuel Cell
PHS	Pumped Hydroelectric Storage
PI	Proportional Integral
PMSG	Permanent Magnet Synchronous Generator
PNN-DPC	Prediction Neural Network Direct Power Control
PSF	Power Signal Feedback
PV	Photovoltaic
RC	Resistor-Capacitor (battery model)
RES	Renewable Energy Sources
RSC	Rotor Side Converter
SCG	Scaled Conjugate Gradient (ANN training)
SCIG	Squirrel Cage Induction Generator
SCs	Supercapacitors
SMC	Sliding Mode Control
SMC-DPC	Sliding Mode Control Direct Power Control
SMES	Superconducting Magnetic Energy Storage
SOC	State of Charge
SOFC	Solid Oxide Fuel Cell
STC	Standard Test Conditions (PV)
SVM	Space Vector Modulation
THD	Total Harmonic Distortion(s)
UCs	Ultracapacitors
VAWT	Vertical-Axis Wind Turbine
VRB	Vanadium Redox (battery)
VSC	Voltage Source Converter
WECS	Wind Energy Conversion System
WT	Wind Turbine

GENERAL INTRODUCTION

CONTEXT AND MOTIVATION

The 21st century faces a critical energy dilemma: escalating global demand driven by development, the enduring dominance of fossil fuels contributing to climate change and geopolitical instability, and persistent energy poverty hindering progress in many regions[1]. This sustained reliance on carbon-intensive sources has led to well-documented environmental consequences, including rising global temperatures and extreme weather events, necessitating an urgent shift towards sustainable and equitable energy systems [2].

In response, the global transition to renewable energy sources (RES), particularly wind and solar photovoltaic (PV) energy, has accelerated Significantly. These technologies have seen exponential growth in installed capacity and significant cost reductions[3]. However, their large-scale integration into power grids presents considerable technical challenges. The inherent intermittency and variability of RES can lead to grid instability, power quality issues such as voltage and frequency fluctuations, and an increased need for grid flexibility, demanding innovative solutions for reliable operation [4, 5].

Within wind energy conversion, Doubly-Fed Induction Generators (DFIGs) are widely adopted for large turbines due to their variable-speed capabilities and efficient power control. Effective control of DFIG rotor-side (RSC) and grid-side (GSC) converters is crucial for maximizing energy capture and ensuring power quality. Classical control strategies, like Conventional Direct Power Control (C-DPC), though simple and fast, suffer from inherent limitations. These include significant power ripples, high Total Harmonic Distortion (THD) in grid-injected currents, and variable switching frequencies, which adversely affect overall system efficiency and power quality [6-8].

These deficiencies in classical control motivate the exploration of advanced models. Artificial Intelligence (AI) techniques, including Fuzzy Logic Control (FLC) and Artificial Neural Networks (ANNs), offer promising avenues to address the non-linearities and uncertainties in renewable energy systems. AI-based controllers can provide adaptive and intelligent decision-making, potentially improving performance in ripple reduction and harmonic mitigation [9, 10]. Concurrently, DC microgrids are emerging as efficient and flexible platforms for integrating diverse RES and energy storage systems (ESS). Their advantages, such as reduced conversion losses and simplified energy management, make them ideal for modern distributed generation [11, 12]. This

research is therefore driven by the need to develop and rigorously evaluate advanced AI-based control algorithms for WT-DFIG systems and to investigate their synergistic integration within a comprehensive DC microgrid. The ultimate aim is to enhance power quality, system efficiency, and overall operational performance, contributing to a more sustainable energy future.

RESEARCH OBJECTIVES AND CONTRIBUTIONS

The main objective of this thesis is to contribute to the development and evaluation of advanced control algorithms, with a strong emphasis on Artificial Intelligence techniques, for renewable energy systems. The research focuses on enhancing the performance and power quality of Doubly-Fed Induction Generator (DFIG)-based wind turbines and their effective integration into a comprehensive DC microgrid with photovoltaic (PV) systems, battery energy storage systems (BESS), and auxiliary power generation system fuel cell (FC).

The specific objectives pursued to achieve this main goal are:

- ✓ To develop detailed mathematical models for all key components of the DC microgrid, including the WT-DFIG, PV array, BESS, FC system, and their associated power electronic converters, providing a robust foundation for simulation and control design.
- ✓ To conduct a critical analysis of classical control strategies, particularly Conventional Direct Power Control (C-DPC), for both the Rotor Side Converter (RSC) and Grid Side Converter (GSC) of the DFIG, identifying their performance limitations concerning power ripple and harmonic distortion.
- ✓ To design, implement, and comparatively evaluate novel AI-based Direct Power Control strategies for the DFIG's RSC. This includes the exploration of Fuzzy Hysteresis DPC (FH-DPC), Neural Hysteresis DPC (NH-DPC), Prediction Neural Network DPC (PNN-DPC), and Classification Neural Network DPC (CNN-DPC), with the aim of significantly reducing power ripples and Total Harmonic Distortion (THD).
- ✓ To develop and implement intelligent control strategies for other components of the DC microgrid, specifically a Fuzzy Logic-based DPC for the DFIG's GSC and a Fuzzy Logic-based Maximum Power Point Tracking (MPPT) for the PV system, alongside appropriate controllers for the BESS and FC system.
- ✓ To perform a systematic sizing of all DC-microgrid components to ensure operational viability and the capacity to meet defined energy demands.

- ✓ To design and validate a comprehensive rule-based Energy Management System (EMS) to orchestrate power flow between all sources, storage element, the load, and the AC grid, while optimizing renewable energy utilization, ensuring BESS health, and maintaining overall system stability.
- ✓ To evaluate the performance of the fully integrated DC microgrid system under realistic, dynamic environmental conditions and variable load profiles through comprehensive simulations.

The primary contributions of this research are:

- ✓ **Novel AI-Enhanced DPC Strategies for DFIG-RSC:** The development and successful validation of four distinct AI-based DPC strategies (FH-DPC, NH-DPC, PNN-DPC, and CNN-DPC) for the DFIG's RSC, demonstrating substantial improvements in power quality (reduced active and reactive power ripples, lower stator current THD) compared to classical C-DPC. The CNN-DPC strategy, in particular, is identified as a superior approach due to its performance and efficient design.
- ✓ **Intelligent Control for GSC and PV Systems:** The design and application of a Fuzzy Logic-based DPC for the DFIG's GSC and a Fuzzy Logic-based MPPT for the PV system, contributing to enhanced efficiency and performance of these key microgrid components.
- ✓ **Comprehensive DC Microgrid Design and Management**: The holistic design, systematic sizing, and intelligent control of an integrated DC microgrid comprising WT-DFIG, PV, BESS, and FC systems. This includes the development of a robust rule-based EMS that effectively coordinates all distributed energy resources and storage, ensuring reliable and efficient operation.
- ✓ **Demonstrated System-Level Performance Enhancement:** Through extensive simulations, this thesis demonstrates the synergistic benefits of applying advanced AI-based local controllers in conjunction with an effective EMS, leading to improved power quality and robust stability of the overall DC microgrid system under dynamic conditions.

THESIS ORGANIZATION

This thesis is structured into five chapters, systematically addressing the research objectives:

Chapter I: Introduction to Renewable Energy Systems and Advanced Control Strategies provides a comprehensive overview of the global energy context, the imperative for renewable energy, and a detailed discussion of various renewable energy sources, including wind and solar technologies. It highlights the operational principles and control challenges associated

with DFIG-based wind energy systems and introduces the motivation for employing AI-based control strategies. Furthermore, it discusses microgrid architectures, emphasizing the advantages of DC microgrids for integrating renewable sources, and outlines the proposed DC microgrid configuration studied in this thesis.

Chapter II: Modeling of Microgrid Components focuses on the detailed mathematical modeling of each constituent of the DC microgrid. This includes the aerodynamic and electrical subsystems of the WT-DFIG (in various reference frames), the photovoltaic (PV) system including cell and array characteristics, the battery energy storage system (BESS) with its equivalent circuit and State of Charge (SOC) considerations, the Proton Exchange Membrane Fuel Cell (PEMFC) system, and the associated AC/DC/AC and DC/DC power electronic converters.

Chapter III: Classical Control Strategies for DFIG-Based Wind Turbine Systems presents and evaluates a classical control methodology for the WT-DFIG. This includes Power Signal Feedback (PSF) MPPT and Proportional-Integral (PI) Pitch Control for wind power optimization and limitation. It then details the Conventional Direct Power Control (C-DPC) methodology for both the Rotor Side Converter (RSC) and Grid Side Converter (GSC). The chapter concludes with a simulation-based performance analysis of this classical scheme, critically identifying its operational drawbacks, particularly concerning power quality.

Chapter IV: AI-Enhanced Direct Power Control of WT-DFIG Rotor Side Converter addresses the limitations of classical C-DPC by proposing and investigating four novel AI-based DPC strategies for the DFIG's RSC. Two strategies, Fuzzy Hysteresis DPC (FH-DPC) and Neural Hysteresis DPC (NH-DPC), focus on replacing the conventional hysteresis comparators. The other two, Prediction Neural Network DPC (PNN-DPC) and Classification Neural Network DPC (CNN-DPC), employ ANNs for direct voltage vector selection. A comprehensive comparative analysis based on simulation results under various operating conditions is conducted, leading to the selection of CNN-DPC as the preferred strategy due to its superior performance in ripple and THD reduction and efficient design.

Chapter V: Management and Control of the proposed DC-Microgrid synthesizes the preceding work by focusing on the control and management of the entire integrated DC microgrid. It details the implementation of the selected CNN-DPC for the DFIG-RSC and proposes a Fuzzy Logic-based DPC for the DFIG-GSC, along with a Fuzzy-MPPT for the PV system and controllers for the BESS and FC. The chapter describes the systematic sizing of all microgrid components and presents the design and operational logic of a rule-based Energy Management System (EMS). Finally, it presents extensive simulation results to validate the performance of the fully integrated

DC microgrid under dynamic environmental conditions and variable load profiles, demonstrating its stability, efficiency, and power quality.

The thesis concludes with a General Conclusion and Perspectives, summarizing the key findings, reiterating the research contributions, discussing the limitations of the current work, and proposing avenues for future research.

I

INTRODUCTION TO RENEWABLE ENERGY SYSTEMS AND ADVANCED CONTROL STRATEGIES

I.1. INTRODUCTION

The chapter introduces renewable energy systems and advanced control strategies. It discusses the global energy landscape, the environmental challenges and resource constraints driving the need for sustainable energy sources, and key renewable energy technologies. Topics include wind and solar power generation, DFIG wind energy systems, energy storage systems, batteries, fuel cells, microgrid configurations, and DC microgrids. The chapter also highlights control challenges and the rationale for investigating advanced control strategies, particularly those leveraging artificial intelligence and enhanced control algorithms. This chapter's discussion provides a background for understanding the modeling approaches, control strategies, and energy management techniques presented in the thesis.

I.2. GLOBAL ENERGY CHALLENGES AND THE RENEWABLE IMPERATIVE

I.2.1. Historical Perspective

Since the Industrial Revolution, the global energy landscape has transformed significantly. The reliance on fossil fuels has driven unprecedented economic growth and technology advances but also significant environmental consequences. The 20th century saw a huge jump in energy use. Global energy supply grew from about 30 EJ in 1900 to over 600 EJ in 2023 based on the latest statistics reported in Energy Institute [13-15], as presented in Figure I-1. Most of this came from conventional sources, accounting for 81-82% of the global energy mix in 2023 [13].

This historical focus on fossil fuels has created challenges. Economically, markets have been volatile, as seen during oil crises in the 1970s and Europe's recent natural gas issues [16]. Environmentally, fossil fuels have led to substantial greenhouse gas emissions, with CO_2 levels rising from pre-industrial 280 ppm to over 420 ppm by 2024 [17]. This is linked to rising global temperatures, sea level rise, and extreme weather events [18].

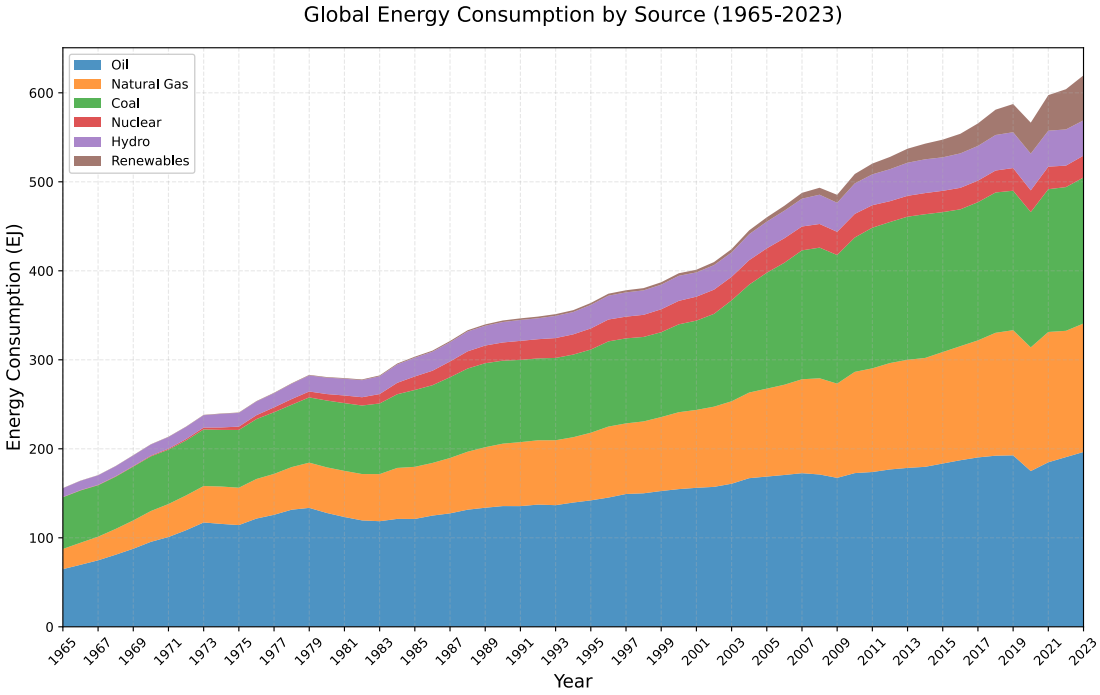

Figure I-1:Global Energy Consumption by Source (1965-2023) [13].

Access to electricity remains limited, with ~733 million people still without it, primarily in parts of Africa and Asia [19]. These challenges demand a global review, emphasizing sustainable alternatives to fossil fuels.

I.2.2. The Renewable Energy Transition

The global shift to renewable energy is transforming how society produces and consumes energy, with significant progress in technologies such as wind, solar, hydroelectric, geothermal, and bioenergy. Over the past decade, global renewable capacity grew from 1,228 GW in 2010 to over 4,448 GW in 2024 [20], as shown in Figure I-2. This expansion added 585 GW of capacity. renewables accounted for 92.5% of all new power generation globally in 2024. Technological innovations have driven significant cost reductions in the levelized cost of electricity. For instance, solar costs have fallen 90% and wind 65% since 2010, making these sources competitive in many

regions [21]. Policy measures like renewable portfolio standards, carbon pricing, and subsidies have accelerated investment and deployment worldwide [22].

Renewable energy sources like wind and solar pose challenges to existing power systems because they are inconsistent and variable. This makes grid stability, frequency regulation, and power quality management difficult. As a result, there is a need for technologies like energy storage, demand response, and improved forecasting [23]. Hybrid renewable energy systems that combine multiple sources with complementary storage solutions like batteries and hydrogen systems offer a strategy to enhance reliability and optimize resource utilization. These systems are effective for microgrid applications, which can operate in both grid-connected and islanded modes [24].

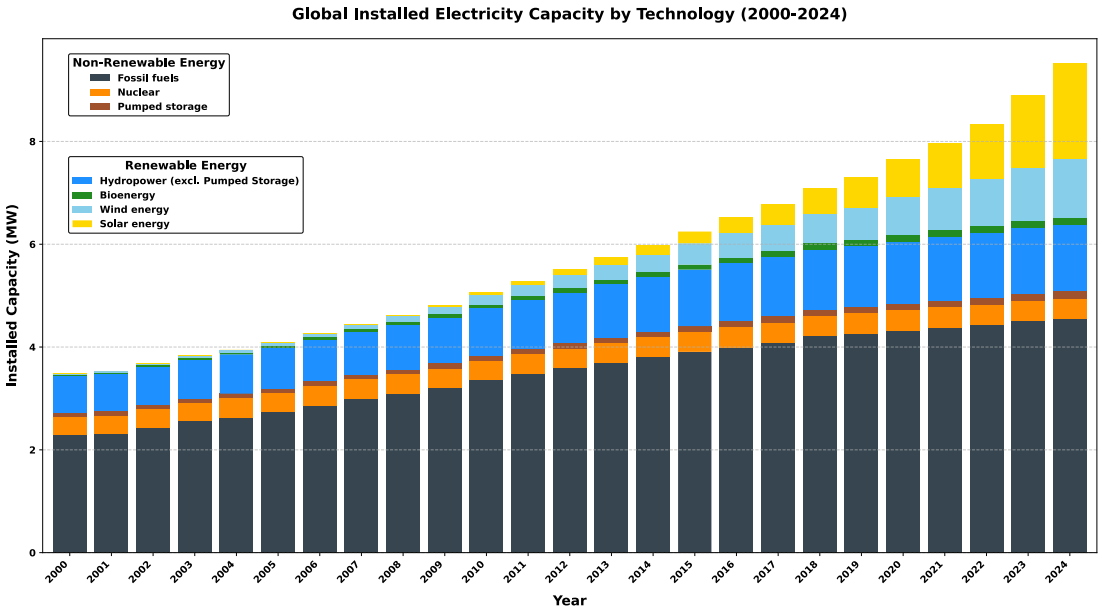

Figure I-2:Global Installed Electricity Capacity by Technology (2000-2024)[20].

I.2.3. Motivation for AI-Based Control Strategies

The transition to renewable energy is crucial, but controlling these systems poses unique challenges. Variability and intermittency of sources like wind and solar can lead to grid instability and quality issues [25]. Advanced renewable energy technologies require sophisticated control algorithms to maximize energy capture and ensure stable integration with the power grid. Managing and optimizing energy flow in complex hybrid renewable energy systems adds a layer of complexity. Traditional control techniques struggle to effectively handle these systems and modern power grid demands [26-28].

This motivates the exploration and application of advanced control strategies, particularly AI-based ones. AI offers the potential to adapt to changing conditions, handle non-linearities and

uncertainties, improve overall performance, enhance power quality and stability, and optimize energy management in complex hybrid systems [29, 30].

I.3. OVERVIEW OF RENEWABLE ENERGY SOURCES

I.3.1. Wind Energy

Wind energy has emerged as a mature and extensively implemented renewable resource, capitalizing on the natural availability of wind [31]. In 2024, global wind power capacity is estimated to have reached approximately 1133 GW, reflecting an annual growth rate of around 11% as reported by [20]. This substantial capacity underscores the sector's rapid development and highlights ongoing improvements in turbine design and control systems that significantly optimize the conversion of aerodynamic energy into electrical power.

I.3.1.1. Wind Energy Conversion Principles

Wind energy conversion involves transforming the kinetic energy of moving air into electrical energy. Wind turbines capture the wind's kinetic energy with blades attached to a rotor, which is connected to a generator that converts the mechanical energy of the rotating blades into electrical energy [32]. Figure I-3 illustrates the components involved in this process.

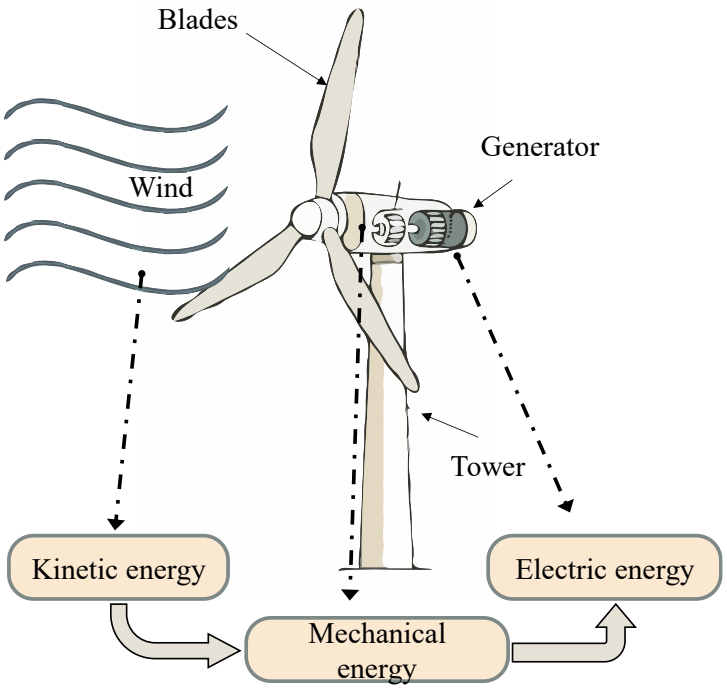

Figure I-3: Process of Horizontal-Axis Wind Turbine Operation.

The efficiency of wind energy conversion depends on the aerodynamic design of the turbine blades, which are designed to maximize energy extraction from the wind. Wind speed, air density, and turbine rotor size are factors considered in the blade design. The power captured by the turbine is proportional to the cube of the wind speed, so wind speed is a critical factor in determining energy production [33, 34].

I.3.1.2. Types of Wind Turbines

Wind turbines are generally classified into two main categories: Horizontal-Axis Wind Turbines (HAWTs) and Vertical-Axis Wind Turbines (VAWTs), as displayed in Figure I-4. Each type exhibits unique characteristics, advantages, and operational challenges that influence their deployment in different scenarios [33, 35, 36].

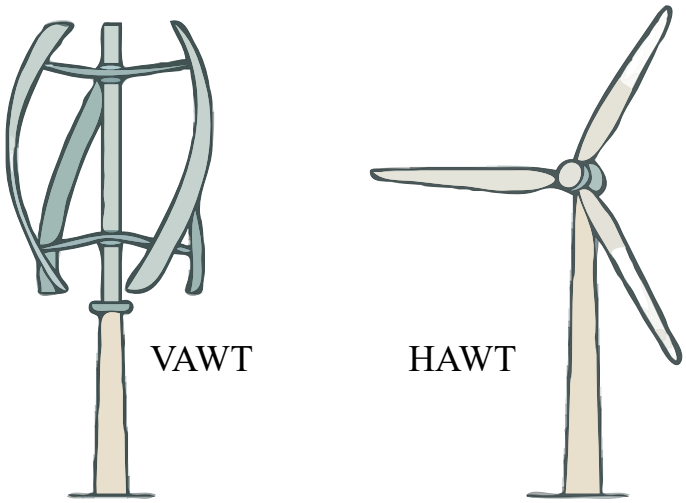

Figure I-4: Types of Wind Turbines.

- **Horizontal-Axis Wind Turbines (HAWTs):**

HAWTs are the most common and efficient technology in wind energy generation. Their horizontal rotor and blades that rotate in a vertical plane make HAWTs more efficient and they have a well-established design. HAWTs are widely adopted in onshore and offshore wind farms because they are energy-saving, can be made bigger, and are easy to maintain. While HAWTs have many benefits, they have a significant visual impact and require complex control systems and strong engineering to manage fatigue and dynamic loads under different wind conditions.

- **Vertical-Axis Wind Turbines (VAWTs):**

Vertical-axis wind turbines (VAWTs) are a different kind of wind turbine. Their rotors are oriented vertically, so they can collect energy from every direction. This makes them well-suited for

urban environments and areas with turbulent wind because there's no need for yaw control. However, VAWTs have trade-offs. They can't capture energy from all directions like HAWTs, and this affects their energy efficiency.

Table I-1: Comparison of HAWTs and VAWTs

Technology	Advantages	Disadvantages
HAWTs	High energy capture efficiency, scalability, ease of maintenance	Visually intrusive, requires significant infrastructure
VAWTs	Omnidirectional, suitable for urban environments	Lower efficiency, higher mechanical stresses

I.3.1.3. Generator Technologies

The conversion of mechanical energy from wind turbines into electrical energy is accomplished by generator systems that must operate efficiently across a range of wind conditions. The selection of generator technology significantly impacts the overall performance, reliability, and cost-effectiveness of wind energy conversion systems [37-39]. As shown in Figure I-5, the main generator technologies are listed below:

- **Doubly Fed Induction Generators (DFIGs):**

Doubly Fed Induction Generators (DFIGs) are essential in modern wind energy conversion systems, favored for their efficient operation at various wind speeds. This variable-speed capability is due to a unique design, including a wound rotor induction generator coupled with a converter. The converter system, with a rotor-side converter (RSC) and a grid-side converter (GSC), enables slip power transfer, optimizing RSC capture while controlling reactive power and ensuring grid stability and power quality via GSC. Their flexibility and high efficiency make DFIGs ideal for onshore and offshore wind power projects.

- **Permanent Magnet Synchronous Generators (PMSGs):**

Permanent magnet synchronous generators (PMSGs) are a significant technology in wind energy conversion systems. These generators use permanent magnets within the rotor and eliminate the need for excitation, slip rings, and brushes, improving efficiency and reducing maintenance. The absence of these components also improves reliability and enhances dynamic performance. PMSGs are particularly advantageous for offshore wind turbines due to their gearless design, which simplifies mechanical complexity and increases durability. The cost and management of permanent magnet materials may limit their large-scale use.

➢ **Squirrel Cage Induction Generators (SCIGs):**

Squirrel cage induction generators (SCIGs) are known for their robust, simple design and historical significance to fixed-speed wind turbines, ensuring reliability with their rotor. SCIGs operate via electromagnetic induction, with the rotor generating power slightly faster than synchronous speed. They're rugged enough for cost- and reliability-focused applications but require reactive power, which can be a limitation in modern wind farms focused on grid stability. SCIGs are less efficient than DFIGs and PMSGs for maximizing energy capture across wind speeds.

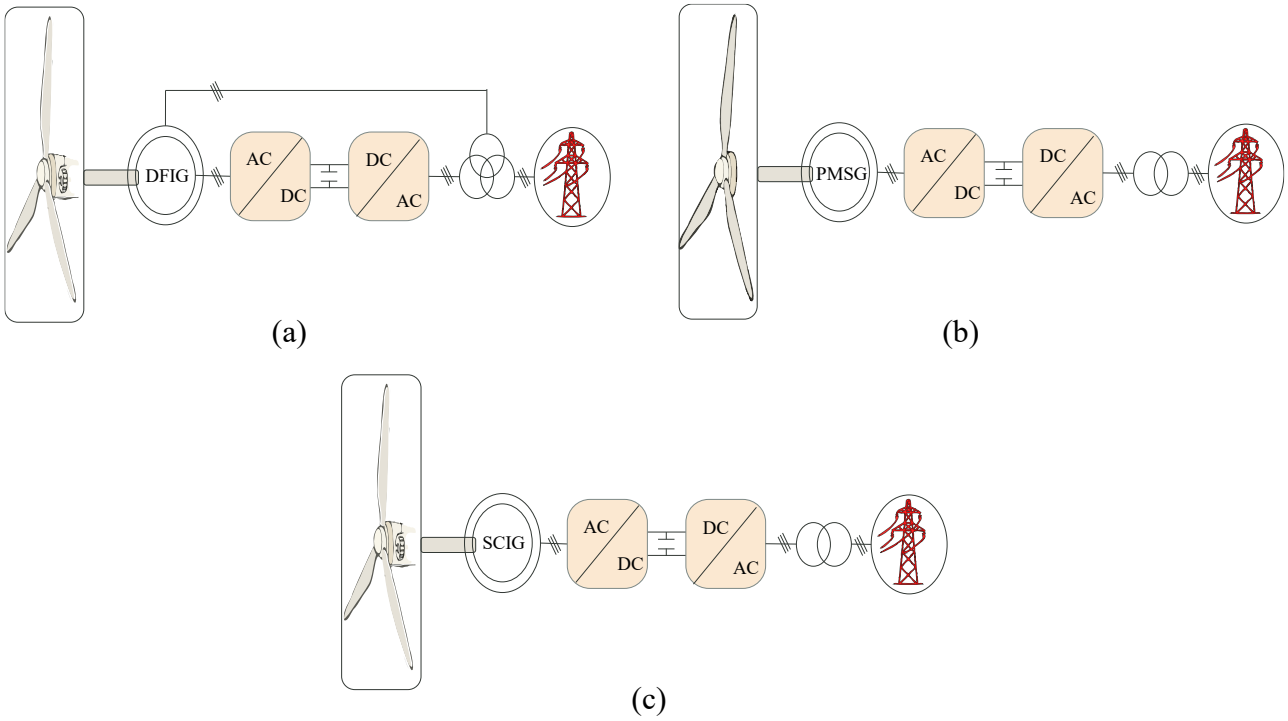

Figure I-5: AC grid-connected wind turbine generator configurations— (a) Doubly-Fed Induction Generator (DFIG), (b) Permanent Magnet Synchronous Generator (PMSG), (c) Squirrel Cage Induction Generator (SCIG).

I.3.2. Solar Energy

Solar energy stands as another mature and widely adopted renewable resource, harnessing the abundant energy from sunlight [20]. In 2024, the global installed solar power capacity is estimated to have surpassed 1800 GW, indicating an approximate annual growth rate of 32.2%, according to IRENA 2024. This impressive expansion demonstrates the sector's dynamic progress and emphasizes continuous innovations in photovoltaic technology and energy storage solutions that are enhancing the efficiency and reliability of solar power generation.

I.3.2.1. Principles of Photovoltaic

Solar energy conversion uses sunlight to make electricity. Photovoltaic (PV) systems do this using the photovoltaic effect. This happens when photons from sunlight hit a semiconductor material like silicon. This exciting of electrons through a circuit generates electricity. The process's efficiency depends on the sunlight's intensity and the PV cells' characteristics [40-42]. The process involves the following steps, as illustrated in Figure I-6:

- Photon Absorption: Photons from sunlight are absorbed by the semiconductor material in the PV cells.
- Excitation of Electrons: The absorbed photons transfer their energy to electrons, which become excited and flow through the material.
- Electrical Current Generation: The excited electrons are collected and form an electrical current, which is then sent through an inverter to convert it from DC to AC power for grid integration or direct use.

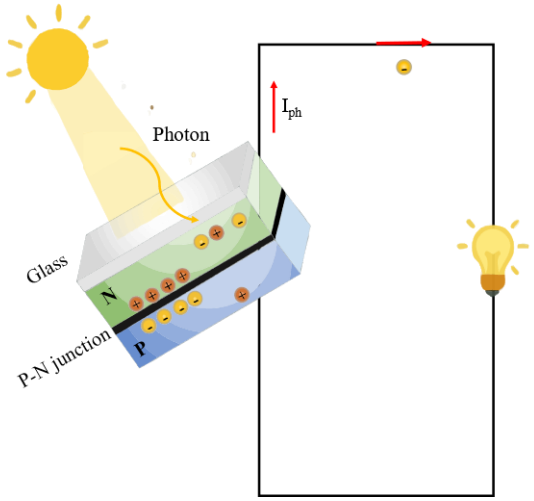

Figure I-6: Working principle of the PV cell.

I.3.2.2. Photovoltaic Technologies

Solar photovoltaic technologies are generally classified into several main categories, each with distinct characteristics, performance parameters, and applications [43-45].

➢ **Crystalline Silicon PV (c-Si):**

Dominant market technology using silicon wafers. Monocrystalline offers higher efficiency (20-22%) while polycrystalline provides cost advantages at lower efficiency (17-19%). Benefits from established manufacturing but faces energy-intensive production challenges.

- **Thin-Film Technologies:**

Microscale semiconductor layers (CdTe, CIGS, a-Si) on various substrates. Advantages include flexible manufacturing, reduced material usage, and better performance in diffuse light/high temperatures. Lower efficiencies (10-18%) but are suitable for lightweight and flexible applications.

- **Emerging PV Technologies:**

Next-generation technologies include perovskites, organic photovoltaics, and quantum dot cells. Perovskites have reached >25% efficiency in laboratories. Offer potential for transparency, flexibility, and simpler manufacturing but face stability and durability challenges.

Table I-2: Comparison of Major PV Technologies

Technology	Advantages	Disadvantages
Crystalline Silicon	High efficiency, proven durability, established supply chain	Energy-intensive production, rigid form factor
Thin-Film	Material efficiency, performance in diffuse light, flexible substrates	Lower efficiency, potential material constraints
Emerging Technologies	Cost potential, novel properties, integration possibilities	Stability issues, limited commercial readiness

I.3.2.3. Solar PV System Configurations

The implementation of solar energy systems offers different configurations to capture energy, ensure system reliability, and integrate with the grid, as presented in Figure I-7. The selection of system architecture impacts performance, cost-effectiveness, and application suitability [46, 47]. The primary system configurations include:

- **Grid-Connected PV Systems:**

Dominant deployment model that integrates with existing electrical infrastructure. These systems convert solar energy to AC via inverters and exchange power with the utility grid, enabling net metering during excess generation while drawing from the grid when needed. Modern systems provide grid-support functions like reactive power control and voltage regulation. Lower cost due to avoided storage requirements, but dependent on grid reliability.

- **Stand-Alone PV Systems:**

Independent systems for remote locations where grid connection is impractical. Require energy storage (typically batteries) and careful sizing of generation capacity. Components include

charge controllers, inverters, and sometimes backup generators. Offer energy independence but involve higher initial investment and maintenance costs.

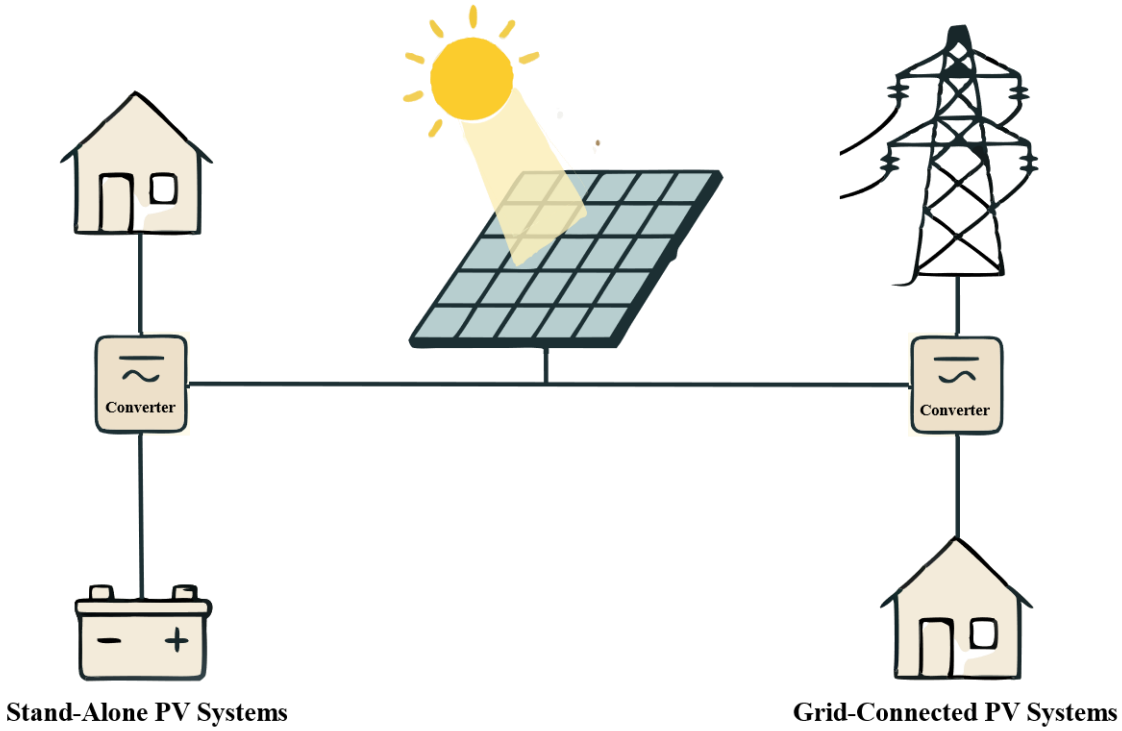

Figure I-7: Solar PV System Configurations.

I.3.3. Integration of Renewable Energy Systems into Microgrids

Integrating renewable energy sources like wind and solar into microgrids is essential for enhancing energy resilience, reducing fossil fuel dependence, and improving energy security [48]. Microgrids, which can operate independently or with the main grid, help mitigate the intermittency of renewable energy by combining multiple sources and incorporating energy storage systems such as batteries for direct energy storage and fuel cells for converting stored fuel to electricity. These storage systems balance supply and demand by storing excess energy when generation is high and discharging it during low generation periods.

I.4. FUEL CELLS

Fuel cells are energy conversion devices that generate electricity through electrochemical reactions between hydrogen and oxygen. They continuously produce electricity as long as fuel is supplied. Fuel cells are known for their high efficiency, low emissions, and suitability for a wide range of applications, including transportation, backup power, and stationary power generation [49, 50].

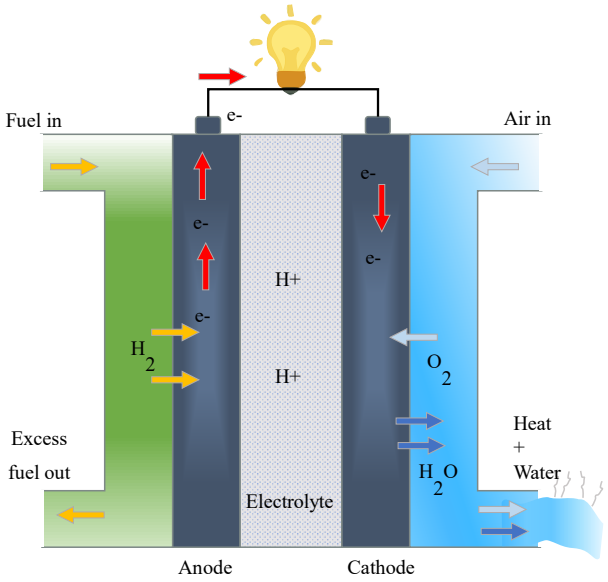

Figure I-8 : Fuel cell working principle.

I.4.1. Working Principle

The general working principle of a fuel cell involves, as explained in Figure I-8:

- Hydrogen input: Hydrogen molecules enter the anode side of the fuel cell.
- Electron separation: The hydrogen atoms are split into protons and electrons. The protons pass through a specialized membrane to reach the cathode.
- Electron flow: The electrons travel through an external circuit, creating an electric current.
- Reaction at cathode: At the cathode, the electrons and protons combine with oxygen, producing water and heat as byproducts.

I.4.2. Types of Fuel Cells

There are several types of fuel cells, each with distinct characteristics suitable for different applications [51]:

- **Alkaline Fuel Cells (AFCs):** Early, cost-effective, and efficient, requiring high-purity hydrogen. Less suitable for high-current density applications.
- **Proton Exchange Membrane Fuel Cells (PEMFCs):** Use a solid polymer electrolyte, making them suitable for high-power applications. Offer quick startup times, high efficiency, and longevity but are expensive and have a shorter lifespan.

- **Solid Oxide Fuel Cells (SOFCs):** Use a solid ceramic electrolyte, operating at high temperatures (above 600°C). Provide high efficiency and fuel flexibility, but require longer startup times and durable materials because of the high operational temperatures.

I.5. ENERGY STORAGE SYSTEMS

Energy Storage Systems (ESS) are pivotal for enhancing the reliability, stability, and economic viability of power systems, particularly those with high penetration of intermittent Renewable Energy Sources (RES) such as wind and solar. ESS technologies address the mismatch between RES generation profiles and load demand, facilitate grid ancillary services, and improve power quality [52]. This section primarily details Electrochemical Storage via Battery Energy Storage Systems (BESS), which are central to the microgrid configuration studied in this thesis, and subsequently provides a concise overview of other notable ESS technologies to offer a broader perspective on the field.

I.5.1. Electrochemical Storage (Batteries)

Battery energy storage systems are a top solution for storing renewable energy. These systems convert chemical energy into electrical energy through redox reactions. They consist of two electrodes (cathode and anode) separated by an electrolyte [53].

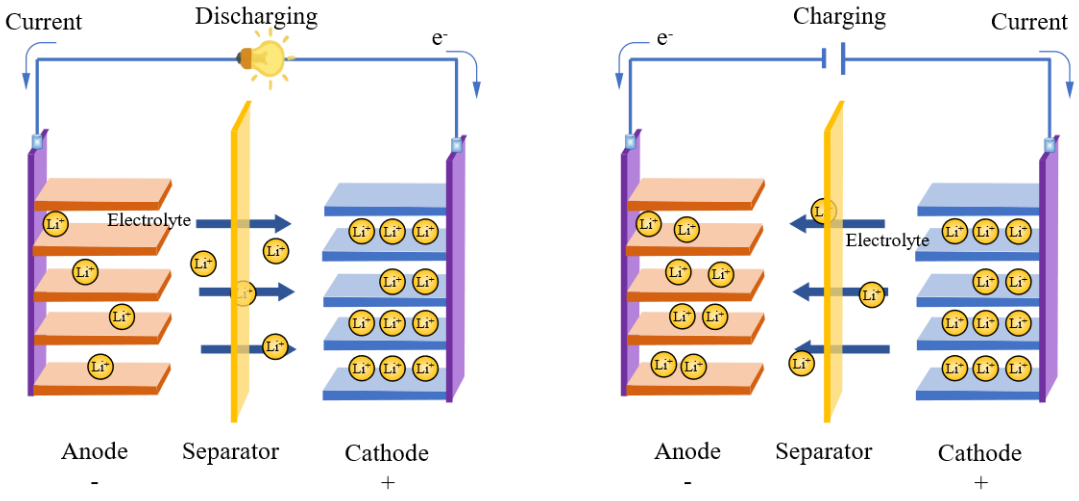

Figure I-9 : Basic working principle of a battery.

I.5.1.1. Working Principle

When a battery is connected to an external circuit, chemical reactions at the electrode-electrolyte interfaces drive the flow of electrons, generating an electric current. Simultaneously, ions

move through the electrolyte to maintain charge neutrality During charging, this process is reversed by an external power source, forcing electrons back into the anode and restoring the battery's chemical potential, as illustrated in Figure I-9 [54].

I.5.1.2. Types of Batteries

Several battery technologies have been developed to optimize energy storage based on efficiency, longevity, and cost [55]. The most common types include:

- **Lead-Acid Batteries:**

  One of the oldest and most established battery technologies, lead-acid batteries are widely used due to their low cost and reliability. However, they have relatively low energy density and shorter lifespan compared to newer technologies.

- **Lithium-Ion Batteries:**

  These batteries offer higher energy density, longer cycle life, and better efficiency, making them the preferred choice for electric vehicles, portable electronics, and grid storage. Despite their advantages, they have higher costs and potential safety concerns related to thermal runaway.

- **Other advanced battery technologies:**

  Such as Nickel-Metal Hydride (Ni-MH), Nickel-Cadmium (Ni-Cd), Vanadium Redox (VRB), Sodium-Sulfur (NaS), and Zinc Bromide batteries, offer alternative solutions depending on specific application requirements.

I.5.2. Overview of Other Energy Storage System Technologies

While BESS represents a versatile and increasingly prevalent ESS solution, various other technologies offer distinct advantages for specific applications. Understanding this broader landscape is crucial for comprehensive energy system design. These systems can be broadly categorized based on their energy storage medium:

I.5.2.1. Mechanical Storage Systems

Mechanical storage technologies convert electrical energy into potential or kinetic energy for later reconversion to electricity.

- **Pumped Hydroelectric Storage (PHS):** PHS is a mature and widely deployed large-scale ESS. It involves pumping water from a lower to an upper reservoir during periods of low demand or surplus energy, then releasing it through turbines to generate electricity when needed [56].

- **Main Characteristics:** Very large capacity, long operational life, high efficiency (typically 70-85%), and low self-discharge.
- **Limitations:** Significant geographical constraints (requiring suitable topography and water availability), substantial capital investment, and long development times, making it suitable primarily for grid-scale applications.

- **Compressed Air Energy Storage (CAES):** In CAES systems, ambient air is compressed and stored under pressure, often in underground geological formations (e.g., salt caverns) or man-made vessels. When electricity is required, the compressed air is heated and expanded through a turbine.
  - **Main Characteristics:** Large storage capacity, long lifespan, and low self-discharge rates.
  - **Limitations:** Similar to PHS, CAES often has geographical dependencies for suitable storage sites, requires large-scale investment, and is typically deployed for utility-scale energy management. Efficiency can be impacted by heat management during compression and expansion.
- **Flywheel Energy Storage (FES):** FES systems store energy kinetically in a rapidly spinning rotor (flywheel) maintained in a low-friction environment (often a vacuum).
  - **Main Characteristics:** High power density, very fast response times (milliseconds), excellent cycle life (hundreds of thousands to millions of cycles), high round-trip efficiency (often >90%), and relatively low maintenance.
  - **Limitations:** Higher self-discharge rates compared to PHS, and typically lower energy density than batteries, making them less suitable for long-duration energy storage [57].

I.5.2.2. Electrical Storage Systems

These systems store energy directly in electric or magnetic fields.

- **Supercapacitors (SCs) / Ultracapacitors (UCs):** Also known as Electrochemical Double-Layer Capacitors (EDLCs), SCs store energy electrostatically by accumulating charge at the interface between high-surface-area electrodes and an electrolyte. They offer characteristics between conventional capacitors and batteries [58].
  - **Main Characteristics:** Extremely high-power density, exceptionally fast charge/discharge rates, very long cycle life (often >1 million cycles), wide operating temperature range, and high reliability.

- **Limitations:** Lower energy density compared to batteries, meaning they store less energy for a given size/weight. They also tend to have higher self-discharge rates than batteries.

➢ **Superconducting Magnetic Energy Storage (SMES):** SMES technology stores energy within the magnetic field generated by a DC current flowing through a cryogenically cooled superconducting coil [59].

- **Main Characteristics:** Near-instantaneous response (milliseconds), very high round-trip efficiency (typically >95%), and an almost unlimited number of charge/discharge cycles. Once charged, there are virtually no losses in the stored energy itself.
- **Limitations:** High capital costs associated with superconducting materials and the necessary cryogenic cooling systems. The technology is complex and primarily deployed in specialized, high-value applications. Energy density is also a consideration.

I.6. DFIG-BASED WIND ENERGY SYSTEMS AND CONTROL CHALLENGES

I.6.1. System Components and Advantages

Modern wind energy conversion systems use the Doubly-Fed Induction Generator (DFIG) technology, which is most common at medium and large scales. These systems have several key components that efficiently convert wind energy at any speed [60].

A DFIG system has a wind turbine, gearbox, doubly fed induction generator (DFIG), power electronic converters, and control systems. The turbine uses aerodynamically designed blades to convert wind energy into mechanical rotation. A gearbox increases the turbine's low rotational speed to match the generator's high speed [61].

The DFIG is a wound rotor induction machine where the stator and rotor windings convert energy.

A back-to-back converter configuration links the rotor circuit to the grid in DFIG systems. It consists of a rotor-side converter (RSC) and a grid-side converter (GSC), connected via a DC-link capacitor [62].

DFIG-based WECS systems offer several significant advantages that have contributed to their widespread adoption in the wind energy sector:

The essential advantages of this configuration include:

- **Wound Rotor Induction Generator (DFIG):** Unlike squirrel-cage generators, DFIG uses a wound rotor with slip rings, enabling rotor windings to be accessed. Power can thus be added to or removed from the rotor circuit via the converter, a feature essential for certain uses.
- **Partially Rated Power Electronic Converter (RSC):** This converter, a back-to-back design with a RSC and a GSC, is placed between the rotor windings and the grid. Its partial rating reduces cost and power losses compared to fully rated converters in other variable-speed turbine technologies.
- **Wide variable Speed Operation:** The converter allows variable speed operation over wide range. The turbine can adjust its speed to track the optimal tip-speed ratio for different wind speeds, capturing more energy.
- **Active and Reactive Power Control:** Power electronic converters independently control both active and reactive power sent to the grid. This is vital for grid stability, voltage regulation, and power factor correction.
- **Enhanced System Efficiency:** DFIG systems can achieve greater energy capture and overall system efficiency compared to fixed-speed turbines by optimizing rotor speed and regulating power flow.

I.6.2. Limitations of Classical Control Strategies

Classical control strategies have been widely employed for DFIG systems, including Vector Control (VC), Direct Torque Control (DTC), and Direct Power Control (DPC). While these methods have proven effective to a certain extent, they also exhibit limitations:

- FOC have been the industrial standard for DFIG systems due to their simplicity and effective power control through decoupling electromagnetic torque and flux. However, they suffer from performance degradation under nonlinearities and parameter variations [62].
- DTC and DPC offer alternatives by eliminating inner current control loops. DTC controls torque and flux directly using a switching table, while DPC directly manages power via voltage vectors. Both methods provide faster dynamics and reduced dependency on parameters. However, conventional DPC and DTC implementations can result in variable switching frequencies and higher Total Harmonic Distortion (THD) [63, 64].

To overcome these limitations, advanced control techniques have been proposed, leveraging artificial intelligence (AI) for adaptive and intelligent decision-making.

I.6.3. AI-Based Control Strategies for DFIG Systems

Artificial intelligence (AI)-based control strategies have gained significant attention in recent years due to their ability to handle the non-linearities and uncertainties in DFIG-based wind energy systems. These strategies include artificial neural networks (ANN), fuzzy logic controllers.

In DFIG based on WESC systems, both Artificial Neural Networks and Fuzzy Logic controllers offer the many advantages. Each technique quickly adapts to parameter changes, providing smoother operation and greater stability during wind speed fluctuations. Their ability to effectively manage nonlinearities enhances efficient energy conversion while minimizing power fluctuations and Total Harmonic Distortion (THD) [65-67].

I.7. MICROGRIDS

Microgrids represent an innovative approach to distributed energy management by integrating multiple renewable energy sources, storage systems, and loads into a coordinated and self-sustained electrical network. These localized grids enhance resilience, efficiency, and reliability by providing energy autonomy while reducing dependency on centralized power infrastructures. With increasing penetration of renewable energy sources, microgrids serve as an essential component in modern energy systems [68, 69]. The Figure I-10 illustrates the key components and configurations of a microgrid.

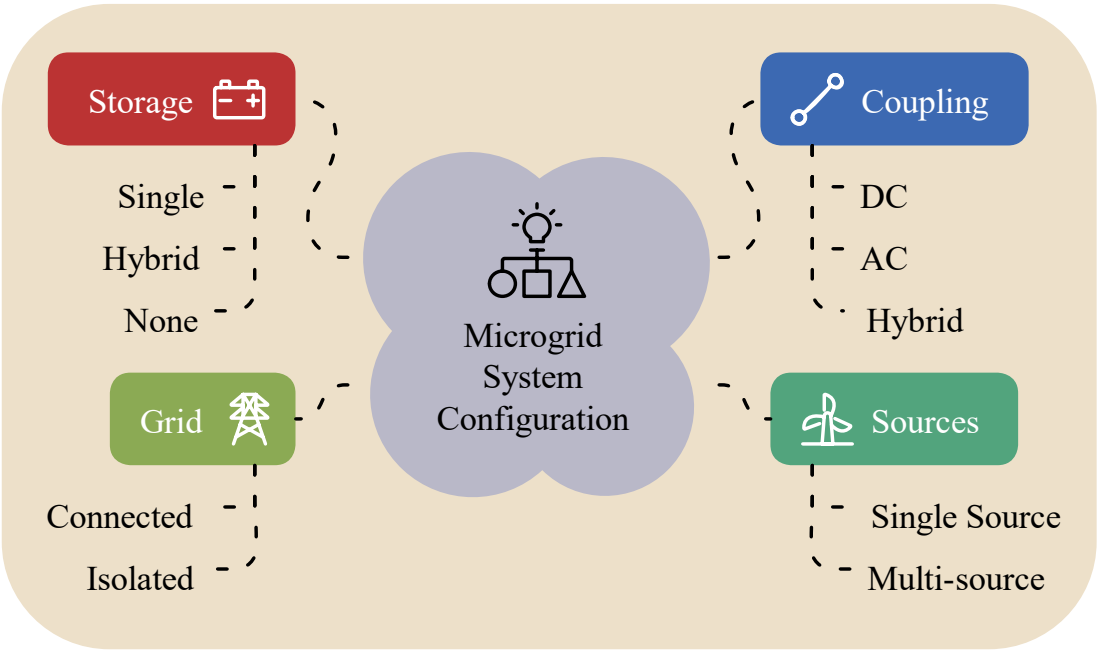

Figure I-10 : Microgrid Configuration.

I.7.1. Microgrid Operating Modes

Microgrids can operate in three primary modes, each serving different purposes depending on grid conditions, energy requirements, and operational objectives [70, 71]:

- **Grid-Connected Mode:**

In this mode, the microgrid remains connected to the main utility grid, exchanging power bidirectionally. The main grid serves as both a source and sink for energy, helping to stabilize frequency and voltage within the microgrid while also allowing for economic optimization of resources. During peak demand periods, the microgrid can import power from the main grid, while during excess generation, it can export power back to the grid.

- **Island Mode (Autonomous Mode):**

When disconnected from the main grid—either intentionally or due to faults in the utility network—the microgrid operates independently. This mode requires sophisticated control mechanisms to maintain stable frequency and voltage without the support of the main grid. Energy storage systems become critical during islanded operation to balance generation and demand, especially with intermittent renewable sources.

I.7.2. Microgrid Configurations

Microgrids can be classified based on their electrical architecture into three main configurations [72, 73]:

- **AC Microgrids:**

The traditional configuration where generation, distribution, and consumption operate with alternating current. AC microgrids interface easily with the conventional grid but may require multiple conversion stages for DC sources like photovoltaics and batteries.

- **DC Microgrids:**

These operate with direct current throughout the network, eliminating the need for synchronization and reactive power management. DC microgrids offer higher efficiency for systems with predominantly DC sources (solar PV, batteries) and loads (electronics, LED lighting), reducing conversion losses. However, they require specialized protection schemes different from conventional AC systems.

- **Hybrid AC/DC Microgrids:**

Combining both AC and DC subsystems connected through bidirectional converters, these configurations leverage the advantages of both architectures. AC sections can interface with the

main grid and traditional AC loads, while DC sections accommodate renewable sources and modern electronic loads with minimal conversion.

I.7.3. Energy Management Systems

Energy Management Systems (EMS) are essential for optimizing the performance of microgrids by coordinating power generation, storage, and consumption. An EMS ensures efficient utilization of resources while maintaining system stability and economic operation [74].

EMS Functions

- **Real-Time Power Flow Optimization:** Balances energy supply and demand, minimizing reliance on external grid support.
- **State-of-Charge (SoC) Management:** Regulates battery charge and discharge cycles to extend battery life and improve efficiency.
- **Demand-Side Management:** Adjusts energy consumption dynamically based on available generation and load priorities.
- **Power Smoothing:** In the case of connection to the grid, it eliminates fluctuations and power disturbances by deploying generation and storage resources.

I.8. STUDIED DC-MICROGRID CONFIGURATION

The choice of a DC microgrid (DC-MG) configuration over its AC counterparts is primarily driven by its inherent advantages, including higher efficiency, reduced power losses, and simplified control mechanisms. DC-MGs facilitate the integration of renewable energy sources and energy storage systems more effectively than AC systems, making them particularly suitable for modern energy demands [75, 76].

Advantages of a DC Microgrid Configuration

- Reduced Conversion Losses: Unlike AC microgrids, a DC microgrid eliminates multiple conversion stages, improving overall energy efficiency.
- Integration of Renewable Sources: DC-MGs can seamlessly integrate various renewable energy sources, such as photovoltaic systems and fuel cells, enhancing sustainability
- Simplified Integration with DC Loads: Most modern devices, such as LED lighting, data centers, and electric vehicles, operate on DC power, making direct integration more efficient.

- Improved System Stability: The centralized energy management system (EMS) dynamically controls power distribution, optimizing generation, storage, and load balancing.
- Higher Efficiency: DC-MGs exhibit lower energy losses due to the absence of reactive power, which is prevalent in AC systems

DC microgrids are particularly advantageous for remote communities, industrial applications, and smart city infrastructures due to their high efficiency, reliability, and compatibility with renewable energy technologies.

I.8.1. Literature Review on DC-Microgrid

Recent research highlights diverse DC-microgrid architectures optimized for various operational settings and energy sources, as demonstrated by several seminal works. This review focuses on the design approaches of these microgrids, examining key studies in the field. These works collectively explore the integration of renewable energy and storage solutions in both isolated and grid-connected DC systems.

Many studies focus on isolated DC-microgrids powered by renewable sources like PV [77-80], wind and tidal energy [81, 82], or a combination thereof [82, 83]. These systems often incorporate hybrid energy storage, combining batteries, supercapacitors, and fuel cells to ensure reliable power and voltage stability. Examples include PV-battery systems [77], PV with battery and supercapacitor [78, 79], wind-tidal systems with battery, fuel cell, electrolyzer, and diesel generator [81], and configurations with hydrogen storage [80]. These isolated microgrids consistently deliver power to DC loads via a shared bus.

Research also explores connected DC-microgrids utilizing wind and solar energy, often with battery and hydrogen storage for energy management [84, 85]. These hybrid DC-microgrid systems, as proposed by researchers like Sahri et al. and Tamalouzt et al., demonstrate the potential of renewable energy and advanced storage to provide reliable, efficient, and sustainable decentralized energy solutions for both standalone and interconnected applications.

I.8.2. Proposed DC-Microgrid System

Building on these previous works, our studied DC-microgrid configuration, as illustrated in Figure I-11, consists of:

- Wind Energy Conversion System (WECS-DFIG).
- Photovoltaic (PV) System.

- Battery Energy Storage System (BESS).
- Fuel Cell.

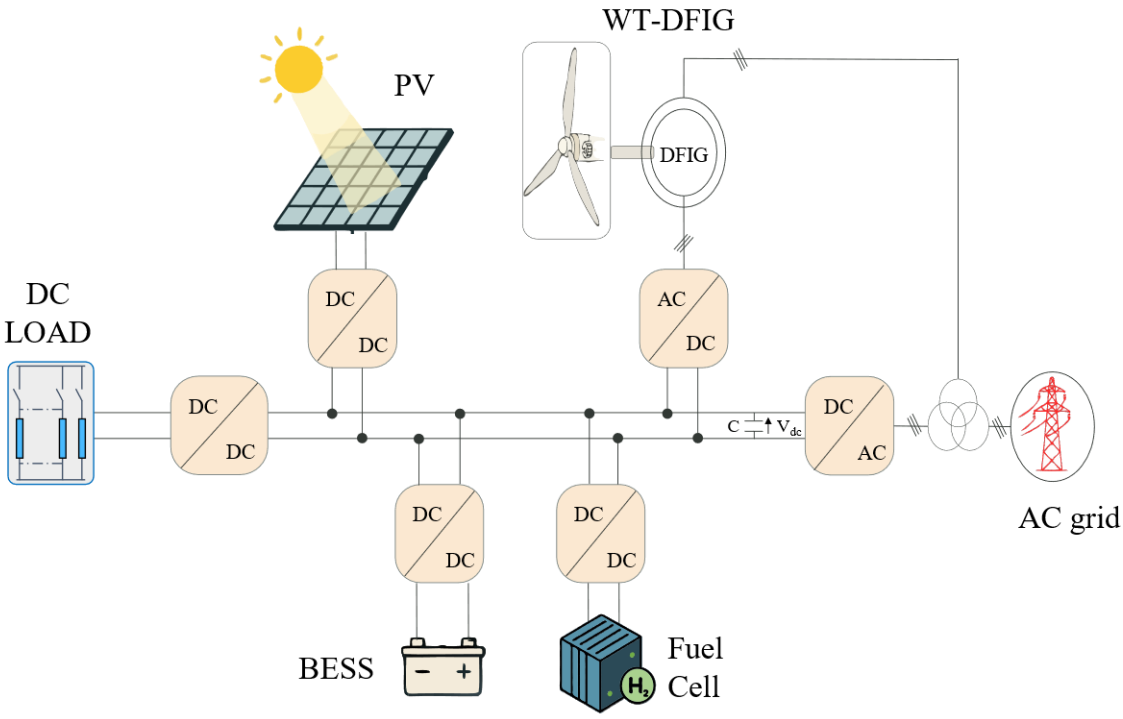

Figure I-11: Proposed DC Microgrid.

This configuration leverages complementary generation profiles and storage capabilities to ensure reliable power supply under varying environmental conditions.

The DC link of the DFIG's back-to-back converter is the integration point for the microgrid's other components. The PV array connects to this DC link through a converter that uses MPPT. The BESS interfaces through a DC-DC converter to enable charging when there is excess generation and discharging when there is a deficit. Similarly, the FC system connects via a unidirectional power conditioning system to supplement generation during periods of low renewable output.

This integrated approach using the DFIG's DC link as the common connection point offers several system-level advantages:

- **Simplified architecture:** Eliminates the need for additional AC-DC conversion stages that would be required in conventional AC microgrid configurations.
- **Improved coordination:** Facilitates direct power balancing among all sources and storage element at the DC level before grid interaction.

- **Enhanced controllability:** Enables the grid-side converter to manage the aggregate power flow between the entire microgrid and the main grid, providing a single control point for grid support functions.
- **Increased efficiency:** Reduces the total number of power conversion stages, decreasing overall system losses.

I.9. CONCLUSION

The chapter laid the foundation for the thesis by examining energy issues worldwide and the necessity for renewable energy. It discussed wind and solar energy technologies, focusing on wind energy conversion systems and photovoltaic arrays, and covered technologies for energy provision, including batteries for direct storage and fuel cells for converting stored fuel to electricity. The chapter also highlighted the shortcomings of traditional control strategies for DFIG systems and explained the importance of exploring AI-based approaches. It also discussed microgrid architectures, emphasizing the efficiency of DC microgrids in integrating renewable

II

MODELING OF MICROGRID COMPONENTS

II.1. INTRODUCTION

This chapter presents a comprehensive and in-depth modeling of the key components constituting a DC-microgrid system. The system under study integrates multiple renewable energy sources and storage device, namely wind turbines equipped with doubly fed induction generators (WT-DFIG), photovoltaic (PV) systems, electrical energy storage elements such as batteries, power generation units like fuel cells utilizing stored hydrogen, and associated power electronic interfaces. The objective of this chapter is to establish precise mathematical and simulation models that reflect the operational dynamics of each component under various environmental and load conditions. The development of such detailed models serves as the foundational basis for the subsequent construction of robust control algorithms and intelligent energy management strategies.

II.2. WIND TURBINE BASED ON DOUBLE FED INDUCTION GENERATOR MODELING

II.2.1. Mechanical Subsystem Modeling

This section presents the mathematical models used to describe the mechanical components of the Wind Energy Conversion System (WECS). These components, including the wind turbine rotor interacting with the wind, the gearbox, and the generator shaft, are visually represented in the schematic shown in Figure II-1. These models underpin the dynamic analysis and control strategies developed in later sections.

II.2.1.1. Aerodynamic Model

The turbine rotor extracts kinetic energy from the wind. The theoretical power available in the wind (P_v) passing through the rotor swept area (A_t) is given by [86]:

$$P_v = 0.5\rho A_t v^3 \quad \text{(II-1)}$$

The actual mechanical power (P_{mech}) captured depends on the power coefficient (C_p), which is a function of the tip-speed ratio (λ) and the blade pitch angle (β):

$$P_{mech} = 0.5\,\rho A_t C_p(\lambda,\beta) v^3 \quad \text{(II-2)}$$

The tip-speed ratio (λ) is defined as:

$$\lambda = \frac{R_t \Omega_t}{v} \quad \text{(II-3)}$$

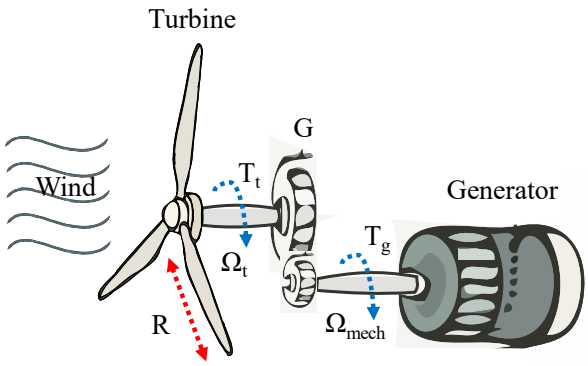

Figure II-1: Schematic of Wind Turbine Mechanical Components.

The aerodynamic torque (T_t) generated on the low-speed shaft is the mechanical power divided by the rotor speed:

$$T_t = \frac{P_{mech}}{\Omega_t} \quad \text{(II-4)}$$

For simulation purposes, the power coefficient $C_p(\lambda,\beta)$ is often approximated using empirical formulas derived from wind tunnel tests or blade element momentum (BEM) theory calculations [61, 62]:

$$C_P(\lambda,\beta) = C_1\left[C_2\left(\lambda_i^{-1}\right) - C_3\beta - C_4\right]e^{\left(C_5\lambda_i^{-1}\right)} + C_6\lambda_i \quad \text{(II-5)}$$

Where the intermediate variable λ_i is calculated as:

$$\lambda_i^{-1} = \frac{1}{\lambda + a\beta} - \frac{b}{1+\beta^3} \quad \text{(II-6)}$$

The coefficients a, b and C_1 to C_6 are specific parameters for the turbine's aerodynamic characteristics. This formulation models the distinct non-linear connection among C_p, λ, and β . As

illustrated by the characteristic curves in Figure II-2, this relationship results in a maximum power coefficient $C_{p,max}$ (often around 0.48-0.59) at an optimal tip-speed ratio λ_{opt} when is β at its 0 degrees.

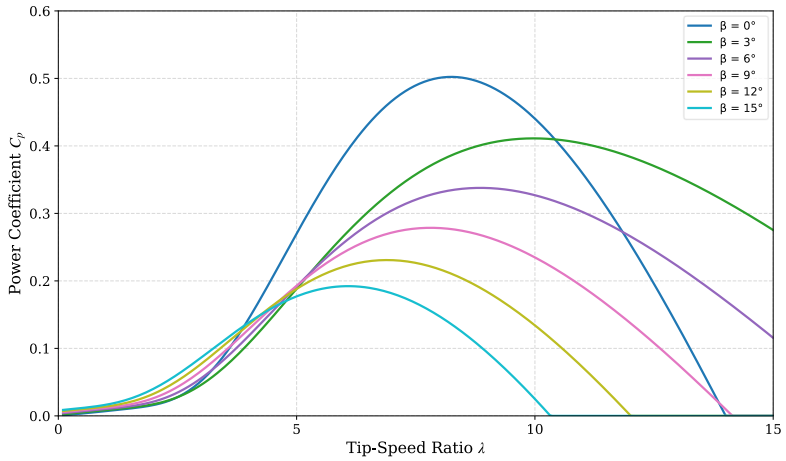

Figure II-2: Characteristic Power Coefficient (C_p) Curves as a Function of Tip-Speed Ratio (λ) and Pitch Angle (β).

II.2.1.2. Drivetrain Model

The drivetrain transmits the mechanical torque from the low-speed turbine shaft to the high-speed generator shaft. It typically includes a gearbox to increase the rotational speed and corresponding shafts.

- **Gearbox Model**

Assuming an ideal gearbox with ratio G. The gearbox increases the rotational speed from the low-speed shaft (Ω_t) to the high-speed shaft (Ω_{mech}) connected to the generator [87]. Neglecting losses:

$$\begin{cases} \Omega_t = \frac{\Omega_{mech}}{G} \\ T_g = \frac{T_t}{G} \end{cases} \quad \text{(II-7)}$$

- **Inertia and Dynamics**

A simplified representation of the drivetrain, often conceptualized as the two-mass model shown in Figure II-3 (including turbine inertia J_t, generator inertia J_g, gearbox G, and friction f_v), helps in understanding its dynamics. The rotational dynamics of the system, referred to the high-speed shaft, are governed by Newton's second law, considering the equivalent inertia J [88]:

$$J\frac{d\Omega_{mech}}{dt} = T_g - T_{em} - T_f \quad \text{(II-8)}$$

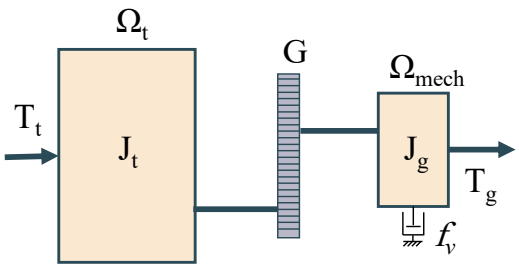

Figure II-3 : Simplified Drivetrain Model.

The equivalent inertia J combines the generator inertia J_g and the turbine inertia J_{tur} reflected through the gearbox:

$$J = J_g + \frac{J_t}{G^2} \tag{II-9}$$

In Eq. II-8, T_{em} is the electromagnetic torque produced by the generator, and T_f represents drivetrain frictional losses, often modeled as viscous friction:

$$T_f = f_v \, \Omega_{mech} \tag{II-10}$$

These equations (II-1) through (II-10) define the mechanical dynamics of the WECS by linking wind speed to generator shaft speed. This comprehensive model serves as the foundation for system-level simulation, dynamic analysis, and control design. The block diagram in Figure II-4 is derived from these equations to show the flow of energy and dynamic interactions within the mechanical subsystem.

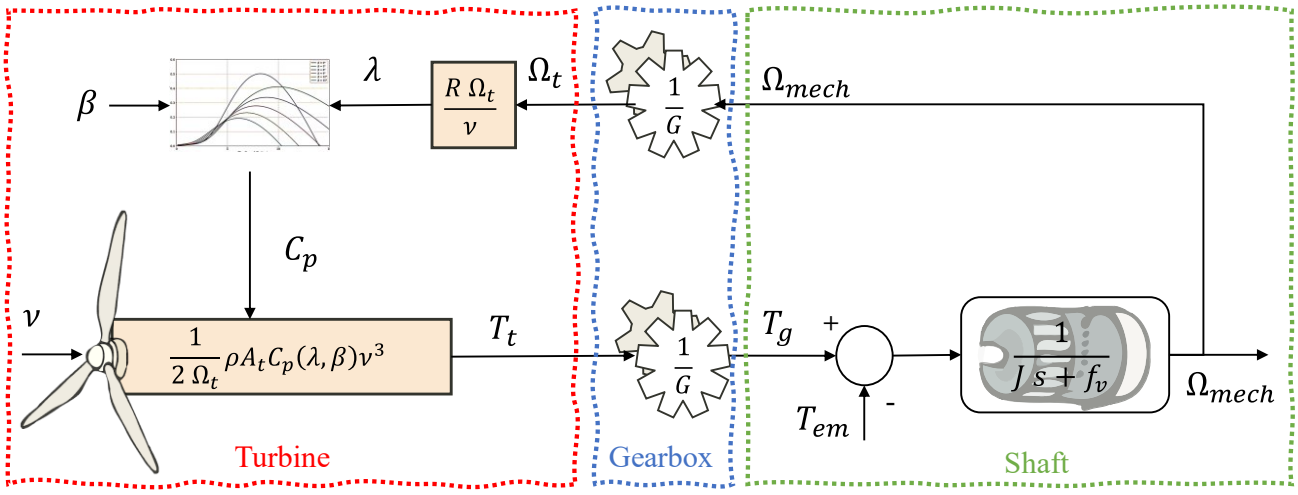

Figure II-4:Block Diagram Representation of the Wind Energy Conversion System (WECS) Mechanical Model.

II.2.2. Electrical Subsystem Modeling

The section develops the mathematical model for the doubly-fed induction generator (DFIG), a critical component in many variable-speed wind turbines. Accurate modeling is essential for design. The initial step involves the establishment of simplifying assumptions and the delineation of the model's inherent complexity in its three-phase coordinates. This complexity is a fundamental motivation for the implementation of reference frame transformations.

II.2.2.1. Simplifying Assumptions

To make the DFIG model tractable while retaining its essential dynamics, the following standard assumptions are employed [60, 87]:

- Negligible slot harmonics and skin effect in conductors.
- Iron losses (hysteresis and eddy currents) are ignored.
- Linear magnetic circuit (no saturation).
- Uniform air gap between the stator and rotor.
- Identical resistances for all three stator windings (R_s) and all three rotor windings (R_r).
- Sinusoidally distributed magnetomotive forces (MMF) in the air gap.
- Constant machine parameters (no temperature effects considered).

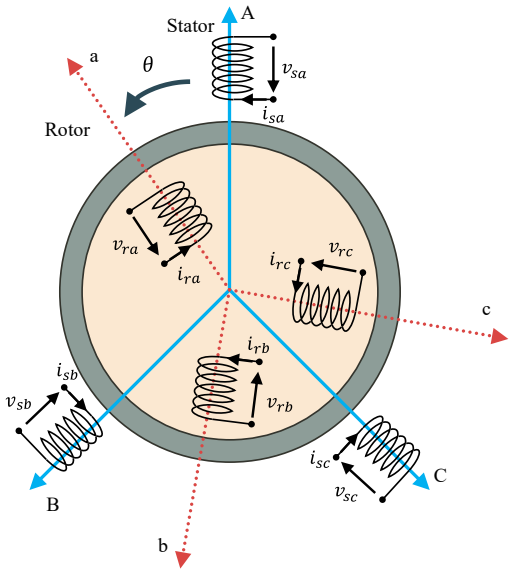

Figure II-5: Schematic Diagram of Doubly-Fed Induction Generator (DFIG) Windings.

II.2.2.2. DFIG Modeling in the Natural (abc) Reference Frame

Directly modeling the DFIG using its physical three-phase stator (sa, sb, sc) and rotor (ra, rb, rc) variables leads to a complex system description. A schematic diagram showing the DFIG (Doubly-Fed Induction Generator) with stator and rotor windings is shown in Figure II-5, and the corresponding voltage equations are as follows [61, 88]:

Stator:

$$\begin{cases} v_{sa} = R_s i_{sa} + \frac{d\varphi_{sa}}{dt} \\ v_{sb} = R_s i_{sb} + \frac{d\varphi_{sb}}{dt} \\ v_{sc} = R_s i_{sc} + \frac{d\varphi_{sc}}{dt} \end{cases} \quad \text{(II-11)}$$

Rotor:

$$\begin{cases} v_{ra} = R_r i_{ra} + \frac{d\varphi_{ra}}{dt} \\ v_{rb} = R_r i_{rb} + \frac{d\varphi_{rb}}{dt} \\ v_{rc} = R_r i_{rc} + \frac{d\varphi_{rc}}{dt} \end{cases} \quad \text{(II-12)}$$

The complexity arises primarily from the flux linkage equations (φ), where the mutual inductances between stator and rotor phases depend explicitly on the instantaneous electrical angle (θ) of the rotor:

$$\begin{cases} [\varphi_{s(abc)}] = [L_{ss}][i_{s(abc)}] + [M_{sr(\theta)}][i_{r(abc)}] \\ [\varphi_{r(abc)}] = [L_{rr}][i_{r(abc)}] + [M_{rs(\theta)}][i_{s(abc)}] \end{cases} \quad \text{(II-13)}$$

The self-inductance matrices ($[L_{ss}]$, $[L_{rr}]$) and mutual inductance matrices ($[M_{sr}]$, $[M_{rs}]$) are:

$$[L_{ss}] = \begin{bmatrix} l_s & m_s & m_s \\ m_s & l_s & m_s \\ m_s & m_s & l_s \end{bmatrix}; \qquad [L_{rr}] = \begin{bmatrix} l_r & m_r & m_r \\ m_r & l_r & m_r \\ m_r & m_r & l_r \end{bmatrix};$$

$$[\mathrm{M_{sr}}] = [\mathrm{M_{rs}}]^{\mathrm{T}} = \mathrm{M_0} \begin{bmatrix} \cos(\theta) & \cos\left(\theta + \frac{2\pi}{3}\right) & \cos\left(\theta + \frac{4\pi}{3}\right) \\ \cos\left(\theta + \frac{4\pi}{3}\right) & \cos(\theta) & \cos\left(\theta + \frac{2\pi}{3}\right) \\ \cos\left(\theta + \frac{2\pi}{3}\right) & \cos\left(\theta + \frac{4\pi}{3}\right) & \cos(\theta) \end{bmatrix}; \quad \text{(II-14)}$$

Where $[L_{ss}]$and $[L_{rr}]$ are matrices of constant self and mutual inductances within the stator and rotor respectively, but $[M_{sr(\theta)}]$ and $[M_{rs(\theta)}]$ contain sinusoidal terms involving θ This dependence on rotor position results in time-varying parameters in the differential equations, significantly complicating analysis and control design.

II.2.2.3. DFIG Modeling in Park's Reference Frames

Park's transformation is employed to overcome the complexity of the ABC model. This mathematical tool converts the variables into an equivalent system rotating at a chosen reference speed. With an appropriate reference frame, time-varying terms are eliminated, resulting in a constant model [60, 89]. Common frames include:

II.2.2.3.1. Synchronously Rotating Reference Frame

This frame rotates at synchronous speed (ω_s) and converts time-varying AC quantities to steady state DC values. It simplifies control system design by making key variables such as flux and torque constant, which is particularly useful for Field-Oriented Control (FOC). Despite the transformation, the full dynamics of the machine are preserved.

The stator and rotor voltage equations become:

$$\begin{aligned}
\frac{d\varphi_{sd}}{dt} &= v_{sd} - R_s i_{sd} + \omega_s \varphi_{sq} \\
\frac{d\varphi_{sq}}{dt} &= v_{sq} - R_s i_{sq} - \omega_s \varphi_{sd} \\
\frac{d\varphi_{rd}}{dt} &= v_{rd} - R_r i_{rd} + (\omega_s - \omega) \varphi_{rq} \\
\frac{d\varphi_{rq}}{dt} &= v_{rq} - R_r i_{rq} - (\omega_s - \omega) \varphi_{rd}
\end{aligned} \quad \text{(II-15)}$$

Flux Linkage Equations:

$$\begin{aligned}
\varphi_{sd} &= L_s\, i_{sd} + M\, i_{rd} \\
\varphi_{sq} &= L_s\, i_{sq} + M i_{rq} \\
\varphi_{rd} &= L_r i_{rd} + M\, i_{sd} \\
\varphi_{rq} &= L_r\, i_{rq} + M\, i_{sq}
\end{aligned} \quad \text{(II-16)}$$

With $L_s = l_s + m_s, L_r = l_r + m_s,$ and $M = 3/2M_0$.

II.2.2.3.2. Stationary Reference Frame

Fixed to the stator, this frame uses real-time voltage and current measurements without transformation. It simplifies the equations on the stator side and is particularly useful for transient studies such as startup, braking, or fault conditions, while maintaining full time-domain dynamics.

The stator and rotor voltage equations become:

$$\begin{aligned}\frac{d\varphi_{s\alpha}}{dt} &= v_{s\alpha} - R_s i_{s\alpha}\\ \frac{d\varphi_{s\beta}}{dt} &= v_{s\beta} - R_s i_{s\beta}\\ \frac{d\varphi_{r\alpha}}{dt} &= v_{r\alpha} - R_r i_{r\alpha} - \omega\,\varphi_{r\beta}\\ \frac{d\varphi_{r\beta}}{dt} &= v_{r\beta} - R_r i_{r\beta} + \omega\,\varphi_{r\alpha}\end{aligned} \quad \text{(II-17)}$$

Flux Linkage Equations:

$$\begin{aligned}\varphi_{sd} &= L_s\, i_{sd} + M\, i_{rd}\\ \varphi_{sq} &= L_s\, i_{sq} + M i_{rq}\\ \varphi_{rd} &= L_r i_{rd} + M\, i_{sd}\\ \varphi_{rq} &= L_r\, i_{rq} + M\, i_{sq}\end{aligned} \quad \text{(II-18)}$$

II.2.2.3.3. Rotor Reference Frame

Aligned with the rotor's position, this frame simplifies rotor-side equations by eliminating relative motion terms. While it adds speed-related terms to the stator equations, it's advantageous for control strategies requiring rotor position or speed feedback.

The stator and rotor voltage equations become:

$$\begin{aligned}\frac{d\varphi_{s\alpha}}{dt} &= v_{s\alpha} - R_s i_{s\alpha} + \omega\,\varphi_{s\beta}\\ \frac{d\varphi_{s\beta}}{dt} &= v_{s\beta} - R_s i_{s\beta} - \omega\,\varphi_{s\alpha}\\ \frac{d\varphi_{r\alpha}}{dt} &= v_{r\alpha} - R_r i_{r\alpha}\\ \frac{d\varphi_{r\beta}}{dt} &= v_{r\beta} - R_r i_{r\beta}\end{aligned} \quad \text{(II-19)}$$

Flux Linkage Equations:

$$\begin{aligned}\varphi_{sd} &= L_s\, i_{sd} + M\, i_{rd}\\ \varphi_{sq} &= L_s\, i_{sq} + M i_{rq}\\ \varphi_{rd} &= L_r i_{rd} + M\, i_{sd}\\ \varphi_{rq} &= L_r\, i_{rq} + M\, i_{sq}\end{aligned} \quad \text{(II-20)}$$

II.3. PHOTOVOLTAIC SYSTEM MODELING

PV systems convert solar energy directly into DC electricity through the photovoltaic effect in semiconductor materials. Modeling their output characteristics under varying environmental conditions (solar irradiance and temperature) is critical for the design of MPPT algorithms and overall energy management in the microgrid.

II.3.1. PV Cell Equivalent Circuit Model

PV cells are described by a single-diode model, shown in Figure II-6. This model treats the cell as a nonlinear current source and uses a current-voltage equation that combines the photocurrent from light, the rectifying behavior of the p-n junction (modeled by an ideal diode), and the impact of parasitic resistances [90].

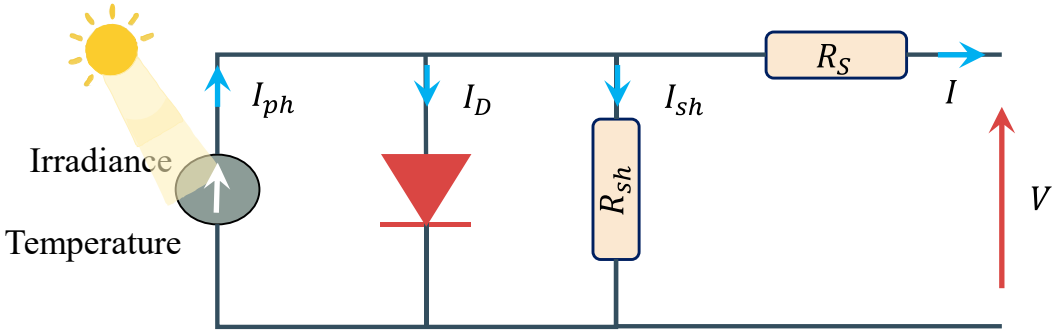

Figure II-6 : Single-Diode Equivalent Circuit Model of a Photovoltaic (PV) Cell.

This circuit includes:

- A current source (I_{ph}) representing the photogenerated current, directly proportional to solar irradiance.
- A diode (D) representing the p-n junction characteristics.
- A series resistance (R_s) accounting for ohmic losses in contacts and semiconductor material.
- A shunt resistance (R_{sh}) representing leakage currents across the p-n junction.

The terminal behavior of the PV cell, defined by the relationship between its output current (I) and voltage (V), is mathematically described by a transcendental equation derived from applying Kirchhoff's current law to the equivalent circuit model. The standard form of this equation is given by [91]:

$$I = I_{\text{ph}} - I_0 \left[\exp\left(\frac{V+IR_s}{nV_t}\right) - 1\right] - \frac{V+IR_s}{R_{\text{sh}}} \qquad \text{(II-21)}$$

The photocurrent itself is dependent on both the ambient irradiance and the operating temperature, and is defined by:

$$I_{ph} = \left[I_{sc-ref} + K_I\,(T - Tref)\right] \cdot \frac{G}{G_{ref}} \quad \text{(II-22)}$$

II.3.2. Main Operational Parameters: Short-Circuit Current and Open-Circuit Voltage

Two critical parameters derived from the I-V characteristic curve define the operational boundaries of the PV cell under specific irradiance and temperature conditions [68]:

- **Short-Circuit Current** (I_{sc})**:** The maximum current delivered by the cell when the voltage across its terminals is zero ($V = 0$). Ideally, $I_{sc} \approx I_{ph}$.
- **Open-Circuit Voltage** (V_{oc})**:** The maximum voltage across the cell terminals when the current is zero ($I = 0$). V_{oc} is highly dependent on temperature and the diode saturation current.

The typical Current-Voltage (I-V) and Power-Voltage (P-V) characteristic curves, illustrating these parameters and the Maximum Power Point (MPP), are shown in Figure II-7.

The variations of I_{sc} and V_{oc} with temperature and irradiance are critical to understanding PV system performance under varying environmental conditions:

- **Irradiance** (G): As irradiance increases, I_{sc} rises nearly linearly while V_{oc} increases logarithmically.
- **Temperature** (T): An increase in temperature typically leads to a modest rise in I_{sc}; however, V_{oc} experiences a substantial decline. This reduction in V_{oc} adversely affects the overall efficiency of the PV cell.

Figure II-8 illustrates the impact of varying irradiance and temperature on the PV cell's I-V characteristics, visually confirming the trends described above.

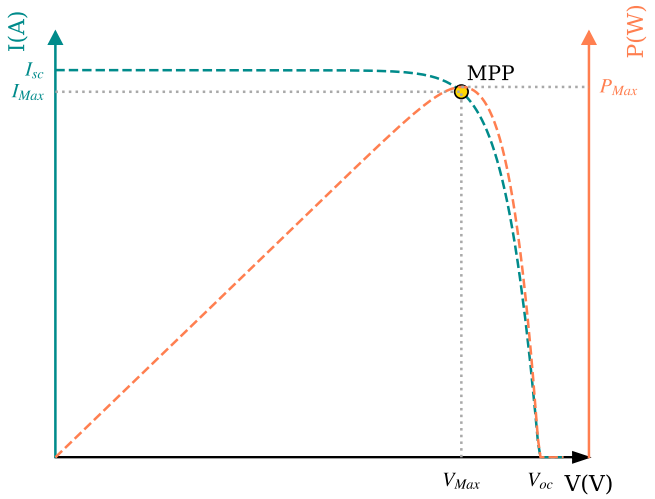

Figure II-7: Typical I-V and P-V Characteristic Curves of a PV cell.

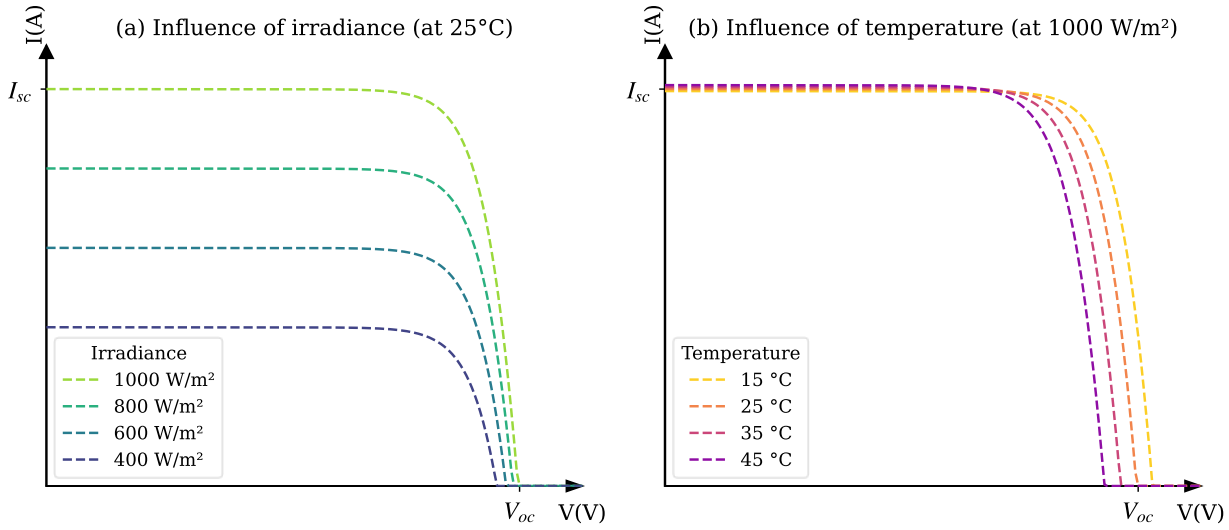

Figure II-8 : Influence of (a) Irradiance and (b) Temperature on PV cell I-V Characteristics.

II.3.3. PV Module and Array Modeling

Figure II-9 depicts the hierarchical structure of a photovoltaic system, where individual cells are assembled into modules, which are then interconnected to form arrays. Since the voltage output of an individual PV cell (usually between 0.5–0.7 V) is insufficient for most applications, cells are interconnected in series and parallel to form modules and arrays:

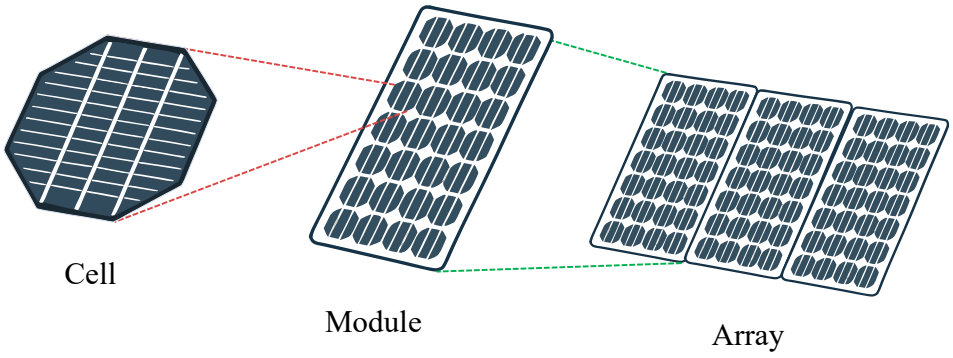

Figure II-9 : Hierarchical Structure of a Photovoltaic System (Cell, Module, Array).

- **Series Connection:** N_s cells in series increase the output voltage:

$$V_{module} = N_s V_{cell} \tag{II-23}$$

- **Parallel Connection:** N_p cells in parallel increase the output current:

$$I_{module} = N_p I_{cell} \tag{II-24}$$

At the array level, the combined output is determined by:

$$V_{array} = N_s V_{module}; I_{array} = N_p I_{module} \tag{II-25}$$

Where N_s and N_p represent the number of modules connected in series and parallel, respectively, at the array level.

II.3.4. Effect of Environmental Parameters

The performance of a PV system is highly dependent on environmental conditions, primarily solar irradiance and temperature.

- **Irradiance (G):** Increases in irradiance raise I_{ph} and, consequently, output current and power.
- **Temperature (T):** Higher temperatures reduce V_{oc} and V_{MPP}, degrading overall efficiency. Although I_{sc} may rise slightly, the negative temperature coefficient of voltage dominates.

II.4. BATTERY ENERGY STORAGE SYSTEM MODELING

Energy storage systems are foundational components in hybrid energy configurations, particularly for mitigating the intermittency inherent in renewable energy sources such as wind and

photovoltaic (PV) systems. Among the various energy storage technologies available, lead-acid batteries remain prevalent due to their cost-effectiveness, operational simplicity, and widespread availability. This section delineates the modeling approach, and operational considerations associated with lead-acid battery storage systems.

II.4.1. RC Equivalent Circuit Model

To represent the battery's electrical behavior, an equivalent circuit model (ECM) approach is adopted. For the system-level analysis undertaken in this thesis, a first-order Thevenin (or RC) model, illustrated in Figure II-10, is selected. This choice balances the need for representing key electrical characteristics, such as internal voltage drop and transient response, with the requirement for computational tractability within complex system simulations [92, 93]. More complex ECMs exist but were deemed unnecessary for the objectives of this study.

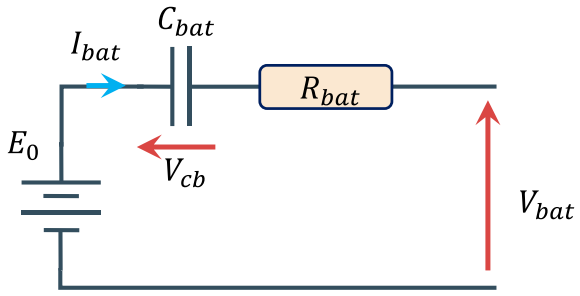

Figure II-10 :First-Order RC (Thevenin) Equivalent Circuit Model of a Battery.

- **Electromotive Force (E_0):** Denotes the terminal voltage of the battery when no load is applied.
- **Internal Resistance (R_{bat}):** Accounts for resistive losses during both charging and discharging processes.
- **Capacitive Element (C_{bat}):** Simulates the dynamic behavior of charge accumulation and release.

The relationship governing the terminal voltage of the battery is given by the following equation:

$$V_{bat} = E_0 - R_{bat} \cdot i_{bat} - V_{\mathrm{Cb}} \tag{II-26}$$

where V_{Cb} represents the voltage across the capacitor, representing the dynamic charge/discharge response.

II.4.2. State of Charge

The State-of-Charge (SOC) is a pivotal indicator of the battery's energy content, measured as a percentage of its total capacity. It provides essential information for monitoring energy availability, implementing control strategies, and ensuring safe operation of the energy storage system. The calculation of the SOC is determined by the following equation [68, 94]:

$$SOC = 1 - \frac{C_{cb}}{Q_a} \tag{II-27}$$

The SOC evolves dynamically during operation, offering real-time insights into battery performance under varying load and generation conditions.

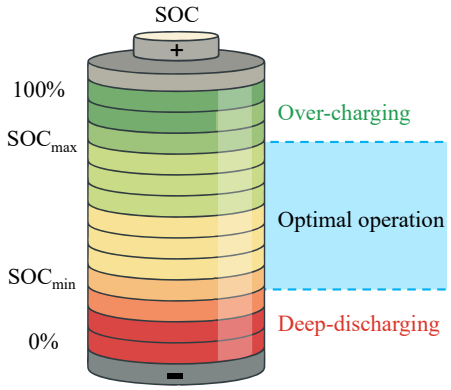

Figure II-11 : Battery State of Charge (SOC) Levels and Recommended Operating Range.

Maintaining the SOC within specified operational limits is crucial for extending the battery's lifespan and ensuring its health. These limits are typically defined by a minimum SOC (SOC_{min}) and a maximum SOC (lifespan). For instance, with lead-acid batteries, an optimal operating range of lead-acid batteries is often recommended between 20% SOC (SOC_{min}) and 80% SOC (lifespan) [68, 94]. Operating the battery below SOCmin (deep discharge) or above SOCmax (overcharge) can lead to accelerated degradation, reduced cycle life, and potential safety issues. Figure II-11 visually represents these operational zones in relation to the battery's State of Charge. Effective energy management strategies rely heavily on accurate SOC estimation and adherence to these operational boundaries.

II.5. FUEL CELL SYSTEM MODELING

Fuel cells are critical components in the power generation sector of hybrid energy systems, offering high efficiency energy conversion with minimal environmental impact. These electrochemical devices directly convert chemical energy from fuel (typically hydrogen) into

electrical energy through oxidation reactions. This section delineates the modeling approach and operational considerations associated with Proton Exchange Membrane Fuel Cells (PEMFCs), which are particularly suitable for distributed generation applications due to their low operating temperatures and quick start-up capabilities.

II.5.1. PEMFC Electrochemical Model

To simulate the behavior of a PEMFC stack under varying operating conditions, a mathematical model that accounts for both static and dynamic characteristics is utilized. The terminal voltage of a single PEMFC cell (V_{cell}) can be expressed as [95, 96]:

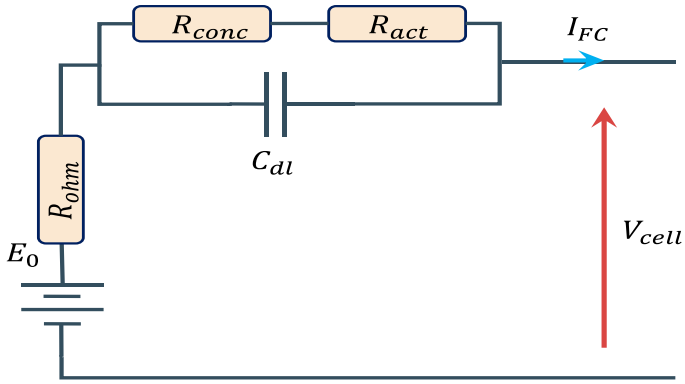

Figure II-12 :Equivalent Electrical Circuit Model of a PEM Fuel Cell.

$$V_{cell} = E_{Nernst} - V_{act} - V_{ohm} - V_{con} \quad \text{(II-28)}$$

An equivalent electrical circuit diagram representing the components contributing to the PEMFC terminal voltage, including static losses and the dynamic double-layer capacitance effect, is shown in Figure II-12.

II.5.1.1. Static Model Components

Static models describe the steady-state relationship between current and voltage, accounting for various losses.

- **Nernst Voltage** (E_{Nernst})**:** The theoretical maximum voltage, or Nernst potential, is derived based on operating temperature and reactant partial pressures:

$$E_{Nernst} = 1.229 - 0.85 \times 10^{-3}(T - 298.15) + 4.3085 \times 10^{-5} T \ln\left(P_{H_2} \cdot P_{O_2}^{0.5}\right) \quad \text{(II-29)}$$

Here, P_{H_2} and P_{O_2} are the partial pressures of hydrogen and oxygen, respectively.

- **Activation Loss (V_{act}):** This voltage drop arises due to the energy required to initiate chemical reactions at the electrodes. It is modeled using the Tafel equation:

$$V_{act} = \xi_1 + \xi_2 T + \xi_3 T \ln\left(C_{O_2}\right) + \xi_4 T \ln(I_{FC}) \quad \text{(II-30)}$$

Where $\xi_1, \xi_2, \xi_3, \xi_4$ are empirical coefficients, C_{O_2} is the oxygen concentration, and I_{FC} is the fuel cell current.

- **Ohmic Loss (V_{ohm}):** Ohmic losses stem from resistance in the membrane and electrodes:

$$V_{ohm} = I_{FC} \cdot (R_m + R_c) \quad \text{(II-31)}$$

Where R_m (ionic resistance) and R_c (electronic resistance) depend on material properties, including membrane hydration.

- **Concentration Loss (V_{con}):** At high current densities, reactant depletion at electrode surfaces causes voltage drops:

$$V_{con} = -\beta \ln(1 - J/J_{max}) \quad \text{(II-32)}$$

Where J is the current density and J_{max} is the maximum current density.

II.5.1.2. Dynamic Model

The transient behavior of a PEMFC is primarily attributed to the double-layer capacitance at the electrode-electrolyte interface. This dynamic effect is modeled using an equivalent RC circuit, where a capacitor represents the charge accumulation and release. As illustrated in Figure 2.5, this equivalent circuit model demonstrates the double-layer charging effect within a fuel cell [97].

This introduces a dynamic voltage term (V_d), governed by the following differential equation:

$$\frac{dV_d}{dt} = \frac{1}{C_{dl}} I_{FC} - \frac{1}{\tau} V_d \quad \text{(II-33)}$$

where C is the double-layer capacitance and τ is the characteristic time constant ($\tau = C \cdot (R_{act} + R_{con})$). Including this dynamic term, the total cell voltage becomes:

$$V_{cell} = E_{Nernst} - V_{act} - V_{ohm} - V_{con} - V_d \quad \text{(II-34)}$$

II.5.2. Fuel Cell Stack

In practical applications, a single PEMFC does not generate sufficient voltage or power output. To address this limitation, multiple individual cells are connected in series to form a fuel cell stack. This configuration enables the system to meet the requisite voltage and power levels.

The total stack voltage is computed as:

$$V_{FC_{stack}} = n_{cells} \cdot V_{cell} \tag{II-35}$$

Where n_{cells} denotes the number of cells in the stack.

II.6. POWER CONVERTER MODELING

Power electronic converters play a critical role in modern energy systems. The choice of modeling approach depends on the simulation objectives. A direct three-phase (abc) switching model is preferred when detailed switching behavior and high-frequency dynamics are important. Averaged models are used for control design and slower dynamic studies. This section presents a detailed switching model for the AC/DC/AC converter used with doubly fed induction generators (DFIGs). It also provides a contextual overview of averaged representations for DC/DC converters commonly used in energy conversion systems.

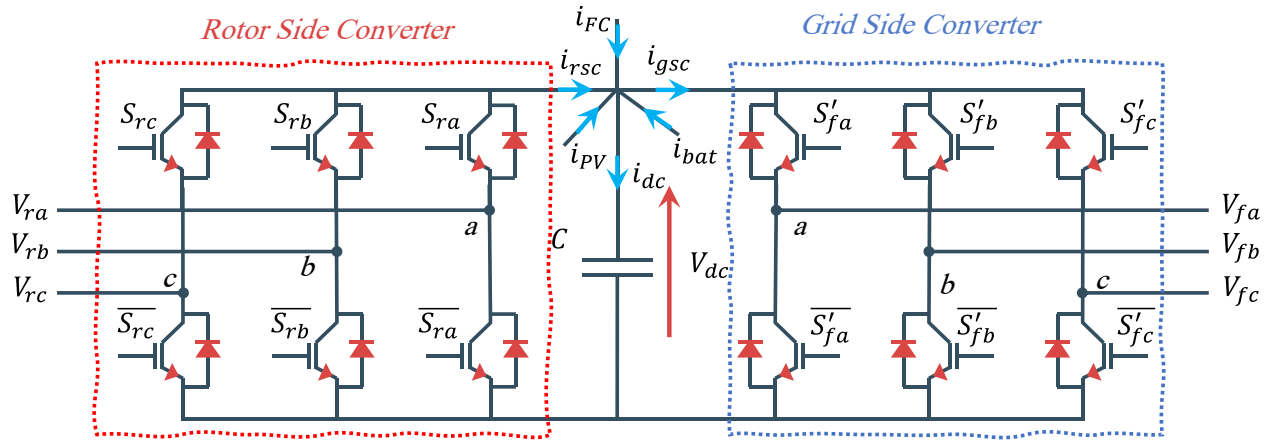

Figure II-13 : AC/DC/AC Back-to-Back Converter Configuration for DFIG.

II.6.1. AC/DC/AC Back-to-Back Converter Model

The interface between the DFIG rotor and the grid is typically implemented via an AC/DC/AC back-to-back converter, as illustrated schematically in Figure II-13. This system has two Voltage Source Converters (VSCs): the Rotor Side Converter (RSC), connected to the rotor slip rings, and the Grid Side Converter (GSC), connected to the grid via an AC filter. A capacitor

connects the DC sides of the two converters. Both converters use a three-phase, two-level topology with controllable.

II.6.1.1. Voltage Source Converters Modeling

Assuming ideal switches, the state of each converter leg (phase $j = a, b, c$) for a specific converter i (where $i = r$ for Rotor Side Converter, or $i = f$ for Grid Side Converter) can be defined by a Boolean switching function S_{ij}. For a two-level converter leg where the upper and lower switches operate complementarily:

$S_{ij} = 1$: Upper switch ON, lower switch OFF (AC terminal connected to positive DC rail).
$S_{ij} = 0$: Upper switch OFF, lower switch ON (AC terminal connected to negative DC rail).

Assuming a star connection and ideal switching behavior, the synthesized phase voltages relative to the local neutral point for each converter are given by [62]:

$$\begin{bmatrix} v_{ia} \\ v_{ib} \\ v_{ic} \end{bmatrix} = \frac{V_{dc}}{3} \begin{bmatrix} 2 & -1 & -1 \\ -1 & 2 & -1 \\ -1 & -1 & 2 \end{bmatrix} \begin{bmatrix} S_{ia} \\ S_{ib} \\ S_{ic} \end{bmatrix} \quad \text{(II-36)}$$

This formulation applies to both RSC and GSC independently by substituting the appropriate switching vector.

II.6.1.2. DC Link Modeling

The DC link is stabilized by a capacitor C, which smooths out voltage fluctuations caused by power exchanges between the RSC and the GSC. The dynamic equation for the DC bus voltage is [61]:

$$\mathrm{V_{dc}} = \frac{1}{C} \int \mathrm{i_{dc}} \mathrm{dt} \quad \text{(II-37)}$$

This equation represents the power balance between the two converters. Any power variation between the rotor and the grid directly affects the DC bus voltage.

II.6.2. DC/DC Converters

DC/DC converters are essential for integrating photovoltaic, battery, and fuel cells with the DC microgrid bus. They adjust voltage within the power system. The topologies used include Buck, Boost, and Bidirectional Buck–Boost converters to address variable voltage demands.

II.6.2.1. Boost Converter

The circuit topology for a typical DC/DC Boost converter is shown in Figure II-14. Used for PV or FC systems to step up a lower voltage source (V_{in}) to a higher DC bus voltage (V_{out}). averaged model of boost is [68]:

$$L\,\frac{dI_L}{dt} = V_{in} - (1 - d)\,V_{out} \tag{II-38}$$

Where I_L is the inductor current, d is the duty cycle of the main switch, L is the boost inductor.

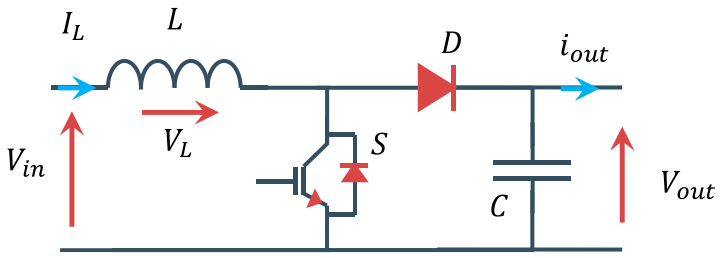

Figure II-14 : DC/DC Boost Converter Circuit Topology.

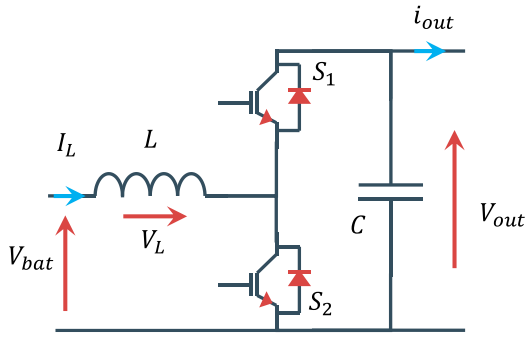

Figure II-15 : Bidirectional DC/DC Converter Topology.

II.6.2.2. Buck-Boost Converter

Figure II-15 shows a common topology for a bidirectional DC/DC converter, often used for battery interfacing. Allows bidirectional power flow and voltage step-up/down, suitable for interfacing batteries to a DC bus. Can be implemented using two switches or a bidirectional topology [68].

Let V_{bat} be the battery voltage and V_{dc} be the DC bus voltage. Depending on the control (duty cycle d), the converter facilitates charging (buck mode) or discharging (boost mode). During

charging, power flows from the DC bus to the battery, whereas during discharging, power flows from the battery to the DC bus.

- **Discharging Mode (Boost Mode):** In this mode, the converter steps up the battery voltage V_{bat} to match the higher DC bus voltage V_{dc}. The averaged model is expressed as:

$$L \frac{dI_L}{dt} = V_{bat} - (1 - d) V_{out} \quad \text{(II-39)}$$

- **Charging Mode (Buck Mode):** During charging, the converter steps down the DC bus voltage V_{dc} to match the lower battery terminal voltage V_{bat}. The averaged model is given by:

$$L \frac{dI_L}{dt} = (1 - d) V_{out} - V_{bat} \quad \text{(II-40)}$$

II.7. CONCLUSION

This chapter presents comprehensive mathematical models for the main components of a DC microgrid system. It covers renewable energy sources, energy storage units, and their interfacing power electronic converters. The analysis includes mechanical and electrical subsystems under various reference frames, providing a foundation for dynamic simulation and control design.

The photovoltaic (PV) system was rigorously modeled using a single-diode equivalent circuit, capturing the nonlinear influence of irradiance and temperature on output characteristics.

The battery energy storage system is represented using a Thevenin model, balancing complexity and efficiency. It discusses metrics such as State-of-Charge (SOC). The PEMFC model addresses static and dynamic behaviors. Finally, the modeling of AC/DC/AC and DC/DC converters provides insights into interfacing and controlling distributed energy resources within the microgrid system.

These models are fundamental for developing advanced control algorithms and energy management strategies, as discussed in subsequent chapters. Their accuracy and fidelity guarantee reliable, stable, and efficient DC microgrid system in various conditions.

III

CLASSICAL CONTROL STRATEGIES FOR DFIG-BASED WIND TURBINE SYSTEMS

III.1. INTRODUCTION

The integration of large-scale wind energy conversion systems (WECS) into electrical grids necessitates the implementation of sophisticated control strategies to ensure the efficient capture of energy, the maintenance of optimal power quality, and the assurance of grid stability. Due to its benefits, the Doubly-Fed Induction Generator (DFIG) is widely used in variable-speed wind turbines. However, DFIGs encounter challenges due to wind variability, necessitating the implementation of robust control systems for both the rotor-side (RSC) and grid-side (GSC) converters.

This chapter evaluates a classical control architecture for the WT-DFIG system, as modeled in Chapter II. The main control components include

- ✓ **The Maximum Power Point Tracking (MPPT)**, utilizing the Power Signal Feedback (PSF) technique, is employed in scenarios where wind speeds are below the rated level.
- ✓ **Pitch control** is achieved through the implementation of a PI regulator, which serves to restrict power output in circumstances where wind speeds exceed the rated levels.
- ✓ **The RSC control** utilizes conventional direct power control (C-DPC) to regulate generated active power (P_s) and the compensated local reactive power (Q_{AC}).
- ✓ **The GSC Control** employs C-DPC to regulate the DC-link voltage (V_{dc}) and the reactive power (Q_g) exchange between the GSC and the grid.

The chapter starts by describing the system configuration and the specific control objectives. It then covers the theoretical principles and math behind the PSF MPPT, PI Pitch control, and C-DPC methods for RSC and GSC. It then presents and analyzes simulation results using MATLAB/Simulink under operating scenarios to evaluate the performance of this classical scheme.

The chapter ends with a discussion of the limitations seen, especially those related to C-DPC, explaining the reason for the advanced, intelligent control methods explored in Chapter IV.

III.2. SYSTEM CONFIGURATION AND OVERALL CONTROL STRUCTURE

The WECS under consideration is composed of a horizontal-axis wind turbine that is coupled via a gearbox to a DFIG. The DFIG's stator windings are directly connected to the AC grid, while the rotor windings are connected to the grid through a back-to-back AC/DC/AC converter system. The system under consideration consists of the RSC, a DC-link capacitor (CDC), and the GSC, which is connected to the grid via an RL filter. The overall structure facilitates bidirectional power flow through the rotor circuit, enabling variable-speed operation and independent power control [62]. As illustrated in Figure III-1, the classical control system's architecture is depicted schematically.

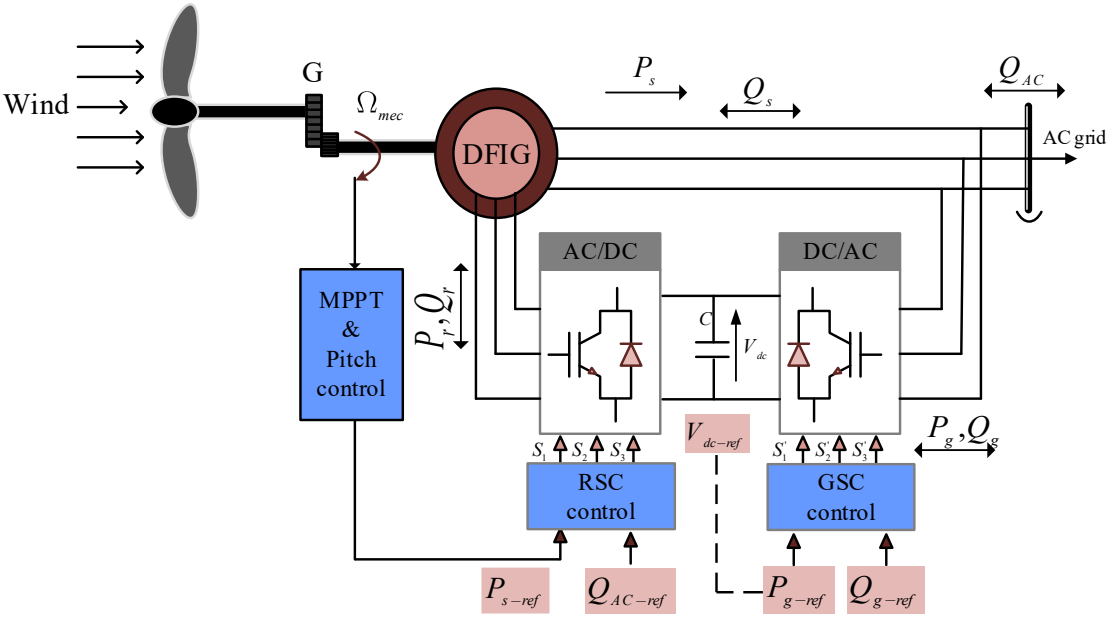

Figure III-1 : Overall Classical Control System Architecture.

The coordinated operation of the control subsystems aims to achieve the following objectives:

- **Optimize Power Capture:** Maximize P_m below rated wind speed using Maximum Power Point Tracking (MPPT), and limit P_m to its rated value above rated speed through pitch control to ensure safe and efficient operation.
- **Control Grid Power:** Ensure P_s tracks the reference derived from MPPT/Pitch control, and Q_{AC} tracks its independent reference (RSC function).
- **Stabilize DC Link:** Maintain V_{dc} at V_{dc-ref} (GSC function).

- **Ensure Grid Compatibility:** Control power Q_g,that injected to AC grid, to be zero for unity power factor operation of the GSC and ensure acceptable harmonic distortion levels in grid currents (GSC function).

III.3. WIND POWER OPTIMIZATION AND LIMITATION CONTROL

It is imperative to exercise effective control over the wind turbine's operating point, considering the range of wind speeds. This is crucial for optimizing energy yield while adhering to the system's physical limitations. The implementation of these strategies is contingent upon the operational zone.

III.3.1. Turbine Operation Zones

As shown in Figure III-2, variable-speed wind turbines operate in three zones. Very low wind speeds (zone I) prevent the turbine from turning. The "cut-in" speed is when the wind speed triggers the turbine to start generating power. The wind speed increases in the first zone, where the power generation is lower than the nominal power. In the second zone, the power generation changes from zone I's to zone III's maximum power. WT extracts the maximum power in both zones at a 0° blade pitch angle using the MPPT algorithm. The wind speed exceeds the nominal speed in zone III, and the pitch angle control system sets the output power limit to its nominal value. When the wind speed reaches its maximum limit in zone III, the DFIG rotor separates from the turbine to prevent turbine damage [98, 99].

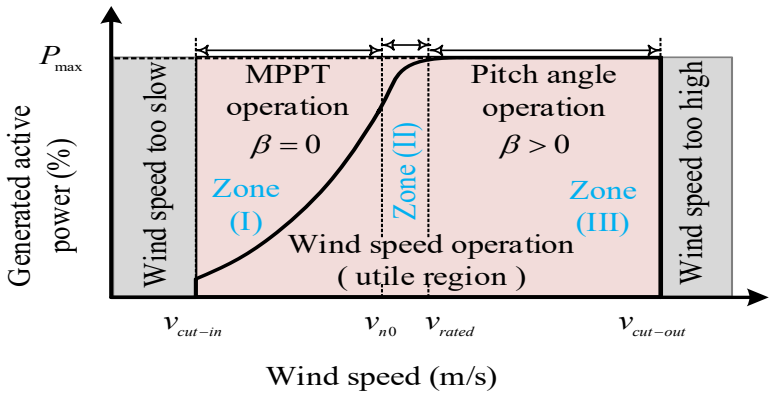

Figure III-2 : Wind Turbine Operating Zones.

III.3.2. Maximum Power Point Tracking

In Zones I and II, the objective of the control system is to extract the maximum possible power from the available wind. This objective is accomplished by employing MPPT algorithms,

which adjust the rotor speed based on the non-linear relationship between wind speed and aerodynamic power [99].

The Power Signal Feedback (PSF) method is a used industrial approach for MPPT [100].The system utilizes pre-defined optimal power curves, derived from simulations or experimental data, to calculate a reference power corresponding to the current wind speed. The actual power output is then compared with this reference, and the doubly-fed induction generator (DFIG) speed is adjusted accordingly.

The mechanical power P_m captured from the wind is related to the generator speed ω_m by [101]:

$$P_{\mathrm{m\_max}} = \frac{1}{2}\rho\pi R^5 \frac{C_{p\_\max}}{\lambda_{\mathrm{opt}}^3}\omega_{\mathrm{m}}^3 = K_{p\_\mathrm{opt}}\omega_{\mathrm{m}}^3 \quad \text{(III-1)}$$

III.3.3. Pitch Angle Control

In Zone III, when wind speeds exceed the rated value, the turbine is required to limit its power output to protect internal components, such as the generator and converters. This objective is accomplished using blade pitch angle regulation, a mechanism that curtails the aerodynamic torque and power capture by augmenting the pitch angle of the blades [98, 99].

To regulate the pitch angle β, a proportional-integral (PI) controller is utilized. The controller is designed to address the discrepancy between the actual and rated power values [61].

$$\frac{d\beta_{ref}}{dt} = K_p(P_{s-max} - P_s) + K_i \int (P_{s-max} - P_s)dt \quad \text{(III-2)}$$

Increasing the pitch angle β reduces the power coefficient C_p and the tip-speed ratio λ, maintaining the output power. This ensures the safety of the system and enables continued energy production within safe limits.

III.4. CLASSICAL CONTROL OF THE ROTOR SIDE CONVERTER USING C-DPC

The Rotor Side Converter (RSC) provides the interface for managing the DFIG's torque-speed characteristics and power flow. By injecting controlled voltages into the rotor windings, the RSC enables variable-speed operation and allows for the independent regulation of active and local reactive power components exchanged between the DFIG stator and the grid. The Conventional

Direct Power Control (C-DPC) strategy is applied for RSC control in this study, as depicted in Figure III-3.

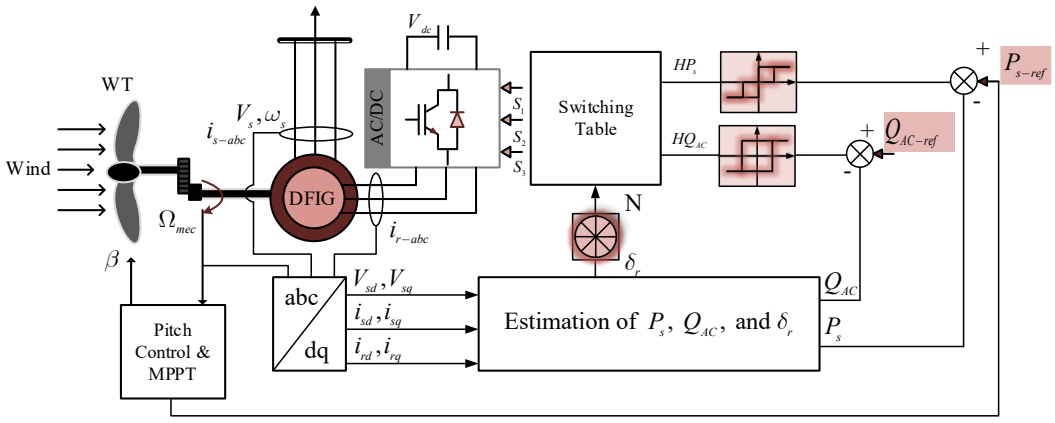

Figure III-3 : Block Diagram of RSC C-DPC Implementation.

III.4.1. Control Objectives and Strategy

The RSC manipulates the power flow from the rotor circuit, which directly influences the power injected by the stator into the grid. The main control objectives for the RSC using the C-DPC strategy are:

- **Active Power Regulation:** Ensure the stator active power (P_s) accurately tracks the reference value (P_{s-ref}) provided by the MPPT or Pitch Control algorithms (Section III.3).
- **Reactive Power Regulation:** Control the compensated local reactive power (Q_{AC}) to track its reference value (Q_{AC-ref}), which is set according to the prevailing reactive power demand of the system or connected loads.

The chosen strategy, DPC, aims to achieve these objectives directly by selecting appropriate RSC voltage vectors based on instantaneous power errors and the estimated position of the machine's flux vectors, bypassing the need for inner current control loops and complex coordinate transformations typically found in Field-Oriented Control (FOC) [102, 103].

III.4.2. Principle of Direct Power Control

Direct Power Control strategies for DFIGs rely fundamentally on the relationship between the active power (P_s) and reactive power (Q_{AC}) and the machine's flux linkage. Understanding this relationship is key to comprehending how manipulating the rotor voltage influences power flow. The expressions that link (P_s) and (Q_{AC}) to the magnitudes of the stator and rotor flux vectors ($|\varphi_s|, |\varphi_r|$) and the electrical angle (γ) between them are derived below.

The standard definition of instantaneous active and reactive powers in the stationary α-β reference frame is as follows:

$$\begin{aligned} P_s &= v_{s\alpha} i_{s\alpha} + v_{s\beta} i_{s\beta} \\ Q_{AC} &= v_{s\beta} i_{s\alpha} - v_{s\alpha} i_{s\beta} \end{aligned} \tag{III-3}$$

In a DFIG connected to a fixed grid, the stator voltage vector, denoted by the symbol $\overrightarrow{v_s}$, is principally imposed by the grid voltage. If stator resistance drop is neglected ($R_s \approx 0$), the stator voltage is directly related to the rate of change of stator flux. When the stator flux magnitude is constant $|\varphi_s|$ and rotating at synchronous speed, the stator voltage components approximate to [61]:

$$\begin{aligned} v_{s\alpha} &\approx -\omega_s \varphi_{s\beta} \\ v_{s\beta} &\approx \omega_s \varphi_{s\alpha} \end{aligned} \tag{III-4}$$

This emphasizes the orthogonal relationship between the voltage and flux vectors in steady state.

The flux linkages for the stator and rotor are defined as:

$$\begin{aligned} \varphi_{s\alpha} &= L_s i_{s\alpha} + M i_{r\alpha} \\ \varphi_{s\beta} &= L_s i_{s\beta} + M i_{r\beta} \\ \varphi_{r\alpha} &= L_r i_{r\alpha} + M i_{s\alpha} \\ \varphi_{r\beta} &= L_r i_{r\beta} + M i_{s\beta} \end{aligned} \tag{III-5}$$

By rearranging these equations, the stator currents can be expressed in terms of the flux components as:

$$\begin{aligned} i_{s\alpha} &= \frac{1}{\sigma L_s} \varphi_{s\alpha} - \frac{M}{\sigma L_s L_r} \varphi_{r\alpha} \\ i_{s\beta} &= \frac{1}{\sigma L_s} \varphi_{s\beta} - \frac{M}{\sigma L_s L_r} \varphi_{r\beta} \end{aligned} \quad ; \quad \text{where } \sigma = 1 - \frac{M^2}{L_s L_r} \tag{III-6}$$

Substituting the stator voltage approximations and the expressions for the stator currents into the power definitions leads to:

$$\begin{aligned} P_s &\approx \frac{\omega_s M}{\sigma L_s L_r} \left(\varphi_{s\beta} \varphi_{r\alpha} - \varphi_{s\alpha} \varphi_{r\beta} \right) \\ Q_s &\approx \frac{\omega_s}{\sigma L_s} |\varphi_s|^2 - \frac{\omega_s M}{\sigma L_s L_r} \left(\varphi_{s\alpha} \varphi_{r\alpha} + \varphi_{s\beta} \varphi_{r\beta} \right) \end{aligned} \tag{III-7}$$

The geometric interpretations of the dot and cross products in the $\alpha\beta$ plane are given by the following equations:

$$\begin{aligned}\overrightarrow{\phi_s}\cdot\overrightarrow{\phi_r} &= \phi_{s\alpha}\phi_{r\alpha}+\phi_{s\beta}\phi_{r\beta} = |\phi_s||\phi_r|\cos(\gamma)\\ \overrightarrow{\phi_s}\times\overrightarrow{\phi_r} &= \phi_{s\alpha}\phi_{r\beta}-\phi_{s\beta}\phi_{r\alpha} = |\phi_s||\phi_r|\sin(\gamma)\end{aligned} \quad \text{(III-8)}$$

where γ is the angle between the stator and rotor flux vectors. Substituting these into the power expressions yields [104]:

$$\begin{aligned}P_s &= -\frac{M}{\sigma L_s L_r}\omega_s|\phi_s||\phi_r|\sin(\gamma)\\ Q_s &= \frac{\omega_s}{\sigma L_s}|\phi_s|\left(|\phi_s|-\frac{M}{L_r}|\phi_r|\cos(\gamma)\right)\end{aligned} \quad \text{(III-9)}$$

It is evident from these expressions that the stator active power P_s is primarily influenced by the rotor flux magnitude $|\varphi_r|$ and the sine of the angle γ, while the reactive power Q_{AC} is controlled by $|\varphi_r|$ and the cosine of γ.

Equation III-9 reveals the core principle of DPC. Assuming the stator flux magnitude $|\varphi_s|$ is kept relatively constant:

- Active power (P_s) is directly influenced by the magnitude of the rotor flux $|\varphi_r|$ and the sine of the angle (γ) between the stator and rotor flux vectors.
- Reactive power (Q_{AC}) is influenced by $|\varphi_r|$ and the cosine of the angle (γ).

The DPC controller manipulates $|\varphi_r|$ and γ indirectly by applying specific voltage vectors (V_r) via the RSC. The relationship between the applied rotor voltage and the change in rotor flux is given by:

$$\varphi_r(t) = \int_0^t (v_r - R_r i_r)dt \quad \text{(III-10)}$$

Neglecting the rotor resistance term ($R_r\overrightarrow{i_r}$) for simplicity during short control intervals (ΔT), the change in rotor flux ($\Delta\overrightarrow{\varphi_r}$) is approximately:

$$\Delta\varphi_r = v_r\Delta T \quad \text{(III-11)}$$

This equation highlights that applying a specific rotor voltage vector $\overrightarrow{v_r}$ for a duration ΔT directly influences the change in the rotor flux vector. A standard two-level voltage source inverter, like the RSC, can typically generate eight discrete voltage vectors (six active vectors V_1 to V_6 of equal magnitude, and two zero vectors V_0, V_7), as illustrated in Figure III-4.

By selecting an appropriate voltage vector from these eight options, the controller can incrementally adjust the magnitude ($|\varphi_r|$) and position (affecting γ) of the rotor flux vector.

Consequently, according to Eq. III-9, this choice directly influences the stator active and reactive powers P_s and Q_s.

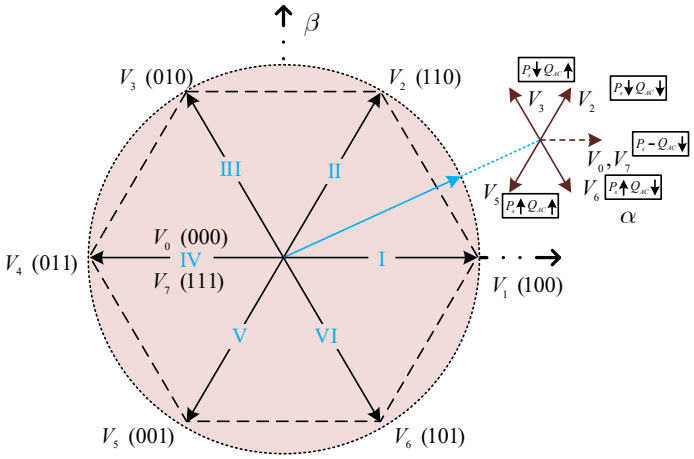

Figure III-4 : Vectors of output rotor voltage for GSC.

III.4.3. Implementation Components

The classical direct power control (C-DPC) scheme is predicated on the real-time selection of a voltage vector by the RSC. The determination is made through a comparison of the instantaneous errors between the reference values (P_{s-ref}, Q_{AC-ref}) and the estimated actual values (P_s, Q_{AC}). Frequently, the stator flux vector is utilized as a reference point for the determination of angular position.

The control procedure follows these main steps:

- **Estimation:** The following equations (Eqs. III-12 and III-13) are used to estimate produced active power, compensated local reactive power, rotor flux, and rotor angle. The grid voltage and rotor currents in the dq synchronous frame (i_{rd}, i_{rq} and V_s), as well as the synchronous pulsation (ω_s), are utilized to establish these estimates:

$$\begin{cases} P_s = -\frac{M}{L_s} V_s i_{rq} \\ Q_{AC} = \left[\frac{V_s^2}{L_s \omega_s} - V_s \frac{M}{L_s} i_{rd}\right] \end{cases} \quad \text{(III-12)}$$

$$\begin{cases} \varphi_{rd} = \left(1 - \frac{M^2}{L_s L_r}\right) L_r i_{rd} + \frac{M}{L_s} \\ \varphi_{rq} = \left(1 - \frac{M^2}{L_s L_r}\right) L_r i_{rq} \\ \theta_r = \tan^{-1}\left(\frac{\varphi_{r\beta}}{\varphi_{r\alpha}}\right) \end{cases} \quad \text{(III-13)}$$

- **Power Error Calculation:** The estimated powers are compared to their respective reference values (P_{s-ref}, Q_{AC-ref}) to determine the power errors:

$$eP_s = P_{s-ref} - P_s\,; \quad eQ_{AC} = Q_{AC-ref} - Q_{AC} \tag{III-14}$$

- **Hysteresis Comparison:** These power errors are fed into hysteresis comparators to generate digitized error signals (HP_s, HQ_{AC}), as shown in Figure III-5:
  - A three-level hysteresis comparator is used for the active power error (eP_s), producing outputs like {-1, 0, +1} corresponding to requests to decrease, maintain, or increase P_s.
  - A two-level hysteresis comparator is often used for the reactive power error (eQ_{AC}), producing outputs like {-1, +1} corresponding to requests to decrease or increase Q_{AC} .

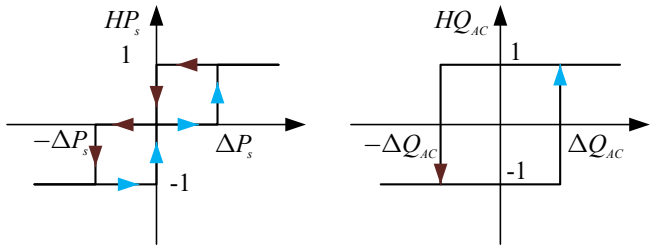

Figure III-5 : RSC Active and reactive powers hysteresis comparators output errors.

- **Rotor Flux Sector Determination:** The estimated rotor flux angle (θ_r) is used to identify which of the typically six predefined angular sectors (each 60° wide) the stator flux vector currently occupies.
- **Switching Table Selection:** The predefined switching table, as shown in Table III-1, constitutes the core decision-making logic. It uses the digitized outputs from the hysteresis controllers (HP_s, HQ_{AC}) and the identified stator flux sector number ($N = 1$ to 6) as inputs. Based on these inputs, the table directly selects one of the eight possible voltage vectors (V_0 to V_7, comprising six active vectors and two zero vectors) that the RSC should apply to the rotor terminals [102].

Table III-1 : RSC DPC switching table.

HQ_{AC}	HP_s	N					
		I	II	III	IV	V	VI
$+1$	$+1$	V_5	V_6	V_1	V_2	V_3	V_4
	0	V_7	V_0	V_7	V_0	V_7	V_0
	-1	V_3	V_4	V_5	V_6	V_1	V_2
-1	$+1$	V_6	V_1	V_2	V_3	V_4	V_5
	0	V_0	V_7	V_0	V_7	V_0	V_7
	-1	V_2	V_3	V_4	V_5	V_6	V_1

- **RSC Switching:** The selected voltage vector determines the switching state (S_a, S_b, S_c) for the RSC power electronic devices IGBTs.

III.4.4. Advantages and Disadvantages

The C-DPC strategy offers significant advantages, including:

- **Fast dynamic response:** Direct power control without intermediate loops allows for quick tracking of power references.
- **Simplicity:** Absence of PI controllers and coordinate transformations for current control simplifies the algorithm.
- **Robustness:** Less sensitive to machine parameter variations compared to some vector control methods.

However, the classical DPC also presents drawbacks:

- **Variable switching frequency:** The use of hysteresis controllers results in a switching frequency that is not fixed, which can complicate the design of filters and potentially cause broader harmonic spectra.
- **Power ripples:** The discrete nature of the voltage vector selection and the hysteresis bands inevitably lead to ripples in the controlled powers.

These limitations, particularly the detrimental effects on power quality, motivate the investigation of the advanced AI-based DPC strategies presented in Chapter IV.

III.5. CLASSICAL CONTROL OF THE GRID SIDE CONVERTER USING C-DPC

The Grid Side Converter (GSC) plays a critical role in the DFIG system by managing the DC link voltage and controlling the reactive power exchanged between the converter and the grid. It ensures a stable DC voltage source for the RSC, regardless of the power flow direction through the rotor circuit, and contributes to the overall reactive power support capability of the wind turbine system. The application of Conventional Direct Power Control (C-DPC) for the GSC is depicted in, as depicted in Figure III-6.

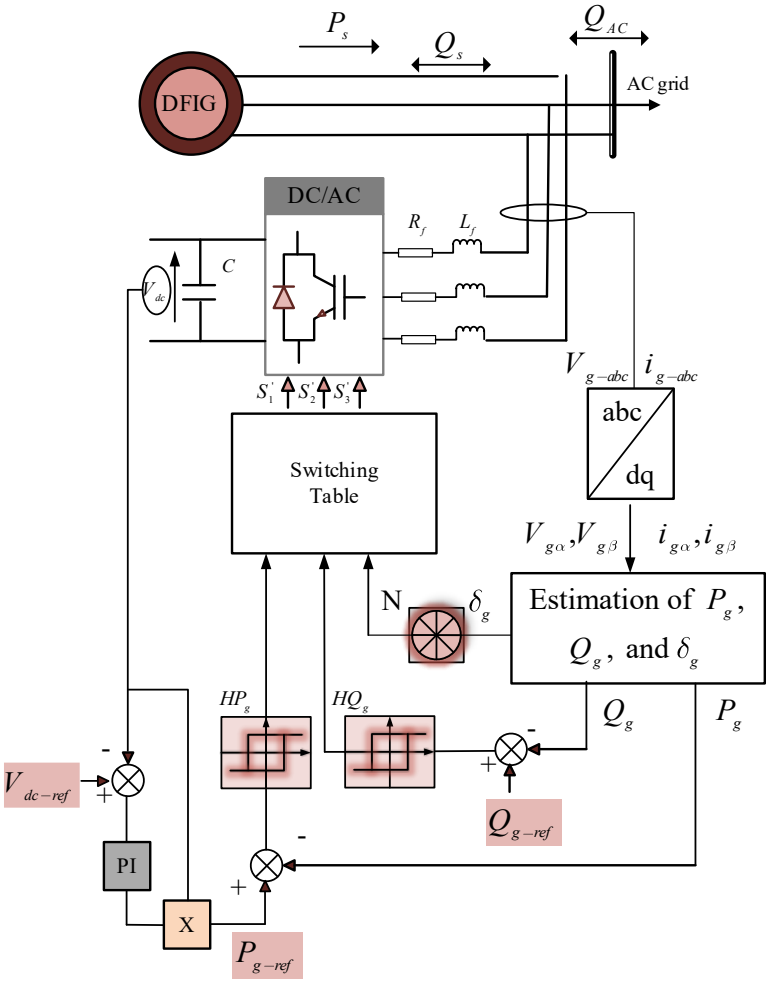

Figure III-6 : Block Diagram of GSC C-DPC Implementation.

III.5.1. Control Objectives and Strategy

- **DC Link Voltage Regulation:** Maintain the DC link voltage (V_{dc}) at its specified reference value (V_{dc-ref}). This is usually achieved using a PI controller that calculates the necessary active power (P_{g-ref}) the GSC must exchange with the grid.
- **Grid Reactive Power Regulation:** Control the reactive power (Q_g) exchanged between the GSC and the grid to track its reference value (Q_{g-ref}). This reference is set to zero for unity power factor operation.

Similar to the RSC control, the C-DPC strategy for the GSC aims to achieve these objectives directly by selecting appropriate GSC voltage vectors based on instantaneous errors, bypassing inner current loops and complex transformations.

III.5.2. Principle of Direct Power Control

The C-DPC strategy for the GSC relies on the instantaneous active (P_g) and reactive (Q_g) power exchanged with the grid. These are defined in the stationary α-β reference frame using the grid voltage ($v_{g\alpha}, v_{g\beta}$) and the current flowing between the GSC and the grid ($i_{g\alpha}, i_{g\beta}$):

$$\begin{aligned} P_g &= v_{g\alpha} i_{g\alpha} + v_{g\beta} i_{g\beta} \\ Q_g &= v_{g\beta} i_{g\alpha} - v_{g\alpha} i_{g\beta} \end{aligned} \quad \text{(III-15)}$$

The GSC connects to the grid typically through an RL filter (L_f and R_f). The voltage generated by the GSC ($\overrightarrow{v_c}$) influences the grid current ($\overrightarrow{i_g}$) based on the grid voltage ($\overrightarrow{v_g}$) and the filter impedance. The relationship is described by Kirchhoff's voltage law [105]:

$$\overrightarrow{V_g} = \overrightarrow{v_c} + R_f \overrightarrow{i_g} + L_f \frac{d\overrightarrow{i_g}}{dt} \quad \text{(III-16)}$$

Neglecting the filter resistance R_f for simplicity over short intervals (ΔT), the change in grid current ($\Delta\overrightarrow{i_g}$) is approximately related to the applied GSC voltage vector $\overrightarrow{v_c}$:

$$\Delta\overrightarrow{i_g} \approx \frac{1}{L_f}\left(\overrightarrow{v_g} - \overrightarrow{v_c}\right)\Delta T \quad \text{(III-17)}$$

This equation highlights that by selecting an appropriate GSC voltage vector ($\overrightarrow{v_c}$) from the available eight discrete vectors (similar to the RSC), the controller directly influences the rate of change of the grid current vector ($\overrightarrow{i_g}$). Consequently, this manipulation directly affects the instantaneous active power P_g and reactive power Q_g exchanged with the grid [60, 105]. The vectors of the output rotor voltage for the GSC are illustrated in Figure III-7.

The crucial link for DC voltage control is the power balance at the DC link capacitor (C_{dc}):

$$C_{dc} \frac{dV_{dc}}{dt} = I_{dc} = \frac{P_{dc}}{V_{dc}} \quad \text{(III-18)}$$

where P_{dc} is the net power flowing into the capacitor. Assuming the converter operates losslessly for control analysis, the power flowing into the DC link

$$-P_g + P_r \approx P_{dc} = C_{dc} V_{dc} \frac{dV_{dc}}{dt} \quad \text{(III-19)}$$

For the purpose of V_{dc} regulation, the GSC's primary role is to control P_g such that it precisely balances the power P_r demanded by the RSC, keeping $dV_{dc}/dt \approx 0$ and thus V_{dc} constant at its reference value. Therefore, controlling P_g provides direct control over the DC link voltage.

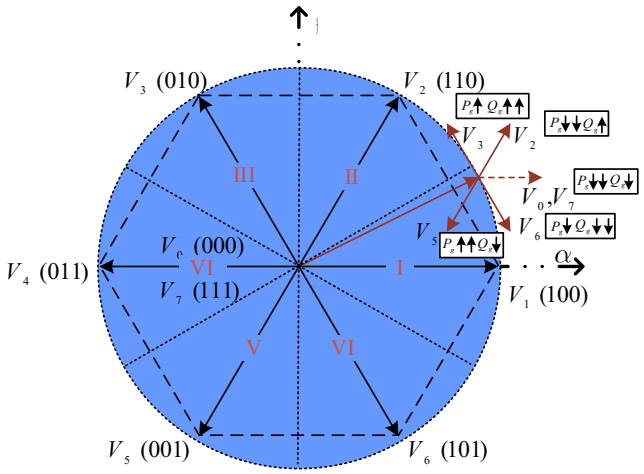

Figure III-7 : Vectors of output rotor voltage for GSC.

III.5.3. Implementation Components

The practical implementation of C-DPC for the GSC involves the following important steps executed in each control cycle:

- **DC Voltage Regulation and P_{g-ref} Generation:** This outer loop generates the active power reference needed by the DPC approach.
  - The DC voltage error is fed into a PI controller:

$$i_{dc-ref} = K_{p-vdc}\left(V_{dc-ref} - V_{dc}\right) + K_{i-vdc}\int\left(V_{dc-ref} - V_{dc}\right)dt \qquad \text{(III-20)}$$

  - Calculate the required active power reference (P_{g-ref}) by multiplying the target DC current by the measured DC voltage:

$$P_{g-ref} = I_{c-ref} \times V_{dc} \qquad \text{(III-21)}$$

  - The reactive power reference (Q_{g-ref}) is typically set to 0 for a unity power factor.
- **Estimation:** Estimate instantaneous grid active (P_g) and reactive (Q_g) powers using Eq. III-15.

  Estimated angle θ_g

$$\theta_g = arctg\left(\frac{v_{g\beta}}{v_{g\alpha}}\right) \qquad \text{(III-22)}$$

- **Power Error Calculation:** The estimated powers are compared to their respective reference values to determine the power errors:

$$eP_g = P_{g-ref} - P_g \; ; \quad eQ_g = Q_{g-ref} - Q_g \tag{III-23}$$

- **Hysteresis Comparison:** These power errors are fed into hysteresis comparators to generate digitized error signals (HP_g, HQ_g), as shown in Figure III-8:

  A two-level hysteresis comparator is often used for both active and reactive powers errors ($\Delta P_g, \Delta Q_g$), producing outputs like {-1, +1} correspondingss to requests to decrease or increase their quantity value.

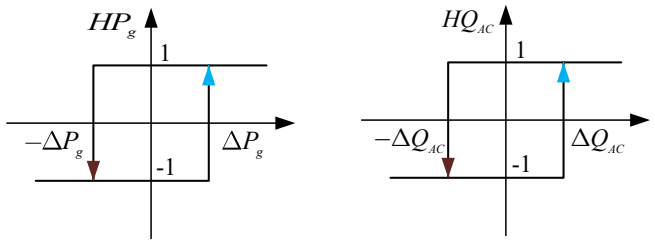

Figure III-8 : GSC Active and reactive powers hysteresis comparators output errors.

- **Flux Sector Determination:** Identify the angular sector ($N_g = 1$ to 6) in which the grid voltage vector $\overrightarrow{v_g}$ currently lies, based on the estimated angle θ_g.
- **Switching Table Selection:** Use the digitized power errors (HP_g, HQ_g) and the grid voltage sector (N_g) as inputs to a predefined switching table. Table III-2 outputs the optimal GSC voltage vector ($\overrightarrow{v_c}$ from $V_0$to V_7) required to drive the powers towards their references [60].
- **GSC Switching:** Apply the selected voltage vector $\overrightarrow{v_c}$ by generating the corresponding switching signals (S'_a, S'_b, S'_c) for the GSC's power switches (IGBTs).

Table III-2 : GSC DPC switching table.

HQ_g	HP_g	N					
		I	*II*	*III*	*IV*	*V*	*VI*
+1	+1	V_3	V_4	V_5	V_6	V_1	V_2
	−1	V_5	V_6	V_1	V_2	V_3	V_4
−1	+1	V_2	V_3	V_4	V_5	V_6	V_1
	−1	V_1	V_2	V_3	V_4	V_5	V_6

III.6. SIMULATION RESULTS AND PERFORMANCE ANALYSIS OF THE CLASSICAL SYSTEM

To comprehensively evaluate the performance and robustness of the classical control system (MPPT, Pitch, RSC C-DPC, GSC C-DPC), dynamic simulations were conducted using

MATLAB/Simulink under a realistic, random variable wind speed profile. This scenario is designed to replicate the fluctuating nature of actual wind resources and test the controller's ability to operate effectively across the full spectrum of DFIG operating modes, including sub-synchronous, synchronous, super-synchronous, and the power-limited overspeed region, in a continuous and successive manner. The system parameters used correspond to the 7.5 kW DFIG system with $\eta_{DFIG} \approx 0.98$ in Appendix. During the simulation, the compensated local reactive power reference (Q_{AC-ref}) was also varied randomly to assess the reactive power control capability under dynamic conditions, while the GSC reactive power reference was kept at $Q_{g-ref} = 0$.

The coordinated response of Maximum Power Point Tracking (MPPT) and Pitch Control systems to dynamic wind is crucial for overall WECS performance. Figure III-9 illustrates this under a variable wind profile. Figure a shows-imposed wind speed (v_{wind}) fluctuations, causing DFIG rotational speed (Ω_{mec}) to traverse various operational modes, including MPPT and power limitation regions. Below rated speed, Ω_{mec} tracks wind variations, indicating active MPPT via Power Signal Feedback (PSF). Speed is clamped near the rated limit during high winds. Figure III-10 confirms pitch control activation, pitch angle (β) remains at 0° during MPPT but increases when speed limits, engaging the PI controller to reduce aerodynamic power. That during MPPT ($\beta = 0°$), tip-speed ratio (λ) and power coefficient (C_p) are maintained at optimal values ($\lambda_{\text{opt}} = 9, C_{p_{\max}} = 0.5$), maximizing efficiency. When pitch control activates ($\beta > 0°$), both λ and C_p are reduced, confirming effective power limitation. These results demonstrate cooperative functioning of the MPPT and Pitch Control systems across the full operational envelope.

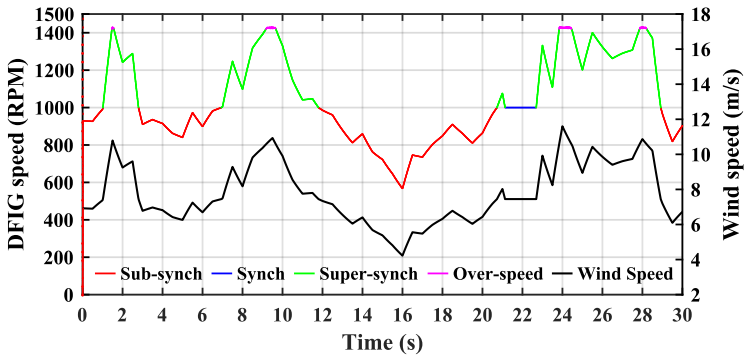

Figure III-9: Wind and DFIG speed .

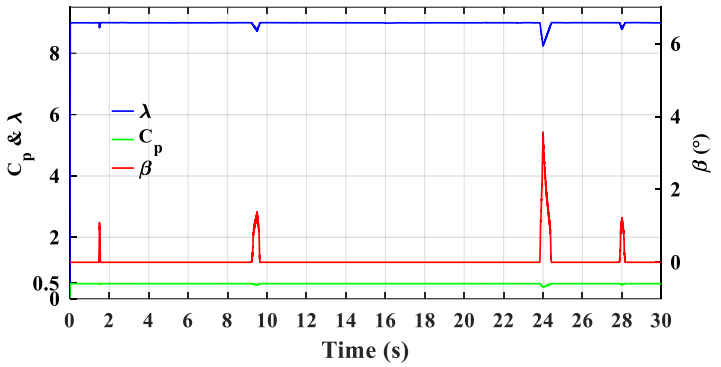

Figure III-10 : C_p, λ and β .

Figuers III-11 and III-12 display the performance of the RSC C-DPC controller in tracking the dynamically varying active power reference (P_{s-ref}) and the randomly varying compensated local reactive power reference (Q_{AC-ref}) under the variable wind profile. Demonstrates that the RSC C-DPC controller successfully forces the average values of P_s and Q_{AC} to follow their respective references across the wide range of operating conditions imposed by the variable wind and reactive power profile. The system correctly operates in generator mode (P_s negative) and manages reactive power compensation, including absorption ($Q_{AC} > 0$), generation ($Q_{AC} < 0$), and unity power factor ($Q_{AC} = 0$). The dynamic response appears capable of following the changing references. However, inherent to the C-DPC method, significant ripples are clearly visible in both the P_s and Q_{AC} waveforms throughout the entire simulation, regardless of the operating mode or power level.

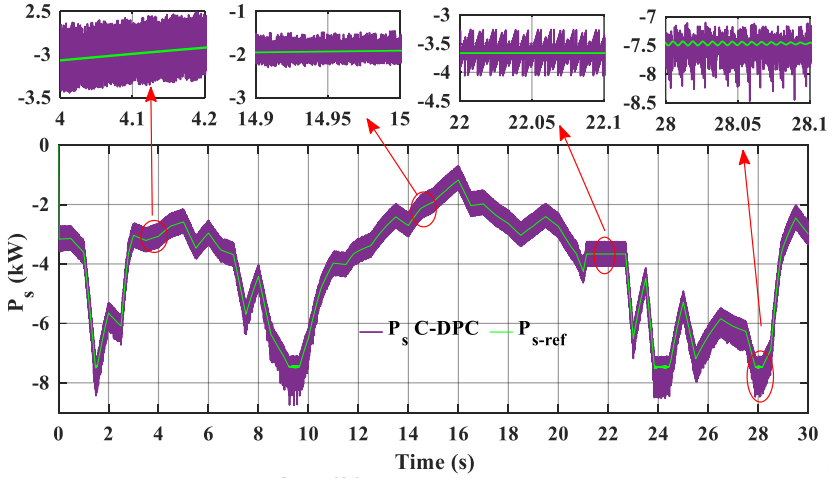

Figure III-11 :Generated active power .

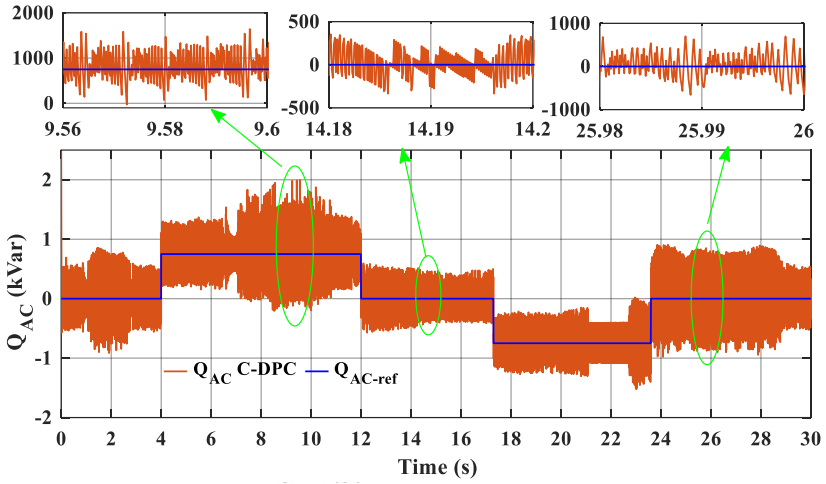

Figure III-12 : Local reactive power.

The performance of the GSC under C-DPC control during the variable wind simulation is shown in below Figuers. The primary objectives are to maintain DC link stability and ensure unity power factor operation for the GSC. Figure III-13 shows the GSC's outer PI voltage loop successfully maintains the average DC link voltage its 880V reference, confirming stability despite large power fluctuations from RSC actions. Figure III-14 displays the active power (P_g) transferred to the grid, demonstrating the GSC's ability to dynamically inject variable active power corresponding to wind conditions while maintaining DC link voltage. Figure III-15 confirms the GSC reactive power (Q_g) is regulated around zero for unity power factor. However, C-DPC's nature introduces noticeable ripples on P_g and Q_g, as highlighted.

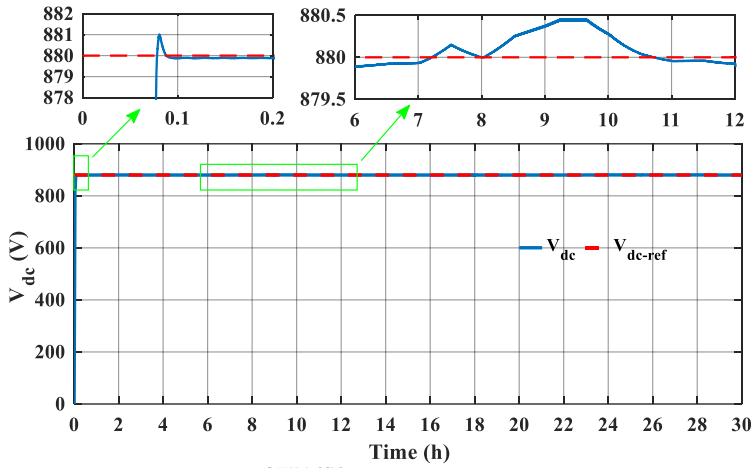

Figure III-13 : DC link voltage.

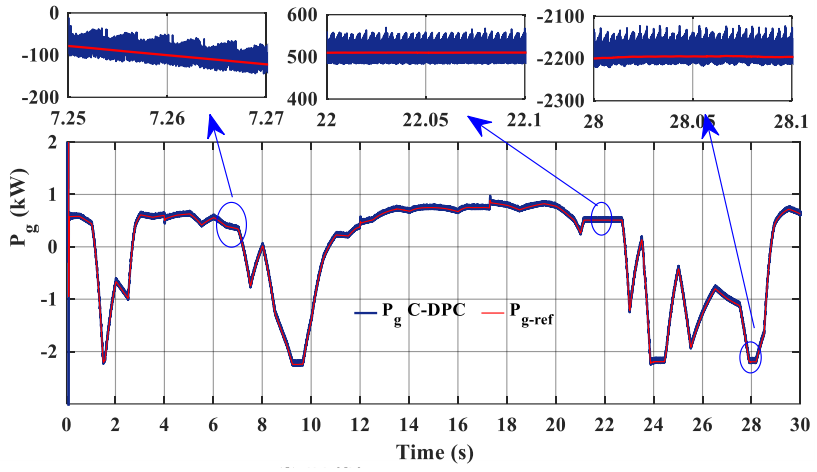

Figure III-14 : Grid active power.

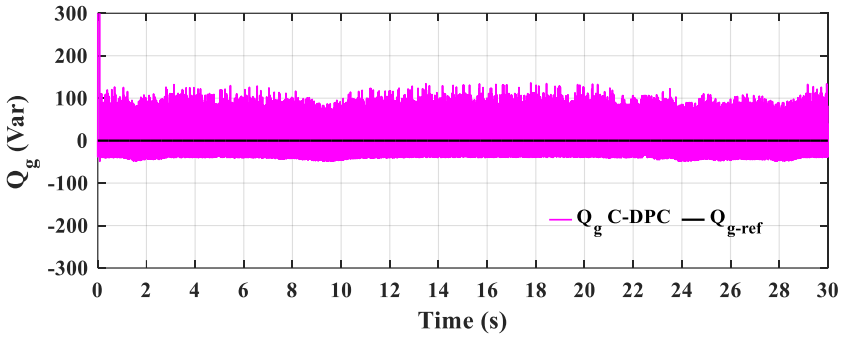

Figure III-15 : Grid reactive power.

AC current quality is critical for WECS control, as poor-quality leads to increased losses, electromagnetic interference, and grid code non-compliance. This analysis examines stator, rotor, and grid current quality generated under classical C-DPC for both RSC and GSC.

Stator current waveforms in Figure III-16, directly injected into the grid, are paramount for quality. However, they show significant non-sinusoidal distortion across all operating conditions (synchronous, sub, super, overspeed). This consistently poor quality indicates inadequate internal power generation under C-DPC.

The RSC's C-DPC synthesizes the rotor current in Figure III-17, whose amplitude and frequency vary with generator speed and mechanical slip. Rotor current waveforms distinctly exhibit distortion and high-frequency switching ripple, typical of variable-frequency hysteresis converters.

The grid current, exchanged with the AC grid via the GSC and its RL filter in Figure III-18, is crucial for compliance. Its quality is influenced by both RSC and GSC C-DPC operations. The grid current waveforms show distortion reflecting the variable switching frequencies and ripple.

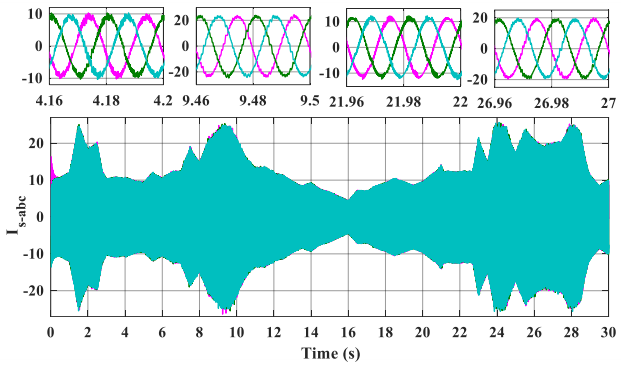

Figure III-16 : Stator current waveforms.

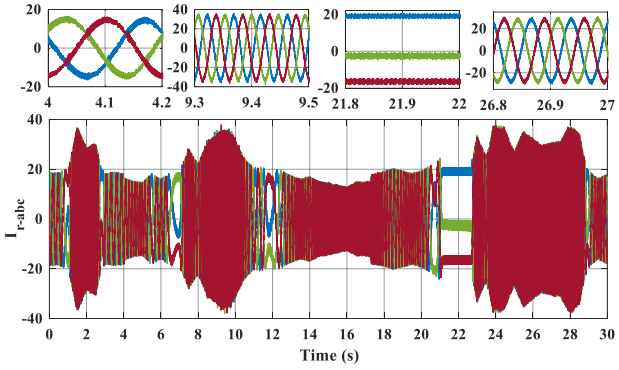

Figure III-17: Rotor current waveforms.

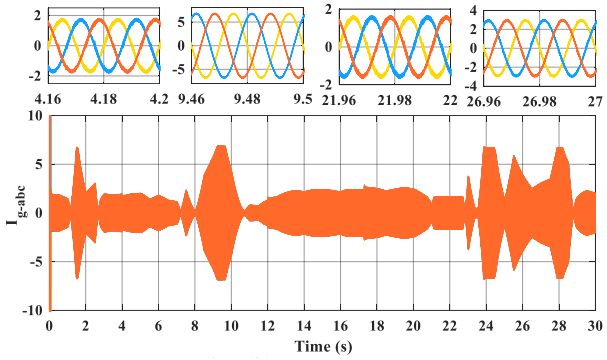

Figure III-18 : Grid current exchanged with the AC grid via the GSC waveforms.

III.7. CRITICAL ANALYSIS OF THE CLASSICAL CONTROL SYSTEM

The performance analysis conducted in Section III.6 allows for a critical evaluation, focusing on the aspects motivating the developments in Chapter IV.

- **RSC C-DPC Deficiencies (Primary Issue):** The classical C-DPC strategy for the RSC is identified as the main source of poor power quality. The inherent use of hysteresis comparators and a fixed switching table leads directly to:
  - **Excessive Power Ripple:** Undesirable fluctuations in P_s sand Q_{AC}, causing torque pulsations and inefficient power delivery.
  - **High Stator Current Harmonics:** Significant current distortion in i_s, which directly pollutes the grid connection.
- **GSC Classical Control:** The classical GSC controller successfully maintained DC link voltage stability, which is crucial for system operation. Its limitations are acknowledged but are not the primary target for improvement in the next chapter.
- **MPPT/Pitch Control**: The classical PSF MPPT and PI Pitch controllers performed adequately in managing the aerodynamic interface according to standard practices.

The analysis strongly indicates that improving the RSC control strategy is the most critical step towards enhancing the overall power quality and grid compatibility of the WT-DFIG system, starting from the source of power conversion within the generator itself.

III.8. CONCLUSION

This chapter has presented and evaluated a classical control methodology for the WT-DFIG system, utilizing established techniques: PSF MPPT, PI Pitch Control, C-DPC for the RSC, and a classical approach for the GSC. Simulation results under realistic variable wind conditions demonstrated the system's fundamental operational capabilities.

However, the critical performance analysis identified significant drawbacks, primarily originating from the Conventional Direct Power Control (C-DPC) applied to the Rotor Side Converter (RSC). These limitations include substantial ripples in controlled powers (P_s, Q_{AC}) and high distortion in stator currents (i_s), These factors negatively impact the quality of power injected into the grid and reduce system efficiency.

The identified deficiencies of the conventional RSC C-DPC provide the direct motivation for Chapter IV. The next chapter will introduce and investigate novel RSC control strategies based on Artificial Intelligence techniques (specifically Fuzzy Logic and Neural Networks). These advanced strategies aim to overcome these limitations and improve the WT-DFIG's performance and grid compatibility.

IV

AI-ENHANCED DIRECT POWER CONTROL OF WT-DFIG ROTOR SIDE CONVERTER

IV.1. INTRODUCTION

Chapter III provided a comprehensive analysis of classical control strategies for the WT-DFIG system, culminating in a critical evaluation of Conventional Direct Power Control (C-DPC). The findings identified the C-DPC applied to the Rotor Side Converter (RSC) as the primary source of significant performance limitations. Specifically, the inherent reliance on fixed hysteresis comparators and a predefined switching table, while offering simplicity and fast dynamics, inevitably results in substantial ripples in the controlled active (P_s) and reactive (Q_{AC}) powers, high harmonic distortion (THD) in the stator currents directly injected into the grid, and an undesirable variable switching frequency [66]. These deficiencies negatively impact power quality, reduce overall system efficiency, and pose challenges for seamless grid integration.

The identified shortcomings of the classical RSC C-DPC provide the direct motivation for exploring more advanced control paradigms. Artificial Intelligence (AI) techniques, notably Fuzzy Logic Control (FLC) and Artificial Neural Networks (ANNs), have demonstrated significant potential in addressing the complexities, non-linearities, and uncertainties prevalent in power electronic converter control and renewable energy systems. Their capacity for learning, adaptation, and approximating complex functions offers a promising pathway to overcome the limitations of conventional hysteresis-based switching logic [106, 107].

Recognizing this potential, considerable research has aimed to enhance DPC for DFIGs through advanced control strategies distinct from direct AI replacements. Techniques integrating Space Vector Modulation (DPC-SVM) sought to achieve a constant switching frequency, simplifying filter design and reducing ripples [108-112], but often compromised inherent DPC robustness by reintroducing parameter-sensitive PI controllers requiring careful tuning. Model Predictive Control (MPC) variants offered potentially superior performance by explicitly optimizing

switching decisions based on system models and cost function minimization at each step [113-118]. Yet, this optimization typically demands accurate system knowledge and imposes a significant computational burden. Furthermore, nonlinear approaches like Adaptive Control [104], robust Sliding Mode Control (SMC-DPC) [119-125], and systematic Backstepping Control (BC-DPC) [126, 127] demonstrated improved dynamic response and disturbance rejection. Despite these performance gains, such advanced methods frequently introduced substantial design and implementation complexity, often undermining the original appeal of DPC's simplicity and intuitive operation.

The recent emergence of AI-driven control strategies reflects a growing need for techniques capable of handling sophisticated control schemes with enhanced precision and versatility. Techniques utilizing fuzzy logic [128-136] and neural networks [106, 107, 137-144] have been implemented to improve Direct Power Control (DPC) through various means, such as replacing traditional switching mechanisms, optimizing controller settings, and refining advanced DPC variants like SVM-DPC and sliding mode control. However, many of these explorations have been constrained in their breadth, frequently examining only a limited selection (e.g., two out of four) of the DFIG's operating modes or neglecting a holistic evaluation of system performance in realistic operational contexts. Moreover, the modifications introduced by certain intelligent control techniques have raised questions about whether they compromise the fundamental simplicity that makes DPC advantageous.

Despite these advances, a critical review as reported in [64-67] shows that many studies fail to provide comprehensive validation under realistic operating scenarios. In particular, rigorous testing over the full DFIG operating spectrum (sub-synchronous, synchronous, super-synchronous, and overspeed) combined with all reactive power compensation modes (absorption, generation, unit PF), all subjected to continuous random wind speed variations, is often lacking. In addition, several proposed intelligent solutions significantly increase controller complexity.

This chapter aims to address these gaps by introducing, detailing, and evaluating four novel AI-based DPC strategies specifically designed for the WT-DFIG's RSC control. These strategies were developed during the course of this doctoral research, and the key findings have been published in [65, 66]. The proposed methods evaluated here are as follows:

- ✓ **Fuzzy-Hysteresis DPC (FH-DPC):** Using FLC to replace hysteresis logic [65].
- ✓ **Neural-Hysteresis DPC (NH-DPC):** Using an ANN to replace hysteresis logic [65].
- ✓ **Prediction Neural Network DPC (PNN-DPC):** Using an ANN for direct voltage vector index prediction [66].

- ✓ **Classification Neural Network DPC (CNN-DPC):** Using an ANN for direct voltage vector classification.

The primary objective is to significantly improve the power quality (reduce ripples and THD) originating from the RSC, while striving to maintain computational feasibility and robustness. These strategies will be rigorously evaluated against C-DPC and relevant prior intelligent methods using comprehensive simulations under realistic, dynamic conditions.

The chapter proceeds as follows: Section IV.2 discusses FLC fundamentals. Section IV.3 covers ANN fundamentals. Sections IV.4 and IV.5 detail the design and implementation of the proposed AI-DPC strategies (grouped by approach: hysteresis replacement and direct selection). Section IV.6 presents the comprehensive simulation results and comparative performance analysis. Finally, Section IV.7 summarizes the chapter's findings and contributions.

IV.2. FUNDAMENTALS OF FUZZY LOGIC

Fuzzy logic (FL) is a mathematical methodology for dealing with uncertainty and imprecision. It was developed by Lotfi Zadeh in the 1960s [145]. FL allows variables to have degrees of membership in sets, rather than strictly belonging or not belonging. This capability to model vague concepts using linguistic terms (like fast, slow, high, low) makes fuzzy logic control (FLC) particularly adept at controlling complex, nonlinear systems where precise mathematical models are unavailable or impractical, or where human expertise is the primary control knowledge [146].

IV.2.1. Fuzzy Sets and Membership Functions

The foundation of FL lies in the concept of a fuzzy set. Unlike a classical (crisp) set where an element either belongs or does not, a fuzzy set A defined over a universe of discourse U (the range of possible values for a variable, e.g., the range of possible power error values) is characterized by a membership function (MF), $\mu_{A(x)}$. This function assigns each element x in U a degree of membership in the set A, represented by a value in the interval $[0, 1]$. $\mu_{A(x)} = 1$ signifies full membership, $\mu_{A(x)} = 0$ signifies no membership, and intermediate values indicate partial membership.

IV.2.1.1. Linguistic Variables

Variables whose values are not numbers but words or sentences from a natural or artificial language (e.g., Error, Temperature). The values of a linguistic variable are fuzzy sets representing concepts (e.g., for Error, the values might be Negative Large, Zero, Positive Small).

IV.2.1.2. Membership Functions:

Define the shape and boundaries of fuzzy sets. Common types include:

- **Triangular:** Defined by three points (a, b, c), $\mu(x) = \max\left(0, \min\left(\frac{x-a}{b-a}, \frac{c-x}{c-b}\right)\right)$.
- **Trapezoidal:** Defined by four points (a, b, c, d). $\mu(x) = \max\left(0, \min\left(\frac{x-a}{b-a}, 1, \frac{d-x}{d-c}\right)\right)$.
- **Singleton:** A crisp value represented as a fuzzy set with membership 1 at a single point x_0 and 0 elsewhere. $\mu(x) = \begin{cases} 1 & \text{if } x = x_0 \\ 0 & \text{if } x \neq x_0 \end{cases}$.

IV.2.2. FLC Architecture and Operation

A Fuzzy Logic typically consists of four main components that process information from inputs to generate a control output [147], as represented in Figure IV-1:

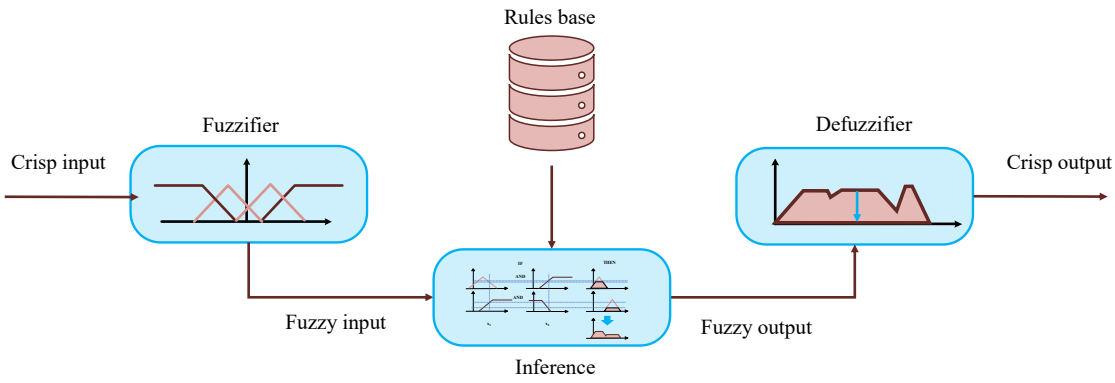

Figure IV-1 : FL Architecture Block Diagram.

IV.2.2.1. Fuzzification Interface:

Converts the crisp (numerical) sensor inputs (e.g., measured errors e_{PS}, $e_{Q_{AC}}$) into fuzzy degrees of membership for each relevant linguistic term (fuzzy set) using predefined MFs.

IV.2.2.2. Knowledge Base

Contains the essential control knowledge, comprising:

- **Data Base:** Defines the MFs for all input and output linguistic variables.
- **Rule Base:** A collection of linguistic IF-THEN rules that describe the control strategy. The rules have the general form:

  `Rule j: IF` x_1 `is` A_{j1} `AND` x_2 `is` A_{j2} `... AND` x_n `is` A_{jn} `THEN` y `is` B_j

  where x_i are input variables, y is the output variable, and A_{ji}, B_j are fuzzy sets.

IV.2.2.3. Inference Engine (Decision-Making Logic)

This unit simulates human decision-making by applying the fuzzy rules to the fuzzified inputs. For each rule j:

- The degree of fulfillment α_j of its premise (IF part) is calculated. This involves applying fuzzy logical operators. Consistent with standard Mamdani implementations and the approach used in this work the AND operator connecting conditions in the premise (e.g., `IF` eP_s `is` P `AND` eQ_{AC} Z) is implemented using the minimum operator:

$$\alpha_j = \min\left(\mu_{A_{j1}}(x_1), \mu_{A_{j2}}(x_2), \dots, \mu_{A_{jn}}(x_n)\right) \tag{IV-1}$$

- The degree of fulfillment α_j is then used to determine the fuzzy output contributed by that rule. In the Mamdani inference method, the output MF B_j is typically scaled or clipped by α_j, resulting in $\mu_{C_j}(y)$.
- The fuzzy outputs from all rules that have fired ($\alpha_j > 0$) are combined (aggregated) into a single fuzzy set representing the overall controller output $\mu_{C_{\text{agg}}}(y)$. The aggregation process, combining the outputs resulting from different rules, typically uses the maximum operator:

$$\mu_{C_{\text{agg}}}(y) = \max_j\left(\mu_{C_j}(y)\right) \tag{IV-2}$$

IV.2.2.4. Defuzzification Interface

Converts the aggregated fuzzy output set $\mu_{C_{\text{agg}}}(y)$ back into a single crisp numerical value y_{crisp} that can be used as the actual control signal. Several methods exist:

- **Centroid / Center of Area (CoA):** Calculates the center of gravity of the area under $\mu_{C_{agg}}(y)$. Robust but can be computationally intensive.

$$y_{crisp} = \frac{\int y \cdot \mu_{C_{agg}}(y) dy}{\int \mu_{C_{agg}}(y) dy} \quad \text{(IV-3)}$$

- **Bisector:** Finds the value y_{crisp} that partitions the area under $\mu_{C_{agg}}(y)$ into two equal halves:

$$\int_{-\infty}^{y_{crisp}} \mu_{C_{agg}}(y) dy = \int_{y_{crisp}}^{\infty} \mu_{C_{agg}}(y) dy \quad \text{(IV-4)}$$

- **Mean of Maximum (MoM), Smallest of Maximum (SoM), Largest of Maximum (LoM):** Based on the output values where the membership degree is maximal. Computationally simpler, but may not reflect the entire shape of the fuzzy output.

IV.2.3. Fuzzy Logic Suitability for DPC Enhancement

Fuzzy Logic (FL) is a suitable candidate for the improvement of DPC for a number of reasons, which can be attributed to its fundamental characteristics. It functions without the necessity of an exact process model or system parameters, demonstrates robustness against noise and disturbances such as variable wind speeds, and maintains a relatively simple structure based on linguistic rules, facilitating implementation.

IV.3. FUNDAMENTALS OF ARTIFICIAL NEURAL NETWORKS

Artificial Neural Networks (ANNs) are powerful computational intelligence tools inspired by the parallel processing capabilities of the human brain. They consist of numerous simple processing elements (neurons) organized in interconnected layers. ANNs learn from data by adjusting the strengths (weights) of these connections, enabling them to model complex, nonlinear relationships between inputs and outputs without requiring explicit mathematical derivations. This makes them highly suitable for tasks like pattern recognition, classification, prediction, and control in diverse fields, including the challenging domain of power system control [148].

A typical ANN consists of an input layer, one or more hidden layers, and an output layer. Neurons in one layer are connected to neurons in the subsequent layer, with each connection having an associated weight. This layered structure, as depicted generically in Figure IV-2, allows the network to perform non-linear mappings from inputs to outputs.

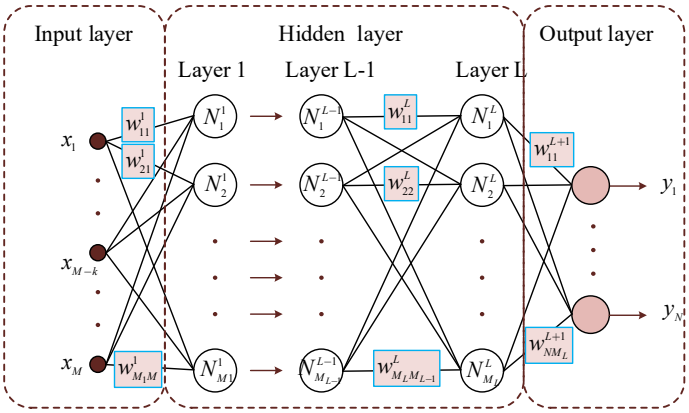

Figure IV-2: General architecture of a multi-input and multi-output neural network.

The application of ANNs to Direct Power Control (DPC) offers potential advantages over conventional methods, particularly in adapting to dynamic conditions like fluctuating wind speeds in Wind Turbine Doubly-Fed Induction Generator (WT-DFIG) systems. While conventional DPC often relies on predefined switching tables, ANNs can learn optimal control actions (like selecting the appropriate voltage vector) based on real-time system states (e.g., power errors, flux position) potentially offering faster and more adaptive responses [66].

Designing an ANN for such control tasks involves several key steps: data preparation, network architecture selection, and training using appropriate algorithms [149-151].

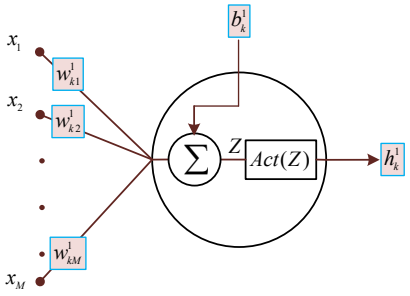

Figure IV-3 Operating principle of a neuron.

IV.3.1. Data Preparation and Input Scaling

Effective ANN training requires a suitable dataset. For DPC applications, the input features typically include variables like the active power error (ePs), reactive power error (eQ_{AC}), and the rotor flux sector (N). The desired output (target) is often the index of the optimal voltage vector (V_n) to be applied.

Before feeding data into the network, pre-processing is essential. A common and often crucial step is input scaling. Feature values are scaled to a specific range, such as [-1, 1], to prevent

features with larger numerical values from dominating the learning process and to potentially improve the convergence speed and stability of the training algorithm.

IV.3.2. Neuron Model and Feed forward

In order to produce the output of the neural network. The input features are fed into the network, and the data is only moved forward through the hidden layers and finally to the output layer.

Therefore, the output value of each neuron h_k^l in the first hidden layer is calculated by summing the multiplication of a vector input feature $\boldsymbol{x} = [x_1, x_2, x_3 \dots, x_M]^T$ with its own vector weight $\boldsymbol{w}^1 = [w_{k1}^1, w_{k2}^1, \dots, w_{kM}^1]$ plus the bias value b_k^1 of a neuron. Then, the activation function is applied to it, as depicted in Figure IV-3. It can be mathematically described as follows:

$$\begin{cases} Z = \boldsymbol{w}^1 \boldsymbol{x} + b_k^1 \\ h_k^1 = Act(Z) \end{cases}; \quad k = 1 \dots M_1 \tag{IV-5}$$

Where superscript of ($\boldsymbol{w}, b$ and h) means first hidden layer.

Moreover, the outputs from all neurons in the first hidden layer serve as inputs to the second hidden layer. This process continues with each subsequent hidden layer until reaching the output layer. The calculation of each neuron's output value is performed in the same manner as in the first hidden layer and can be represented mathematically as follows:

$$h_k^{l+1} = Act\left(w^{l+1}\boldsymbol{H}^l + b_k^{l+1}\right); \quad l = 1 \dots L \tag{IV-6}$$

Where $\boldsymbol{H}^l = \left[h_1^l, h_2^l, \dots, h_{M_l}^l\right]$ is vector output previous layer.

The output of the neural network is given as follows:

$$y_k = h_k^{L+1}; \qquad k = 1 \dots N \tag{IV-7}$$

IV.3.3. Activation Functions

Activation functions introduce non-linearity, enabling ANNs to model complex relationships. Common choices include:

- **The praline function:** Used often in output layers for regression tasks.

$$Act(Z) = Z \tag{IV-8}$$

- **The sigmoid function:** Squashes output to the range (0, 1). Historically used in hidden layers.

$$Act(Z) = \frac{1}{1+e^{-Z}} \tag{IV-9}$$

- **The softmax function:** Used in the output layer for multi-class classification problems. It converts neuron outputs ($\boldsymbol{z}$) into a probability distribution over N classes.

$$Act(\boldsymbol{z})_i = \frac{e^{Z_i}}{\sum_{j=1}^{N} e^{Z_j}} \tag{IV-10}$$

IV.3.4. Backpropagation

The training process is to adjust the weights and bias values to get the neural network output to match the actual output.

The feed-forward neural network is trained by supervised learning. This means reducing the error between the actual and expected output of the network ($e_k = y_k - d_k$). It is done by reducing the cost function. Therefore, there are several formulas for the cost function:

Mean Squared Error (MSE):

$$MSE = \frac{1}{N}\sum_{i=1}^{N}(y_i - d_i)^2 \tag{IV-11}$$

Where $N$is the number of outputs.

Cross-entropy (CE):

$$CE = -\sum_{i=1}^{C_{ann}} d_i \, log(\, y_i) \tag{IV-12}$$

Where C_{ann} is the number of classes.

The backpropagation algorithm is a process in which the gradient of the cost function is calculated from the output layer, passing through the hidden layers to the input layer. Then the weights and bias values of the neural network are updated based on this process. The algorithms used in this literature are Levenberg Marquardt and Scaled Conjugate.

IV.3.5. ANN Suitability for DPC Enhancement

ANNs are a suitable candidate for the improvement of DPC due to their characteristics. They work without an explicit process model, learning the control mapping directly from data examples of system behavior or control principles. They are also resilient to noise and disturbances if the training data is sufficiently varied. Although the internal structure and training can be complex, the implemented trained network provides a direct input-output mapping, making it structurally straightforward for application within the control loop.

IV.4. AI-ENHANCED DPC STRATEGY 1: HYSTERESIS COMPARATORS REPLACEMENT

The first category of AI-based enhancement explored in this thesis focuses on improving the C-DPC scheme by directly addressing the limitations imposed by its conventional hysteresis comparators. These comparators, while simple, introduce quantization effects and operate with fixed bands, leading to power ripple and variable switching frequency. The strategies presented in this section, FH-DPC and NH-DPC, replace these binary/ternary comparators with more sophisticated AI modules (FLC and ANN, respectively) that generate a nuanced control signal representing the desired power adjustments. This signal is then fed into the standard DPC switching table, thus retaining the core vector selection logic of C-DPC but refining the error processing stage. This approach, detailed in [65], aims for improved power quality through smoother control action.

IV.4.1. Fuzzy Hysteresis DPC (FH-DPC)

The FH-DPC controller, as developed and presented in [65], employs a single Mamdani-type Fuzzy Logic Controller to replace the traditional pair of hysteresis comparators. The overall system configuration, illustrating how the FH-DPC module integrates into the WT-DFIG control structure by replacing the conventional hysteresis block while retaining the estimation block and switching table, is depicted in Figure IV-4.

IV.4.1.1. Controller Design

The FLC is designed with two crisp inputs: the active power error eP_s and the local reactive power error eQ_{AC}. The FLC produces a single crisp output, E_{powers}, which encodes the combined desired state of power adjustment. The conceptual structure is shown in Figure IV-5.

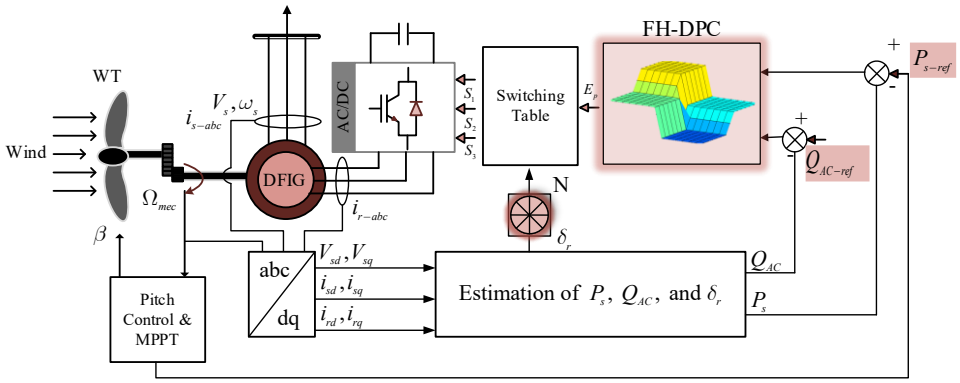

Figure IV-4: WT-DFIG system controlled with FH-DPC.

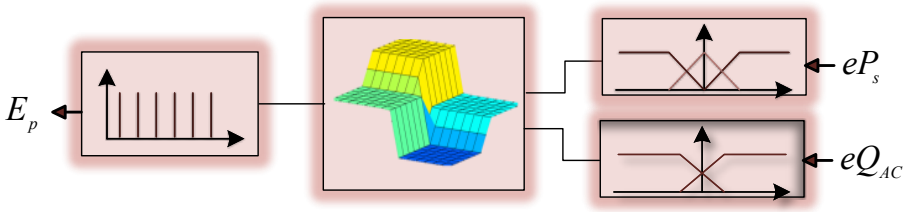

Figure IV-5: Scheme of FH-DPC.

IV.4.1.2. FLC Implementation Details

- **Fuzzification:** The input eP_s is fuzzified using three MFs: Negative (N), Zero (Z), and Positive (P), as shown in Figure IV-6. The input eQ_{AC} uses two MFs: Negative (N) and Positive (P), as shown in Figure IV-7. These MFs define the degree to which the input errors belong to each linguistic category.

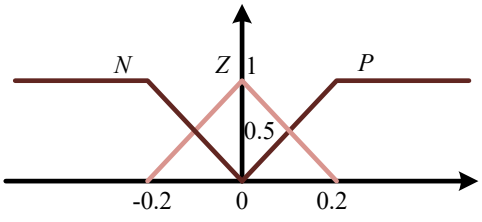

Figure IV-6 : MFs of generated active power error.

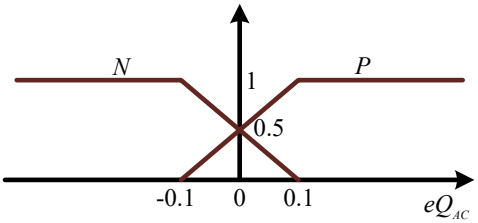

Figure IV-7 : MFs of compensated local reactive power error.

- **Rule Base:** The core control logic is embedded in a set of six IF-THEN rules, as presented in Table IV-1. These rules directly map the linguistic combinations of input errors to desired output states (E_1 to E_6), reflecting the intended actions of the C-DPC hysteresis logic. An example rule is: `IF` eP_s `is` P `AND` eQ_{AC} P `THEN` E_{powers} `is` E_1 . The Mamdani inference system with the min operator for AND was employed.

Table IV-1:Fuzzy Rule of FH-DPC.

eQAC/ePS	*P*	*Z*	*N*
P	*E1*	*E2*	*E3*
N	*E4*	*E5*	*E6*

- **Defuzzification:** The aggregated fuzzy output, representing the combined conclusion from all active rules, is defuzzified using the Bisector method. The output variable E_{powers} is represented by six singleton MFs, each corresponding to a specific combined error state (E_1 to E_6) , as presented in Figure IV-8. The Bisector method finds the crisp value that divides the area of the aggregated output fuzzy set equally.

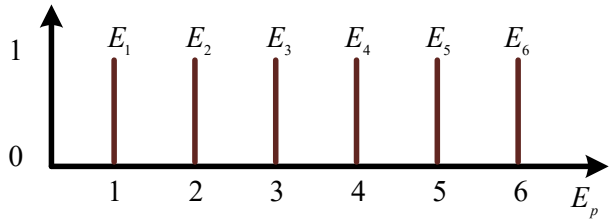

Figure IV-8 : MFs of digital error powers.

IV.4.1.3. Integration with Switching Table

Integration with Switching Table: The defuzzified crisp output E_{powers} from the FLC module, along with the calculated rotor flux sector number (N), serves as the input to the modified DPC switching table, as presented in Table IV-2. This table then directly outputs the index (V_n, 0 to $ss7$) of the voltage vector to be applied by the RSC.

Table IV-2 : Switching table of FH/NH-DPC for RSC.

E_{powers}	N					
	I	II	III	IV	V	VI
E_1	V_5	V_6	V_1	V_2	V_3	V_4
E_2	V_7	V_0	V_7	V_0	V_7	V_0
E_3	V_3	V_4	V_5	V_6	V_1	V_2
E_4	V_6	V_1	V_2	V_3	V_4	V_5
E_5	V_0	V_7	V_0	V_7	V_0	V_7
E_6	V_2	V_3	V_4	V_5	V_6	V_1

IV.4.2. Neural Hysteresis DPC (NH-DPC)

Complementary to the fuzzy approach, the NH-DPC controller, also detailed in [65], utilizes an Artificial Neural Network to learn and replicate the desired input-output mapping of the enhanced hysteresis logic.

IV.4.2.1. Controller Design

The ANN module takes the same normalized power errors (eP_s, eQ_{AC}) as inputs and generates the same combined digital error state output (E_{powers}) as the FH-DPC. It learns the non-linear function represented by the fuzzy system or derived from the C-DPC hysteresis principles. The overall control structure incorporating the NH-DPC module is shown in Figure IV-9.

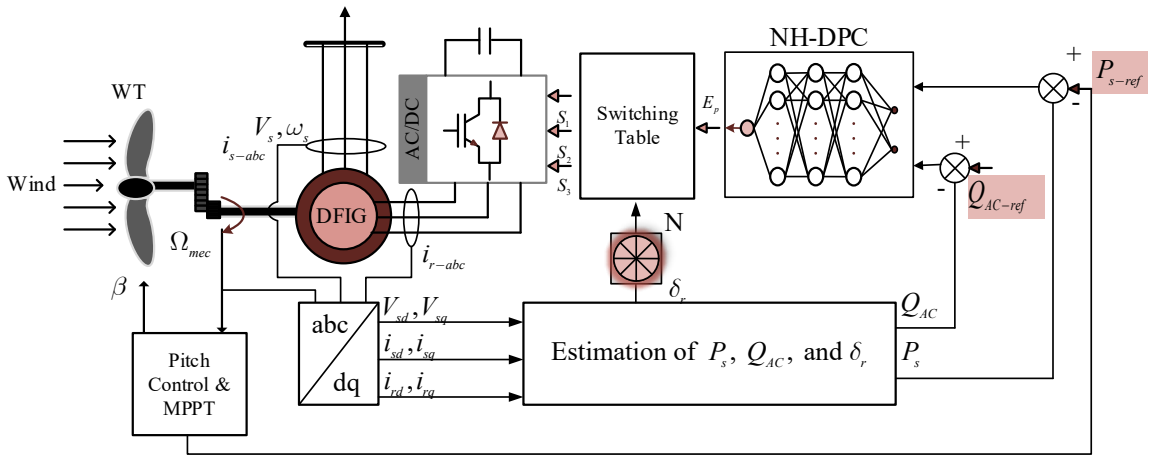

Figure IV-9 : WT-DFIG system controlled with NH-DPC.

IV.4.2.2. ANN Architecture and Training

- **Architecture:** Through experimentation, an MLP architecture was selected as optimal, as illustrated in Figure IV-10. It comprises an input layer (2 neurons for eP_s, eQ_{AC}), three hidden layers with 3, 7, and 5 neurons respectively using Sigmoid activation function, and a single output neuron (for E_{powers}) with a Praline activation function.
- **Training Data:** A dataset of 14,400 input-output pairs ($\{eP_s, eQ_{AC}\} \rightarrow E_{powers}$) was generated, representing the desired mapping, sampling shown in Table IV-3. This data was partitioned into training (70%), validation (15%), and testing (15%) sets.
- **Training Process:** Supervised learning was performed using the Levenberg-Marquardt backpropagation algorithm in the MATLAB Neural Network Toolbox. The algorithm minimized the Mean Squared Error (MSE) cost function. Training converged rapidly,

achieving an extremely low validation MSE of 4.17e-13 in 430 epochs, indicating successful learning of the target function, as demonstrated in Figure IV-11.

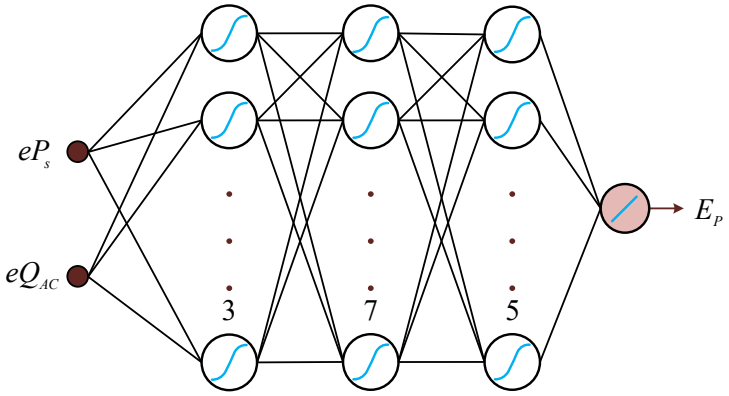

Figure IV-10 : Architecture of hysteresis neural network.

Table IV-3 : Neural network's training samples.

N of samples	eP_s	eQ_{AC}	E_{powers}
1	+0.92	+0.2	1
2	+0.05	-0.18	4
3	-0.82	-0.4	6
4	-0.24	+0.98	3

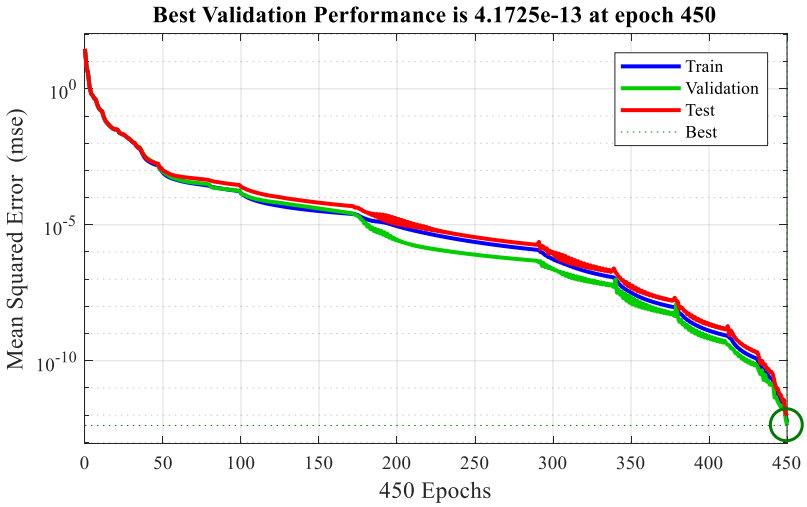

Figure IV-11 : Performance of trained NH.

IV.4.2.3. Integration with Switching Table

Similar to FH-DPC, the crisp Epowers value predicted by the trained ANN, along with the rotor flux sector N, is fed into the same modified switching table, which is presented in Table IV-2, to determine the RSC voltage vector V_n.

IV.5. AI-ENHANCED DPC STRATEGY 2: DIRECT VOLTAGE VECTOR SELECTION

This second strategy represents a more advanced application of AI, aiming to replace the entire core decision-making logic of C-DPC (hysteresis comparators and switching table) with a single, trained ANN. The ANN directly learns the complex mapping from the instantaneous system state (power errors and flux position) to the optimal voltage vector selection, potentially offering further simplification of the control structure and improved performance by capturing nuances missed by the rule-based or table-driven approaches.

IV.5.1. Prediction Neural Network DPC (PNN-DPC)

The PNN-DPC controller, developed and analyzed in [66], employs an ANN configured as a function approximator or regressor to predict the numerical index (0-7) of the most suitable voltage vector.

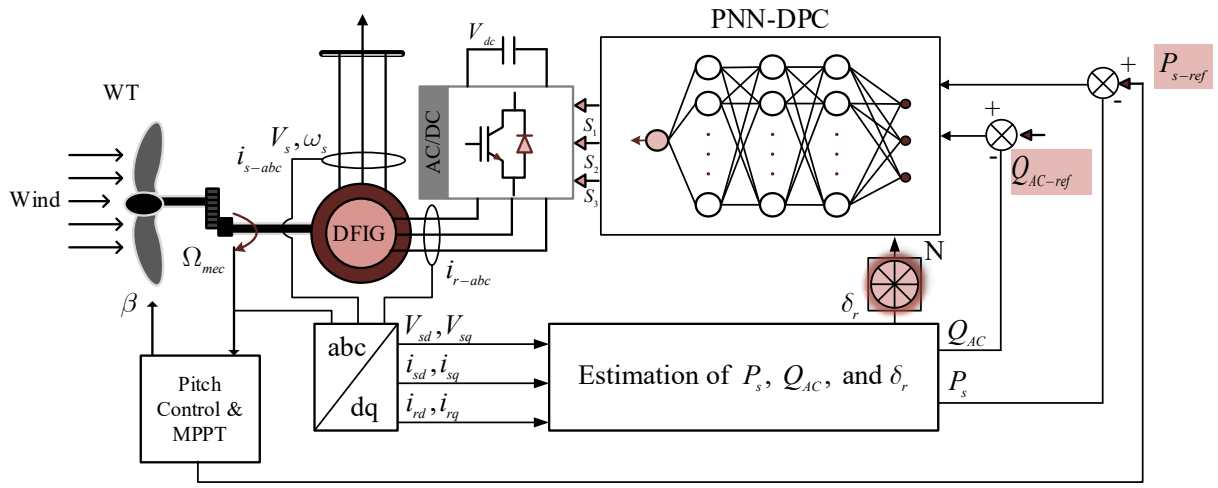

Figure IV-12 : WT-DFIG system controlled with PNN-DPC.

IV.5.1.1. Controller Design

The PNN takes three inputs: active power error (eP_s), local reactive power error (eQ_{AC}), and the rotor flux sector number (N, encoded numerically 1-8). It generates a single continuous output value, V_n, intended to approximate the optimal voltage vector index. The system structure is shown in Figure IV-12.

IV.5.1.2. ANN Architecture and Training

- **Architecture:** An MLP network was designed, as presented in Figure IV-13,consisting of an input layer (3 neurons), three hidden layers (12, 7, and 6 neurons respectively, using Sigmoid activation), and a single output neuron with a Praline activation function.

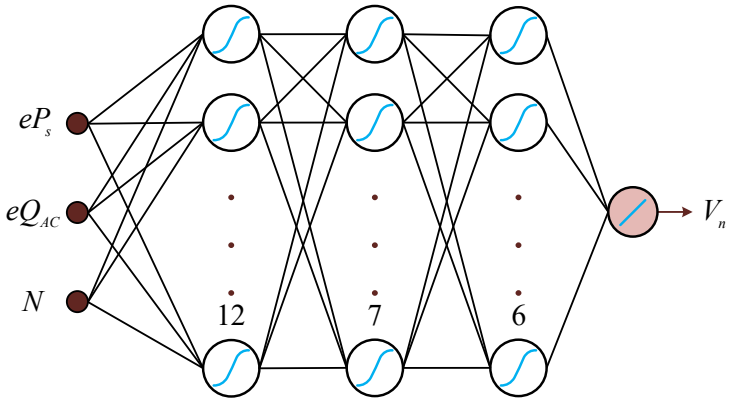

Figure IV-13 : Architecture of prediction neural network.

- **Training Data:** A large dataset (75,600 samples, examples in Table IV-4) was created based on the input conditions (eP_s, eQ_{AC}, N) and the corresponding optimal voltage vector index (V_n) determined by the C-DPC logic (switching table). Data was split 70/15/15 for training/validation/testing.

Table IV-4: Neural network's training samples.

N of samples	eP_s	eQ_{AC}	Vn
1	+0.92	+0.2	1
2	+0.05	-0.18	4
3	-0.82	-0.4	6
4	-0.24	+0.98	3

- **Training Process:** The network was trained using the Levenberg-Marquardt algorithm to minimize the MSE cost function between the predicted V_n and the target V_n. The training achieved a low validation MSE of 2.4e-4 after 743 iterations, signifying good approximation of the target function, as demonstrated in Figure IV-14.

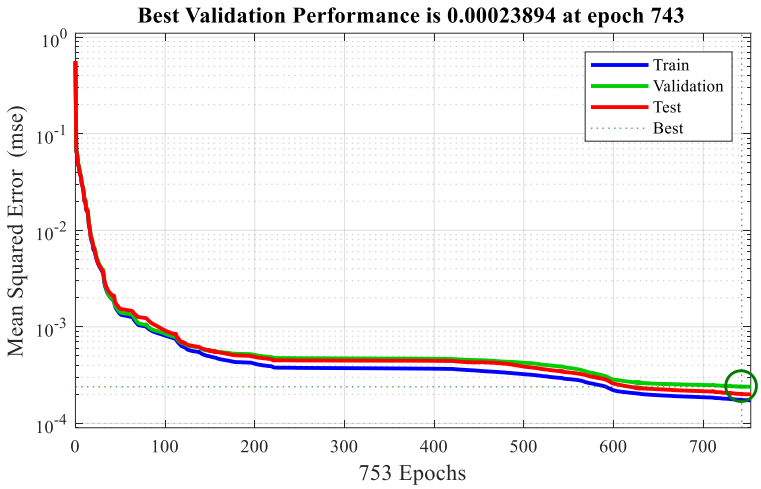

Figure IV-14 : Performance of trained PNN.

IV.5.1.3. Vector Application

The continuous output V_n from the trained PNN is rounded to the nearest integer (in the range 0-7) to select the actual discrete voltage vector V_n applied to the RSC inverter switches. This direct selection bypasses the need for any switching table lookup in the real-time control loop.

IV.5.2. Classification Neural Network DPC (CNN-DPC)

The CNN-DPC controller, also presented in [66], approaches the vector selection task as a multi-class classification problem. The ANN classifies the current operating state into one of eight possible categories, each corresponding to an optimal voltage vector.

IV.5.2.1. Controller Design

The CNN receives the same three inputs (eP_s, eQ_{AC}, N) as the PNN. However, its output layer consists of 8 neurons, where the activation of the k-th neuron represents the probability or confidence that voltage vector V_k (where $k = 0$ to 7) is the optimal choice for the given input state. The overall system diagram is depicted in Figure IV-15.

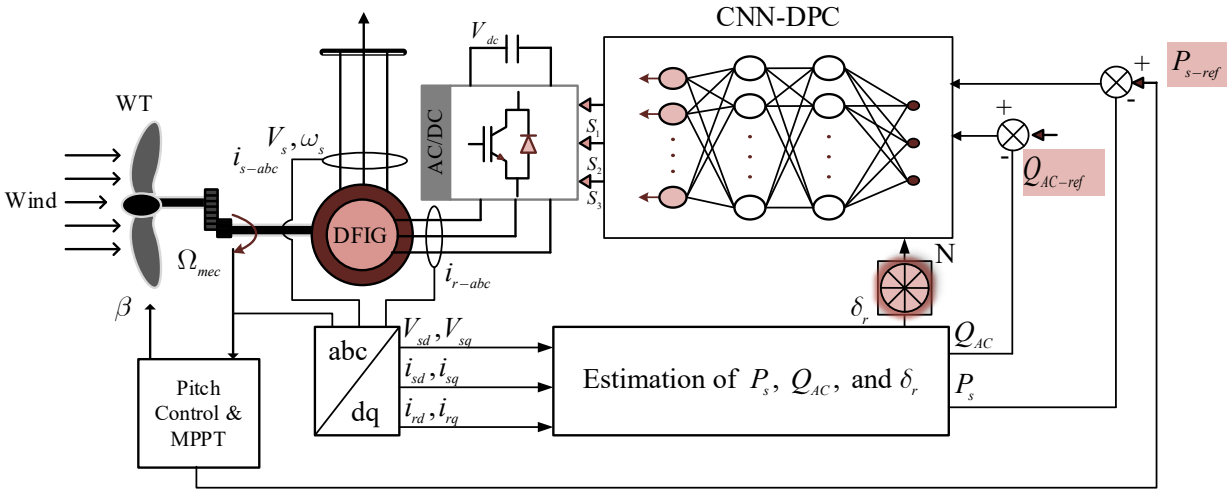

Figure IV-15 : WT-DFIG system controlled with CNN-DPC.

IV.5.2.2. ANN Architecture and Training

- **Architecture:** An MLP structure was employed, as displayed in Figure IV-16, featuring an input layer (3 neurons), two hidden layers (24 and 12 neurons) with Sigmoid activation, and an output layer (8 neurons) using the Softmax activation function. The Softmax function is crucial here, as it transforms the raw outputs of the last layer into a probability distribution (outputs are positive and sum to 1).

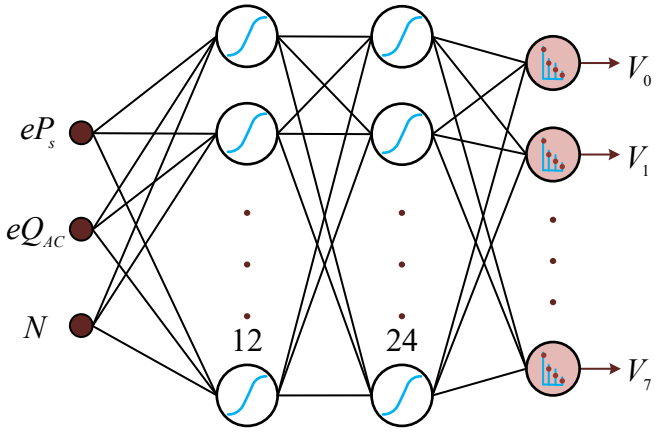

Figure IV-16 : Architecture of classification neural network.

- **Training Data:** A dataset of 72,000 samples was used, as presented in Table IV-4 , similar to PNN-DPC, but the target output (d) was structured as a one-hot encoded vector (e.g., [0 0 0 0 0 1 0 0] if V_5 is the target vector).
- **Training Process:** The network was trained using the Scaled Conjugate Gradient (SCG) algorithm, suitable for classification tasks, minimizing the Cross-Entropy (CE) cost function, which is standard for measuring the difference between probability distributions. The

training achieved a very high classification accuracy of 99.9% after only 594 iterations, indicating excellent learning of the classification task, as confirmed in Figure IV-17 and Table IV-5.

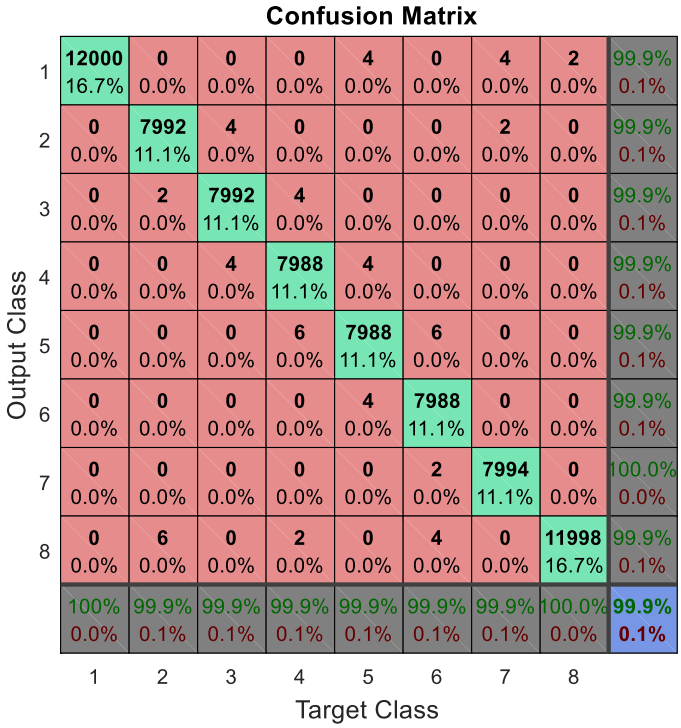

Figure IV-17 : Confusion matrix of the overall data based on trained CNN.

Table IV-5 : Summary of the CNN-DPC training results.

Samples	Iterations	Accuracy	Performance	Time
72000	594	99.9%	0.0006	48s

IV.5.2.3. Vector Application

In real-time operation, the voltage vector V_k corresponding to the output neuron k with the highest activation (highest probability output from Softmax) is selected and applied to the RSC. This also bypasses the need for a switching table.

IV.6. COMPREHENSIVE PERFORMANCE EVALUATION AND COMPARATIVE ANALYSIS

This section presents a detailed evaluation of the four proposed AI-DPC strategies (FH-DPC, NH-DPC, PNN-DPC, CNN-DPC) based on the simulation results reported in [65, 66]. The performance is compared against the baseline C-DPC, where done in Chapter III.

IV.6.1. Simulation Setup

All simulations were conducted in the MATLAB/Simulink environment using the 7.5 kW WT-DFIG system model described in Chapter II, with parameters listed in Appendix. The classical PSF MPPT and PI Pitch Control algorithms managed the turbine speed and power limitation, while the GSC maintained the DC link voltage (880 V) and unity power factor using C-DPC. The comparison focused solely on the impact of the different RSC control strategies under identical system conditions.

IV.6.2. Scenario 1: Step Wind Profile Analysis (Reference Tracking)

This controlled scenario evaluates reference tracking and steady-state performance using a step-like wind profile. Figure IV-18 depict this input wind speed and the corresponding DFIG mechanical speed response. This clearly shows the transitions designed to force the system through sub-synchronous (0-3s), synchronous (3-5s, 8-9s), and super-synchronous (5-8s) operating modes. Simultaneously, the Q_{AC} reference was stepped to test absorption, generation, and unity power factor operation.

The generated active power response for the controllers is presented in Figure IV-19. These plots confirm that the average value of the generated active power P_s under FH-DPC, NH-DPC, PNN-DPC, and CNN-DPC closely follow the reference $P_{s-\text{ref}}$, similar to C-DPC. The zoomed-in sections within these figures specifically highlight the dynamic response during transitions. They illustrate that all AI methods maintain a rapid and well-damped response, comparable to C-DPC, ensuring fast tracking without introducing oscillations. Similarly, Figure IV-20 show the compensated local reactive power Q_{AC} tracking its stepped reference. Again, the average tracking is accurate for all methods, and the zoomed sections confirm excellent dynamic performance during changes in the Q_{AC} reference.

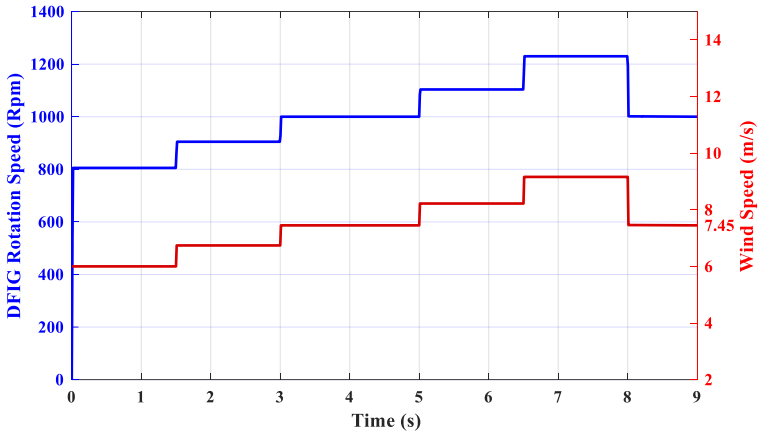

Figure IV-18 : Wind profile and DFIG speed.

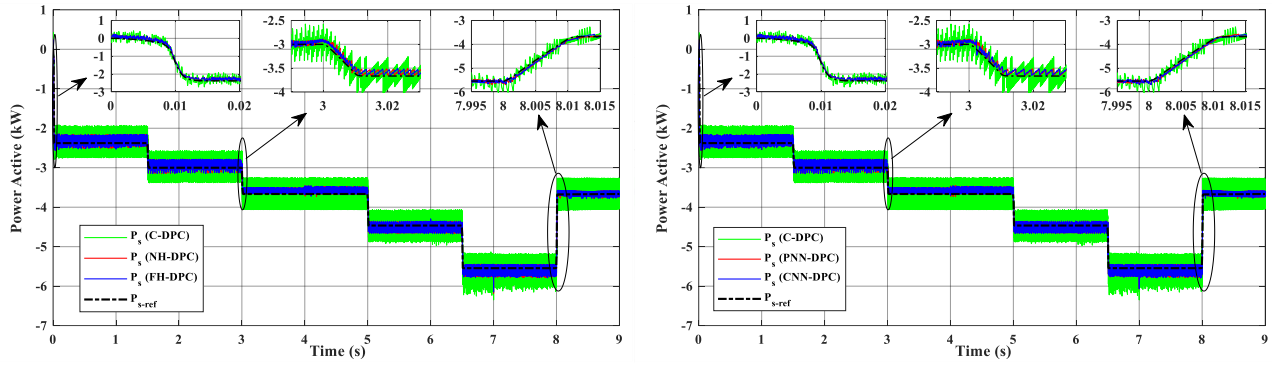

(a) *(b)*

Figure IV-19 : Generated active power with its reference, (a) using FH/NH-DPC, (b) using PNN/CNN-DPC.

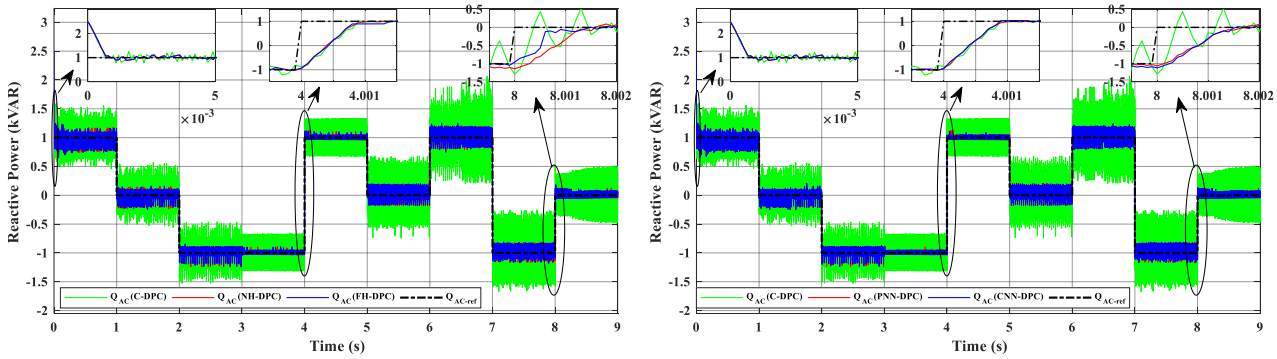

(a) *(b)*

Figure IV-20 : Compensated local reactive power with its reference, (a) using FH/NH-DPC, (b) using PNN/CNN-DPC.

The significant advantage of the AI strategies is visualized in the detailed steady-state views. Figure IV-21 provides close-up views of the active power waveform during sub-synchronous, synchronous, and super-synchronous modes, respectively. These figures clearly contrast the large fluctuations inherent in C-DPC with the substantially smoother P_s waveforms achieved using FH-DPC, NH-DPC, PNN-DPC, and CNN-DPC. Likewise, Figuers IV-22 and IV-23 provide similar detailed views for the compensated local reactive power across different modes and compensation

levels (absorption, generation, unity PF). They consistently show the dramatic reduction in Q_{AC} ripple achieved by all four AI methods compared to the C-DPC model.

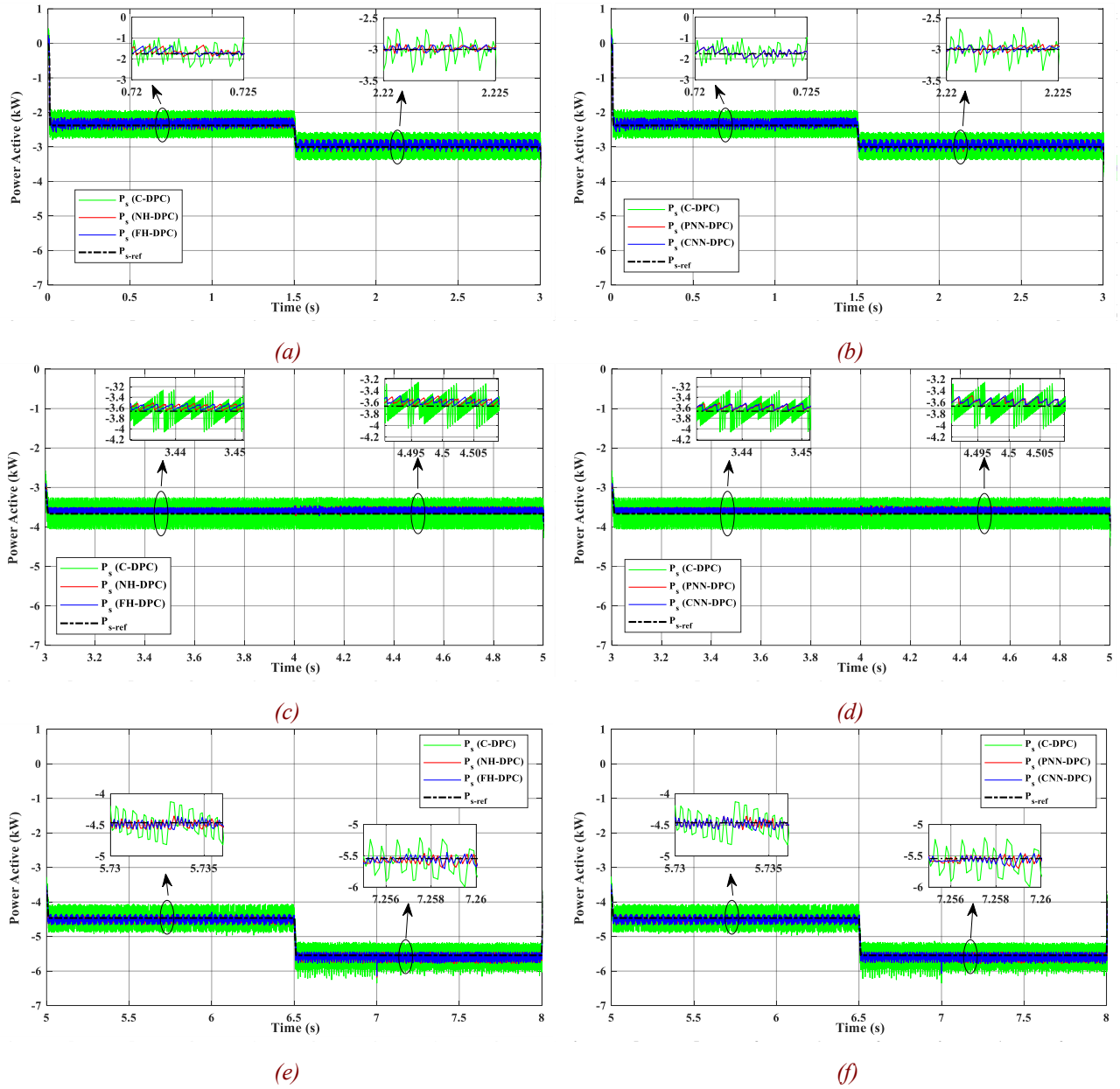

Figure IV-21 : Comparison of generated active power using FH/NH and PNN/CNN references across operating modes, (a) Super-synchronous (FH/NH-DPC), (b) Sub-synchronous (PNN/CNN-DPC), (c) Synchronous (FH/NH-DPC), (d) Synchronous (PNN/CNN-DPC), (e) Sub-synchronous (FH/NH-DPC), (f) Super-synchronous (PNN/CNN).

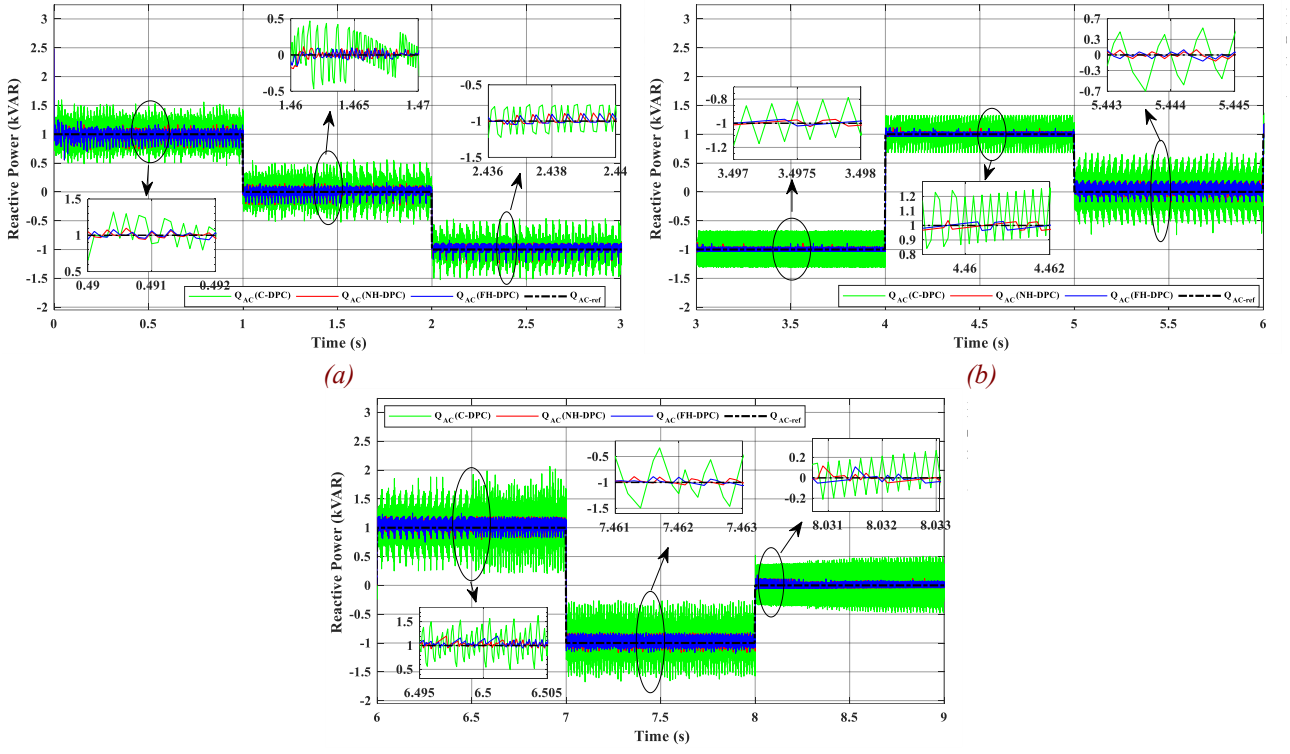

(a) (b)

(c)

Figure IV-22: Compensated local reactive power over operating modes using FH/NH-DPC, (a) In sub-synchronous mode (b) In synchronous mode, Q_{AC} is consumed and generated, while in super-synchronous mode, Q_{AC} is null. (c) In super-synchronous mode, Q_{AC} is generated and consumed, while in synchronous mode, Q_{AC} is null.

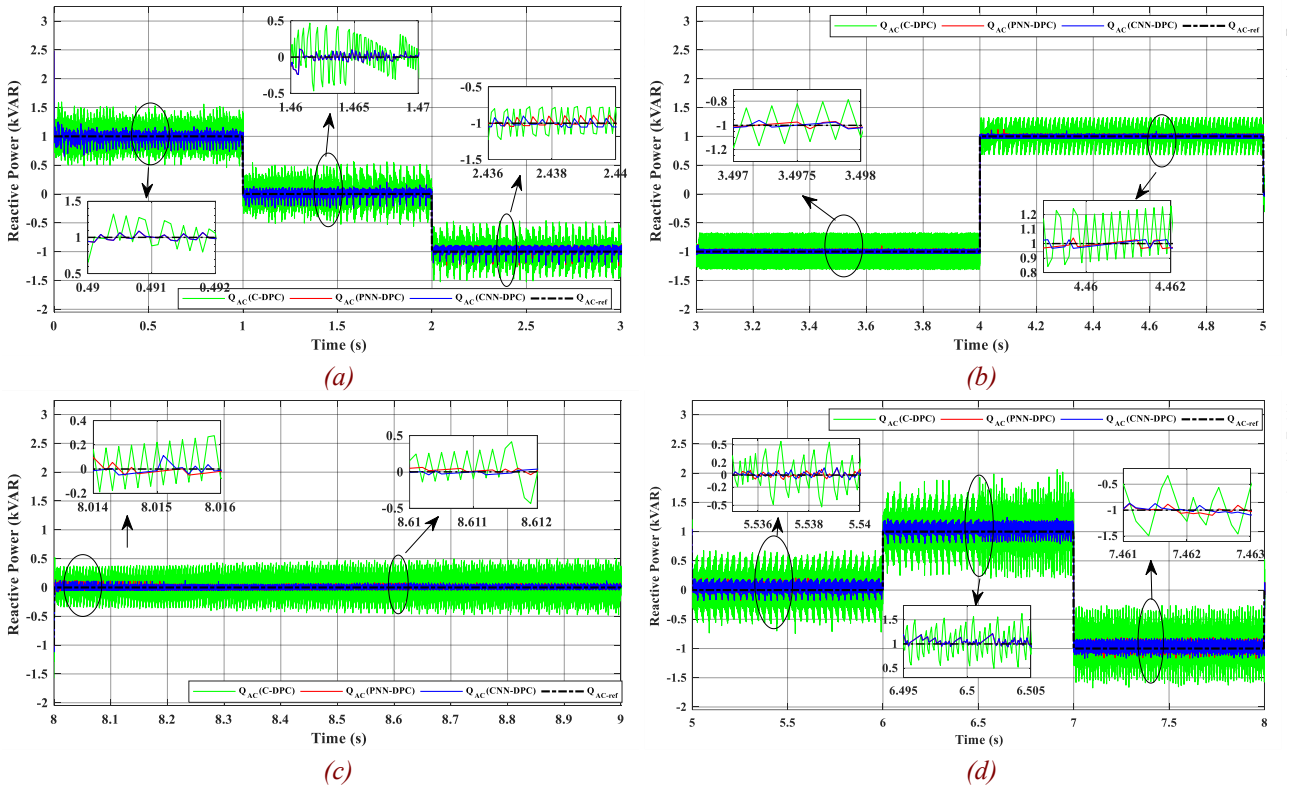

(a) (b)

(c) (d)

Figure IV-23 : Compensated local reactive power over operating modes using PNN/CNN-DPC, (a) In sub-synchronous mode (b) In synchronous mode, Q_{AC} is consumed and generated. (c) In synchronous mode, Q_{AC} is consumed and generated, Q_{AC} is null. (d) In super-synchronous mode.

The visual improvements are quantified in the summary tables. Table IV-6 present the standard deviation of the active power ripple (P_s ripples) for each controller in each mode. This table numerically confirms the significant reduction, showing percentages ranging from 71.26% to 80.50% improvement for the AI methods over C-DPC. The table also allowed comparison between the AI methods, confirming FH-DPC slightly outperforms NH-DPC and CNN/PNN are closely matched. Similarly, Table IV-7 quantify the reactive power ripple (Q_{AC} ripples). The data shows reductions of 67.64% to 88.46% for the AI controllers versus C-DPC, confirming the effectiveness across all operating conditions.

Table IV-6 :Comparison of different control methods for active power ripples.

Performances		Operation modes		
		Sub-Synchronous	Super–Synchronous	Synchronous
Generated power ripples (W)	C-DPC	203.06	202.85	193.98
	NH-DPC	58.35	54.96	37.9
	FH-DPC	58.05	55.56	37.82
	PNN-DPC	57.39	55.99	37.99
	CNN-DPC	57.52	55.99	37.94
Ripples reduction ratio	NH-DPC compared to C-DPC	71.26%	72.91 %	80.46%
	FH-DPC compared to C-DPC	71.41%	72.61%	80.5%
	PNN-DPC compared to C-DPC	71.74%	72.40%	80.41%
	CNN-DPC compared to C-DPC	71.67%	72.40%	80.44%

Table IV-7 :Comparison of different control methods for local reactive power compensation ripples.

Performances		Operation and compensation modes								
		Absorption			Generation			Unit power factor		
Operation modes		Sub-Synch	Super–Synch	Synch	Sub-Synch	Super–Synch	Synch	Sub-Synch	Super–Synch	Synch
Compensated local reactive power ripples (Var)	C-DPC	187.4	269.37	173.32	183.21	240.52	169.47	189.67	232.3	228.03
	NH-DPC	60.65	74.87	20.65	51.59	56.19	19.67	52.96	69.61	30.63
	FH-DPC	60.39	74.86	20.69	51.39	55.68	19.71	51.31	69.1	31.02
	PNN-DPC	60.51	75.1	20.56	51.62	57.51	19.58	52.2	69.06	30.71
	CNN-DPC	60.56	75.1	20.4	51.1	57.25	19.55	52.2	68.96	30.58
Ripples reduction ratio compared to C-DPC	NH-DPC	67.64%	72.21%	88.09%	71.84%	76.64%	88.39%	72.08%	70.03%	86.57%
	FH-DPC	67.77%	72.21%	88.06%	71.95%	76.85%	88.37%	72.95%	70.25%	86.40%
	PNN-DPC	67.71%	72.12%	88.14%	71.82%	76.09%	88.45%	72.48%	70.27%	86.53%
	CNN-DPC	67.68%	72.12%	88.23%	72.11%	76.20%	88.46%	72.48%	70.31%	86.59%

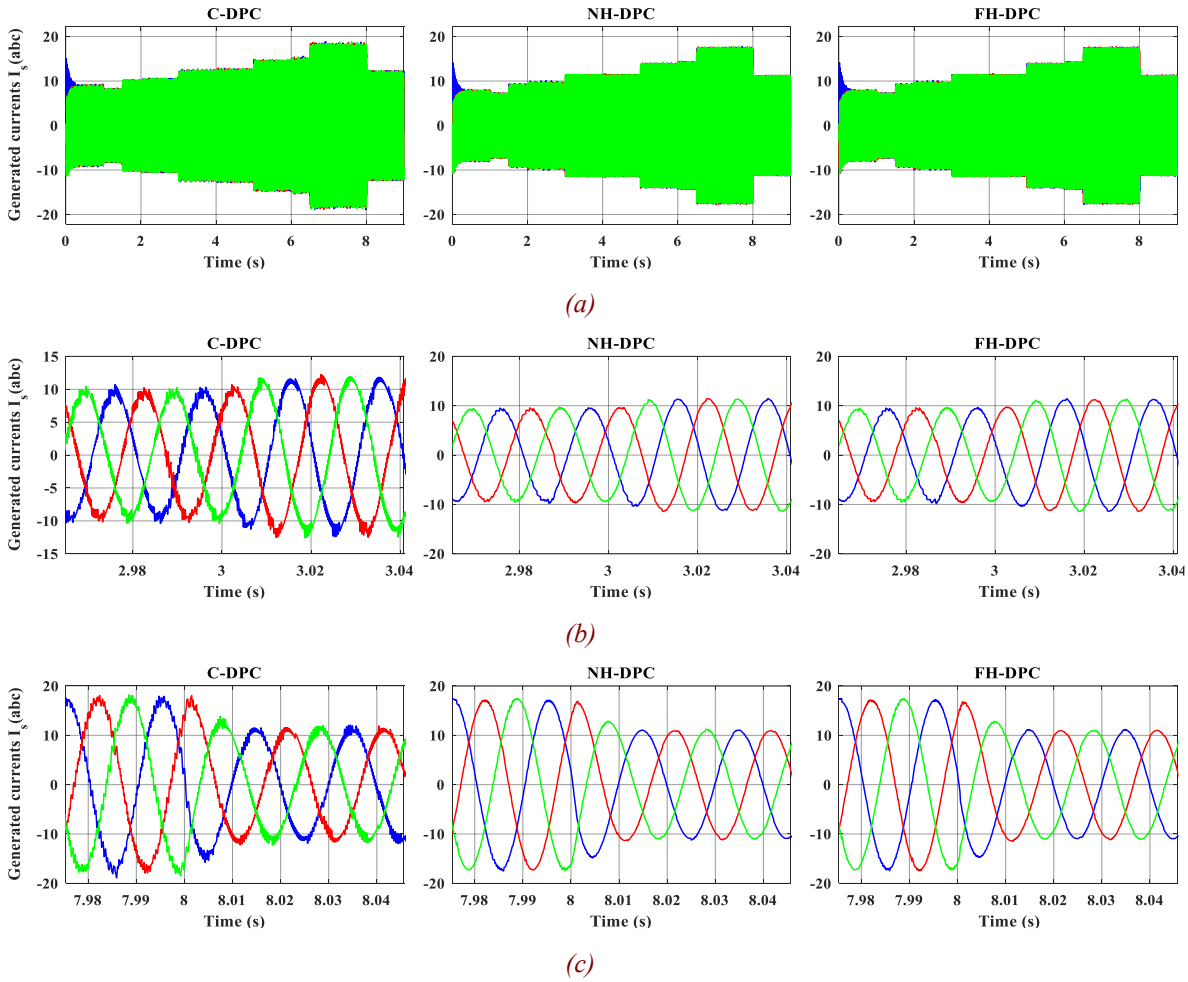

Figure IV-24 : Waveforms of currents generated by the WT-DFIG, using the proposed techniques: The C-DPC, NH-DPC, and FH-DPC, (a) generated currents (b) from sub- to synchronous mode. (c) . from super- to synchronous mode.

Table IV-8 : Comparison of different control techniques for the current generated THD.

	Performances	Operation modes		
		Sub-Synchronous	Super–Synchronous	Synchronous
Generated currents THD	C-DPC	8.80	6.58	8.22
	NH-DPC	2.27	1.85	1.23
	FH-DPC	2.33	1.86	1.26
	PNN-DPC	2.42	1.82	1.19
	CNN-DPC	2.46	1.84	1.19
THD reduction ratio	NH-DPC compared to C-DPC	74.20%	71.88%	85.04%
	FH-DPC compared to C-DPC	73.52%	71.73%	84.67%
	PNN-DPC compared to C-DPC	72.50%	72.34%	85.52%
	CNN-DPC compared to C-DPC	72.05%	72.04%	85.52%

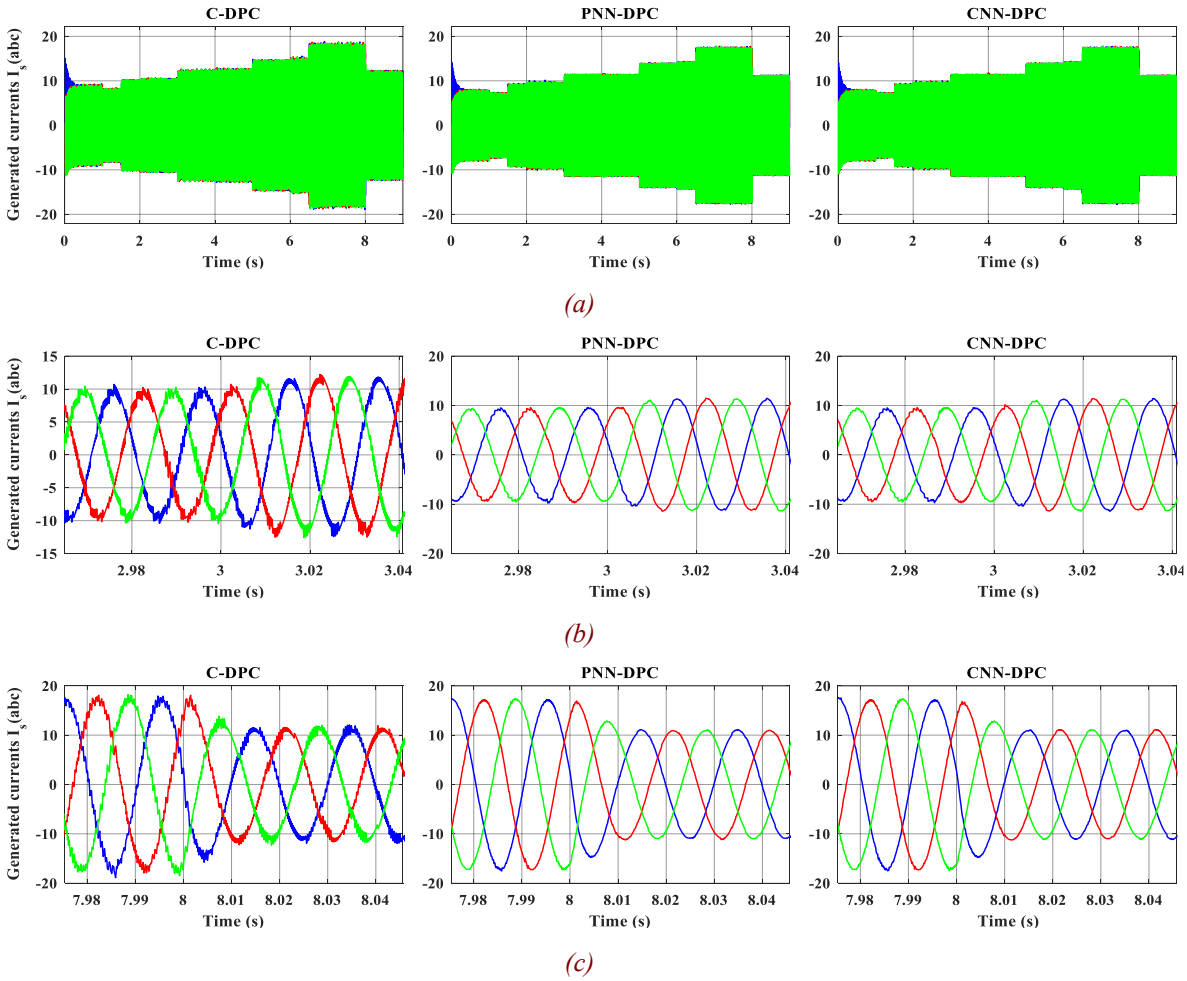

Figure IV-25 : Waveforms of currents generated by the WT-DFIG, using the proposed techniques: The C-DPC, PNN-DPC, and CNN-DPC, (a) generated currents (b) from sub- to synchronous mode. (c) from super-to synchronous mode.

The impact on current quality is directly shown. Figures IV-24 and IV-25 display the three-phase stator current waveforms, visually demonstrating the cleaner, more sinusoidal nature of the currents produced under AI methods (FH/NH/PNN/CNN-DPC) compared to C-DPC. Figure IV-26 presents the crucial FFT analysis results. For each operating mode (sub-synchronous, synchronous, super-synchronous), these figures show the harmonic spectrum of the stator phase 'a' current (Isa) for C-DPC alongside the AI methods. The spectra clearly show a reduction in the amplitude and number of significant harmonic components for the AI controllers. The calculated THD values are explicitly stated on these figures and summarized comprehensively in Table IV-8. This quantitative data confirms the drastic THD reduction from the high levels of C-DPC (6.58%-8.80%) down to the low levels achieved by the AI methods (1.19%-2.46%).

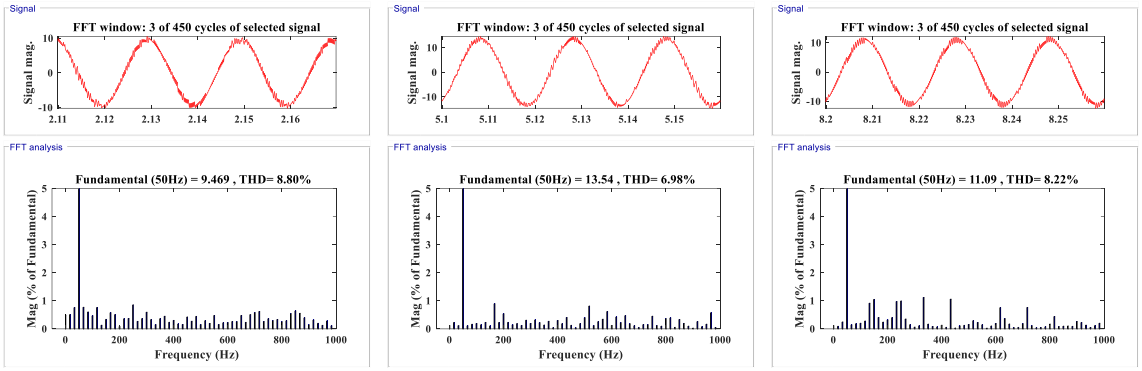

(a)

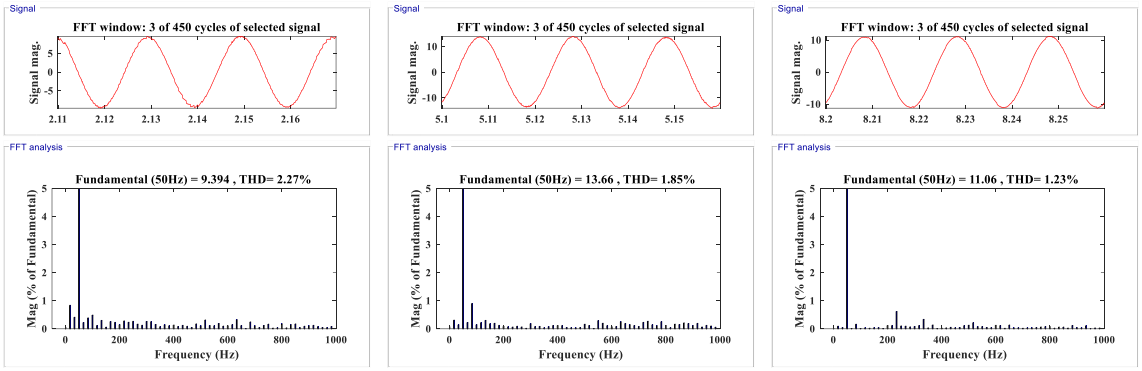

(b)

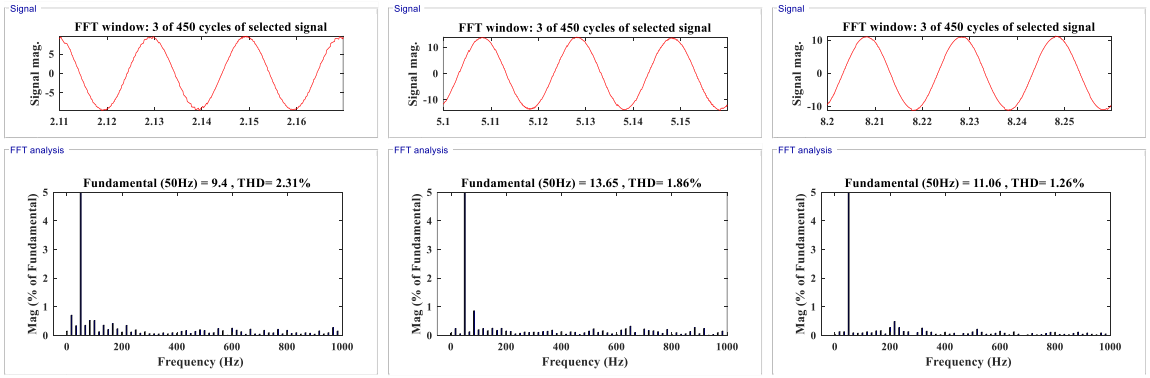

(c)

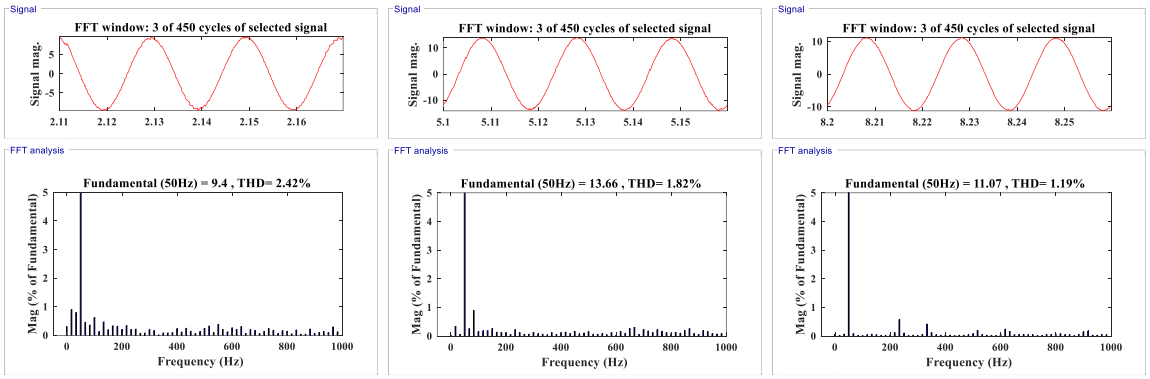

(d)

Figure IV-26 : Generated current of phase (a) and its harmonic spectrum in in Sub-, Super-, and Synchronous Modes for, (a) C-DPC, (b) FH-DPC, (c) NH-DPC, (d) PNN-DPC, (e) CNN-DPC.

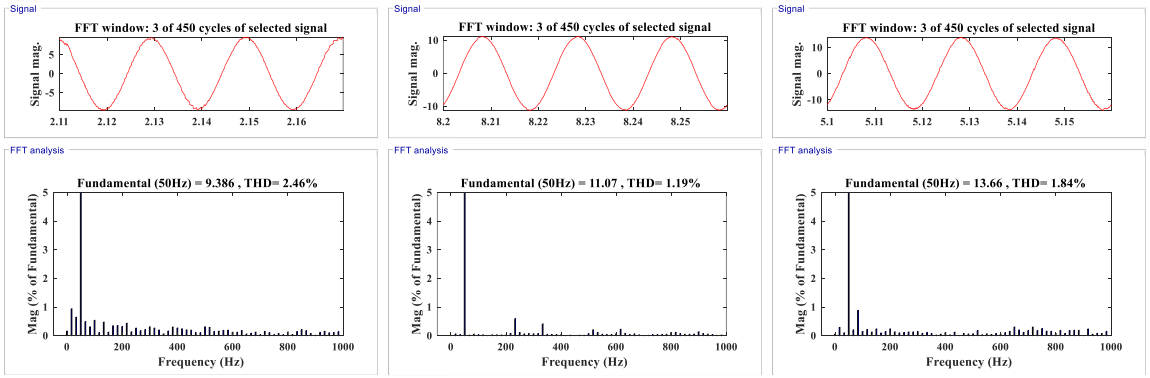

(e)
Figure IV-26 : (Cont.).

IV.6.3. Scenario 2: Random Wind Profile Analysis (Robustness)

This scenario tests the controllers under more realistic, challenging conditions using a continuously varying random wind speed profile. Figure IV-27 display this wind profile (4.96-12 m/s) and the corresponding DFIG speed response, illustrating how the system is driven through its entire operating range, including significant time spent in the overspeed (pitch-controlled) region. The activation of pitch control is confirmed by Figure IV-28, which show the blade pitch angle (β) increasing above 0° during high wind speeds, consequently reducing the power coefficient (Cp) and tip-speed ratio (λ) away from their optimal MPPT values.

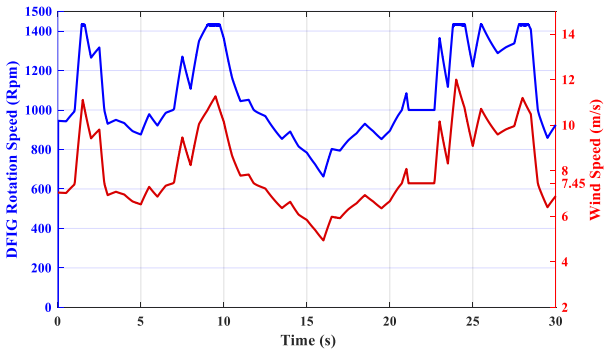

Figure IV-27 : Wind speed profile and DFIG speed .

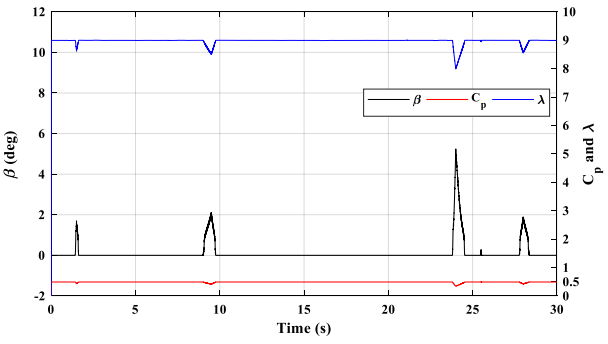

Figure IV-28 : λ, β and C_p .

The generated active power tracking under this random profile is shown in Figure IV-29. These plots demonstrate that despite the continuous wind variations and transitions between MPPT and pitch control, all four AI controllers maintain excellent tracking of the $P_{s-\mathrm{ref}}$. The zoomed sections highlight the controllers' ability to respond rapidly to changes. Local compensated reactive power tracking is shown in Figure IV-30. These confirm that the AI controllers accurately follow the $Q_{AC-\mathrm{ref}}$ throughout the simulation, demonstrating robustness in reactive power management. The reduced ripple compared to C-DPC is also visually evident in these overall plots.

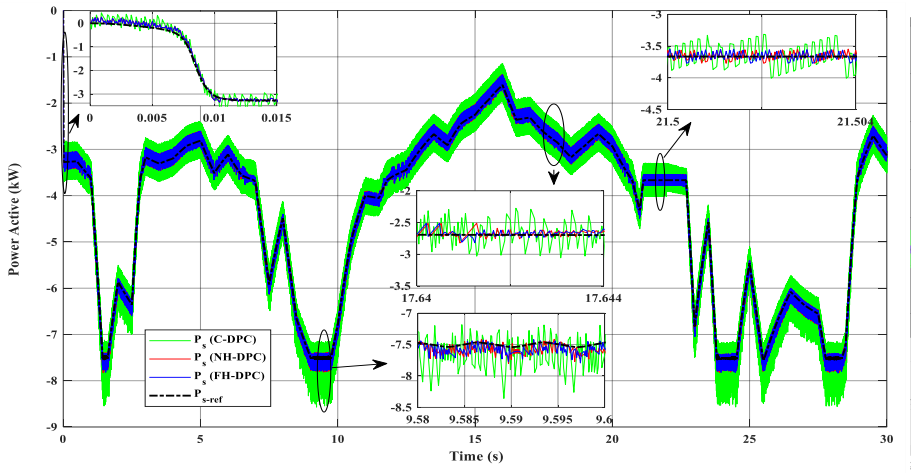

(a)

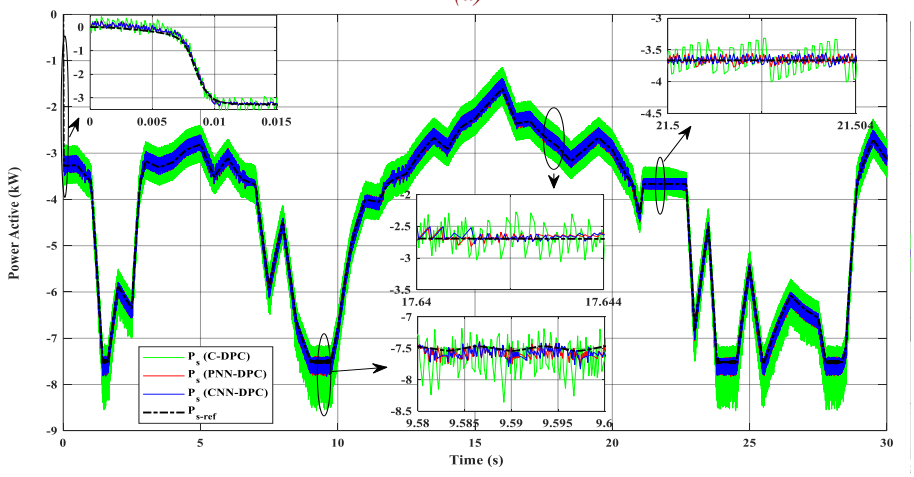

(b)

Figure IV-29 : Generated active power with its reference, (a) using FH/NH-DPC, (b) using PNN/CNN-DPC.

The crucial test is whether the improved power quality is maintained under these dynamic conditions. Figures IV-31 and IV-32 present the stator current waveforms during the random wind simulation. These figures, particularly the zoomed-in sections showing operation during overspeed (b), synchronous (c), and transitions (d), provide compelling visual evidence. The currents under FH-DPC, NH-DPC, PNN-DPC, and CNN-DPC remain significantly cleaner and more sinusoidal compared to the distorted C-DPC currents, irrespective of the operating mode or the rapid fluctuations. This confirms the robustness of the AI methods in delivering superior power quality under realistic operating conditions.

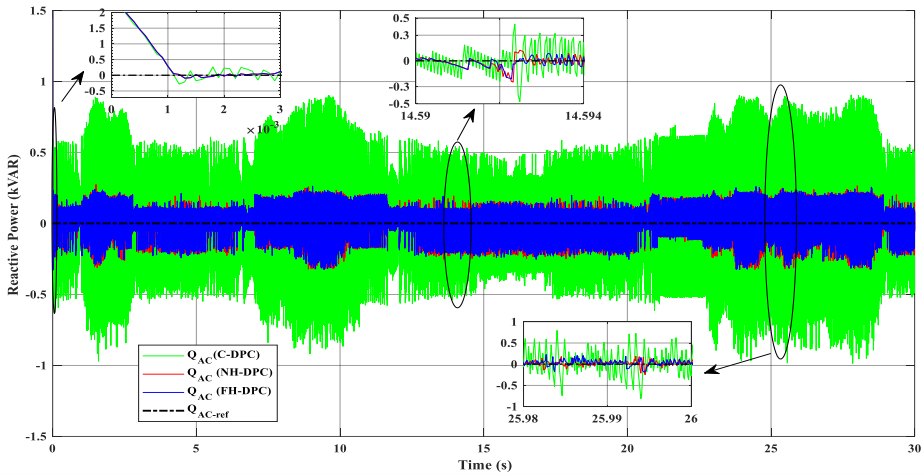

(a)

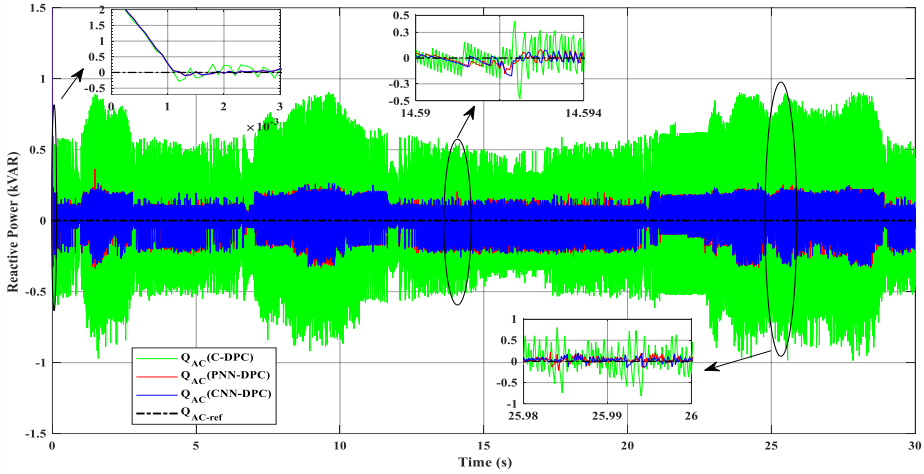

(b)

Figure IV-30 : Local reactive power with its reference using, (a) FH/NH-DPC, (b) PNN/CNN-DPC.

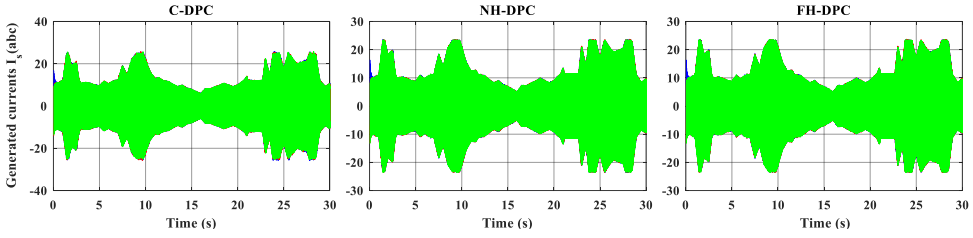

(a)

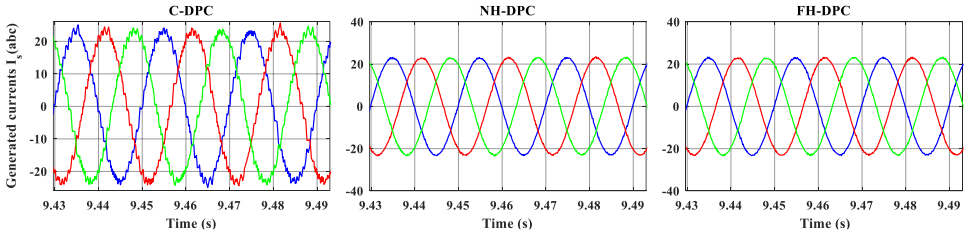

(b)

Figure IV-31 : Waveforms currents generated by the WT-DFIG, using the proposed techniques: The C-DPC, NH-DPC, and FH-DPC, (a) generated currents, (b) overspeed mode, (c) synchronous mode, (d) from super-to sub-synchronous mode.

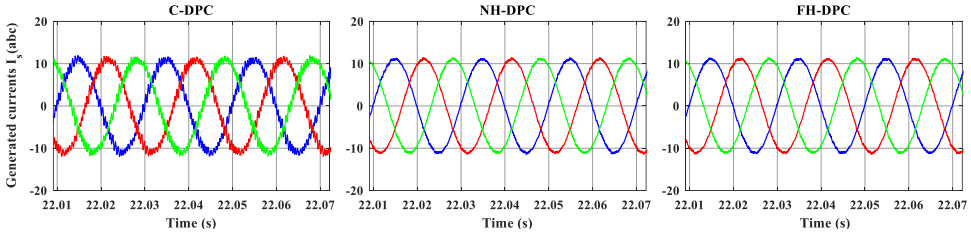

(c)

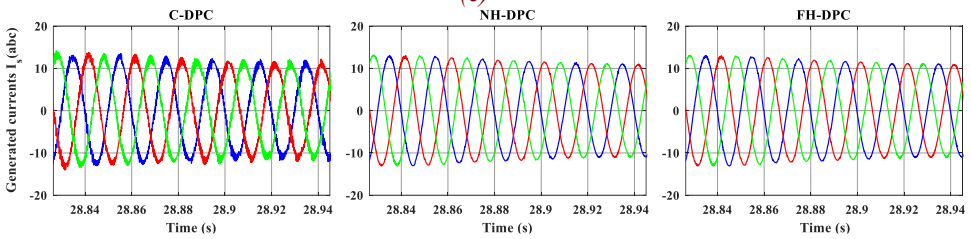

(d)

Figure IV-31 : (Cont.).

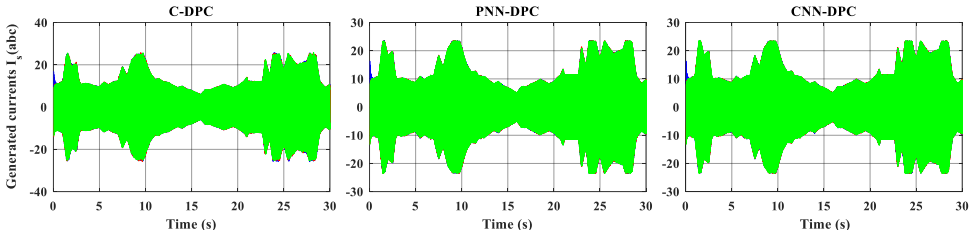

(a)

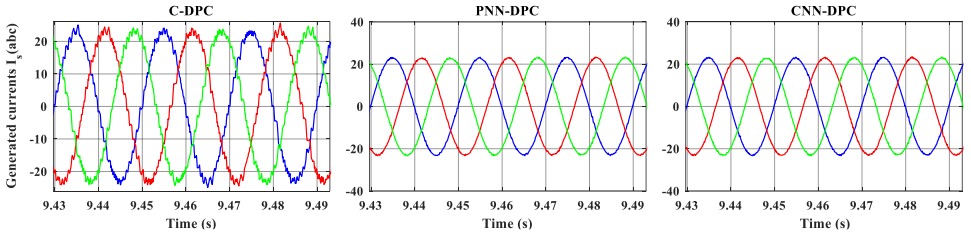

(b)

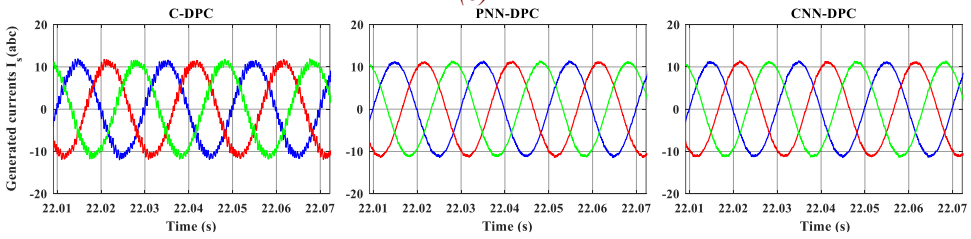

(c)

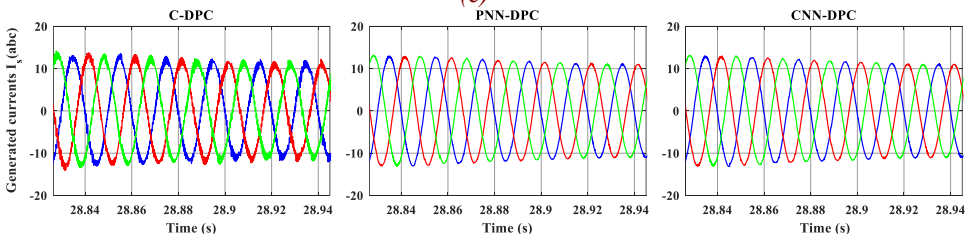

(d)

Figure IV-32 : Waveforms currents generated by the WT-DFIG, using the proposed techniques: The C-DPC, PNN-DPC, and CNN-DPC, (a) generated currents, (b) overspeed mode, (c) synchronous mode, (d) from super- to sub-synchronous mode.

IV.6.4. Discussion on Performance, Implementation, and Trade-offs

The comprehensive simulation results presented in Sections IV.6.2 and IV.6.3 demonstrate the clear superiority of all four proposed AI-DPC strategies (FH-DPC, NH-DPC, PNN-DPC, CNN-DPC) over the baseline C-DPC in terms of power quality enhancement. Evaluating the practical viability and selecting the most suitable approach requires considering not only this enhanced performance but also the associated implementation aspects like design complexity, training effort, and computational load. Table IV-9 provides a consolidated view of these factors and the inherent trade-offs.

- **Performance vs. Complexity:** All four AI methods significantly outperform C-DPC in ripple and THD reduction. The direct vector selection methods (PNN-DPC, CNN-DPC - Strategy 2) offered marginally better quantitative results compared to the hysteresis replacement methods (FH-DPC, NH-DPC - Strategy 1). However, Strategy 2 achieves this with lower final structural complexity by eliminating the switching table, whereas Strategy 1 retains it.
- **Design and Training Effort:** FH-DPC involves medium design complexity based on heuristic fuzzy rule/MF definition, avoiding data-intensive training. All ANN methods (NH, PNN, CNN) necessitate high offline effort for data generation and iterative training/validation. Particularly, CNN-DPC demonstrated the fastest training time among the ANN approaches, offering a significant practical advantage.
- **Computational Load (Execution):** Despite potential offline training demands, all proposed AI controllers are suitable for real-time implementation. The forward pass through trained ANNs (NH, PNN, CNN) is computationally fast. FLC execution (FH-DPC) is also efficient, though potentially slightly slower due to its multi-stage process.
- **Overall Trade-offs and Selection:** The essential trade-off lies between the rule-based transparency of FH-DPC and the potentially higher, data-driven performance and simpler final structure of the ANN methods, particularly PNN/CNN. Considering its top-tier performance in power quality enhancement, combined with the most efficient training process among the ANNs and a streamlined final control structure, CNN-DPC represents the most compelling balance of advantages. It is therefore selected for integration into the broader system analysis in the following chapter.

Table IV-9 : Comparative Summary and Trade-offs of Proposed AI-DPC Strategies.

Feature / Criterion	FH-DPC	NH-DPC	PNN-DPC	CNN-DPC
Performance (vs C-DPC)				
Ps Ripple Reduction	74.84%	74.88%	74.85%	74.84%
QAC Ripple Reduction	77.20%	77.05%	77.07%	77.13%
Current THD Reduction	76.64%	77.04%	76.79%	76.54%
Design & Implementation				
Design Complexity	Medium	High	High	High
Training Effort/Time	N/A	Slow Time (~1.5min)	Slow Time (~2min)	Fastest Time (~48s)
Final Control Structure	Moderate	Moderate	Simple	Simple
Execution time	Moderately	Moderately	Fast	Faster
Overall Assessment	Significant Improvement	Significant Improvement	Superior Performance	Superior Performance
Selected for Next Chapter	No	No	No	Yes

IV.7. CONCLUSION

This chapter has demonstrated the successful application of Artificial Intelligence techniques to significantly enhance the performance of Direct Power Control for WT-DFIG systems, effectively addressing the critical power quality limitations inherent in the conventional C-DPC approach. Four distinct AI-based strategies were investigated: two replacing the hysteresis logic (FH-DPC, NH-DPC) using Fuzzy Logic and Neural Networks, respectively, and two performing direct voltage vector selection via Neural Networks (PNN-DPC and CNN-DPC). Comprehensive simulations under realistic operating conditions confirmed that all proposed AI methods substantially improve upon C-DPC by drastically reducing power ripples and stator current THD, while maintaining fast dynamic response.

Comparing the developed AI strategies revealed nuances in performance and implementation. While the hysteresis replacement methods (FH-DPC, NH-DPC) offered significant improvements, the direct vector selection approaches (PNN-DPC, CNN-DPC) generally achieved marginally better results in ripple and THD reduction, alongside a potentially simpler final control structure by eliminating the switching table.

The Classification Neural Network DPC (CNN-DPC) distinguished itself among these advanced techniques. It consistently delivered top-tier performance, achieving excellent ripple suppression and THD minimization. It is comparable or slightly superior to PNN-DPC and noticeably better than FH-DPC and NH-DPC across various metrics. Furthermore, its classification

method proved highly effective for the discrete nature of voltage vector selection, and it benefited from efficient training compared to other ANN approaches evaluated.

Therefore, based on its demonstrated superior overall performance, robustness under varying conditions, and efficient design, the CNN-DPC strategy is selected as the preferred RSC control method for the subsequent investigations involving the integrated DC microgrid system presented in the next chapter. This selection ensures that the wind energy component within the larger hybrid system operates with the highest achievable power quality based on the findings of this chapter. The results strongly endorse AI-based control, particularly the CNN-DPC approach, as a compelling solution for advancing the control and grid integration of modern WECS.

V

MANAGEMENT AND CONTROL OF THE PROPOSED DC-MICROGRID

V.1. INTRODUCTION

The preceding chapters have laid a robust foundation for this work, beginning with an exploration of the global imperative for renewable energy systems and the inherent control challenges in Chapter I. Subsequently, Chapter II accurately detailed the mathematical modeling of the diverse components constituting the DC-microgrid under investigation, including the DFIG-based wind turbine, photovoltaic array, battery energy storage, and fuel cell system. Chapters III and IV critically evaluated classical control strategies for the DFIG and culminated in the development and selection of an advanced Classification Neural Network Direct Power Control (CNN-DPC) for the DFIG's Rotor Side Converter (RSC), demonstrating significant enhancements in power quality.

This chapter represents the synthesis and application of these foundational elements. It focuses on the management and control of the integrated DC-microgrid. The primary contributions of this chapter are threefold:

The development and implementation of control strategies for the remaining individual microgrid components, most especially a Fuzzy Logic-based Direct Power Control (Fuzzy-DPC) for the DFIG's Grid Side Converter (GSC), Fuzzy MPPT for the PV, alongside appropriate controllers for battery and fuel cell systems.

The systematic sizing of the DC-microgrid components ensures operational viability and meets energy demands.

The design and validation of a comprehensive rule-based Energy Management System (EMS), engineered to orchestrate the power flow between all sources and storage element, optimize renewable energy utilization, safeguard battery health, and ensure reliable power delivery.

The chapter will systematically describe, beginning with the detailed design of the individual component controllers. This will be followed by a presentation of the microgrid sizing methodology

and the parameters of the configured system. The core EMS algorithm will then be detailed, outlining its operational logic and decision-making processes. Finally, the performance of the fully integrated DC-microgrid, operating under the proposed control and management strategies.

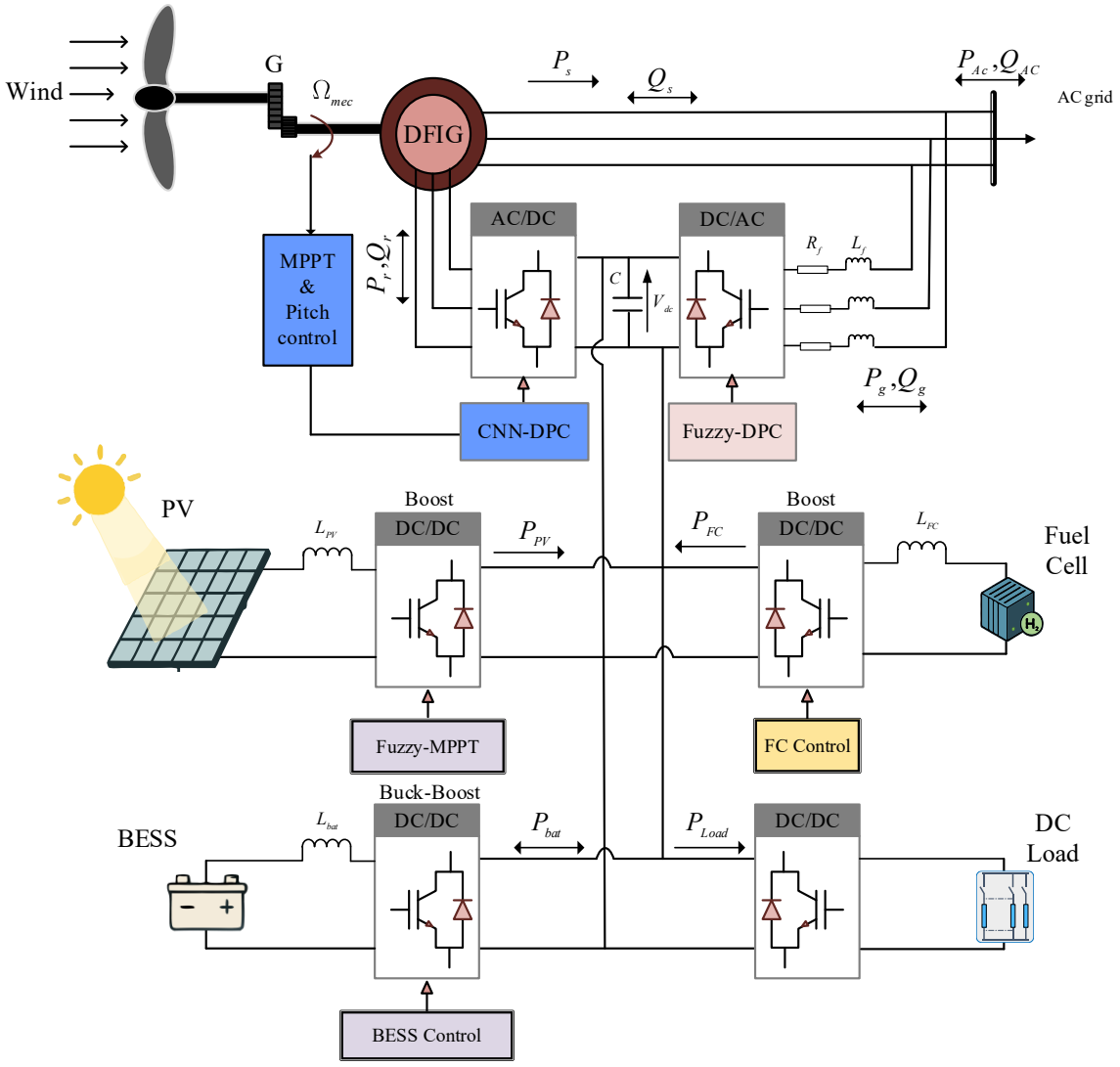

Figure V-1: Overall scheme of proposed DC-MG.

V.2. DETAILED DC-MICROGRID SYSTEM DESCRIPTION

V.2.1. Overall Topology and Component Interconnections

The DC-microgrid concted to AC grid system under investigation, as globally depicted in Figure I-1, integrates a Wind Turbine Doubly-Fed Induction Generator (WT-DFIG), a Photovoltaic (PV) array, a Battery Energy Storage System (BESS), and a Fuel Cell (FC) system. These components are all interconnected via a common DC bus, as illustrated in Figure V-1. The system is

designed primarily to supply a variable DC load, with capabilities for AC grid managed by AC/DC power converters.

The WT-DFIG's stator is typically connected to an AC point of common coupling, while its rotor circuit is connected to the DC bus via a back-to-back converter, the DC link of which forms part of the main DC bus. The PV array is interfaced to the DC bus through a DC/DC boost converter. The BESS utilizes a bidirectional DC/DC buck-boost converter for charging and discharging operations. The FC system, serving as a backup power source, is connected to the DC bus via a unidirectional DC/DC boost converter. The nominal DC bus voltage for the microgrid is maintained at $V_{dc_{ref}} = 880\ V$.

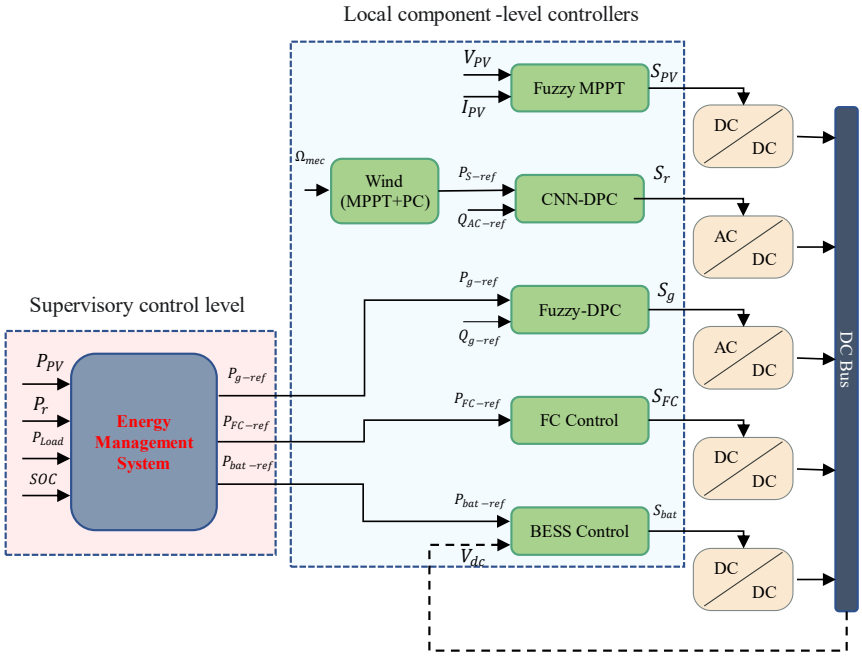

Figure V-2 : Hierarchical control architecture.

V.2.2. Control Hierarchy Overview

The control architecture of the DC-microgrid is hierarchical, as presented in Figure V-2 , comprising:

- **Local Controllers:** Dedicated control systems for each individual component. These are responsible for achieving local objectives such as Maximum Power Point Tracking (MPPT) for the PV system, power tracking and reactive power compensation for the WT-DFIG (RSC and GSC), charge/discharge current regulation for the BESS, and power output regulation for the FC system.

- **Supervisory Energy Management System (EMS):** A higher-level control system that coordinates the operation of all local controllers. The EMS makes decisions regarding power dispatch from different sources and storage units to ensure overall system stability, optimize resource utilization, and meet load demands.

This layered control approach allows for modular design and robust operation of the complex microgrid system.

V.3. COMPONENT DESCRIPTION AND SIZING

This section provides a detailed description of each key component constituting the integrated DC-microgrid. For each component, its designated role within the overall system architecture, the rationale and specifics of its sizing adopted for this research, and its primary operational characteristics are presented. A clear understanding of the individual component capacities and how they interface is essential before delving into their local control strategies and the overarching Energy Management System. The WT-DFIG, with its 7.5 kW rated power, serves as a primary generation unit and a reference for dimensioning other components to ensure a balanced and resilient system. A comprehensive diagram illustrating all component interconnections and their respective power converter interfaces within the DC-microgrid is provided in Figure V-1.

V.3.1. Wind Turbine System: Description and Sizing

The Wind Turbine Doubly-Fed Induction Generator (WT-DFIG) system serves as one of the primary renewable energy sources in the microgrid. Its ability to operate at variable speeds allows for enhanced energy capture from the wind across a range of conditions.

V.3.1.1. Role and Configuration in the DC-Microgrid

The DFIG is configured with its stator windings directly connected to an AC grid. The DFIG's rotor circuit is interfaced with the common DC bus of the microgrid via a back-to-back AC/DC/AC power electronic converter. This converter consists of a Rotor Side Converter (RSC) and a Grid Side Converter (GSC), which share a common DC link capacitor. This DC link is directly integrated to the microgrid. This configuration enables bidirectional power flow through the rotor circuit, facilitating control over the DFIG's rotational speed, its generated power output injected into the AC side via the stator, and the local compensated reactive power exchanged with

the AC grid. The GSC plays a crucial role in managing active and reactive power at its own AC interface.

V.3.1.2. WT-DFIG Sizing

The WT-DFIG system is dimensioned with a rated power of 7.5 kW. This capacity was chosen as a representative size for distributed wind generation and serves as the main renewable energy contributor. Its parameters, detailed in the Appendix, are consistent with the models analyzed in previous chapters. The sizing of other components is considered in relation to this primary generator to ensure complementary operation and adequate coverage of load demands.

V.3.2. Photovoltaic System: Description and Sizing

The Photovoltaic (PV) system serves as the second primary renewable energy source, converting solar irradiance directly into DC electrical power. Its generation profile typically complements that of the wind system.

V.3.2.1. Role and Configuration

The PV array is connected to the DC bus via a unidirectional DC/DC boost converter. The primary functions of this converter are to step up the relatively lower voltage output of the PV array to the higher DC bus voltage and to facilitate Maximum Power Point Tracking (MPPT), ensuring optimal energy harvest from the available solar irradiance.

V.3.2.2. PV System Sizing and Panel Configuration

The PV system is designed for a nominal peak power of 5.5 kWp under Standard Test Conditions (1000 W/m², 25°C). This capacity was selected to be approximately 75% of the WT-DFIG's rated power (7.5 kW), aiming for a substantial daytime energy contribution that complements the wind resource without oversizing relative to the primary generator.

This is achieved using SIEMENS SM 110-24 PV panels, each with a nominal peak power of 110 W and a V_{mpp} of approximately 35V; the main characteristics of this panel are detailed in the Appendix. To reach the target 5.5 kW output and ensure a suitable input voltage range for the DC/DC boost converter, the array is configured with 10 panels connected in series to form a string, resulting in a nominal V_{mpp} of approximately 350V per string. 5 such strings are then connected in parallel, utilizing a total of 50 panels and confirming the system's total peak power of 5.5 kWp.

V.3.3. Battery Energy Storage System : Description and Sizing

V.3.3.1. Role and Configuration

The Battery Energy Storage System (BESS) is a critical component for ensuring the stability, reliability, and flexibility of the DC-microgrid. It acts as an energy buffer, mitigating the intermittency of renewable sources and facilitating load balancing.

The Battery Energy Storage System (BESS) is interfaced with the common DC bus via a bidirectional DC/DC buck-boost converter. This crucial component allows the BESS to charge by absorbing surplus electrical energy from the DC bus when renewable generation exceeds load demand, and to discharge by supplying stored electrical energy to the DC bus when load demand surpasses renewable generation. Its primary roles within the microgrid include short-term energy shifting, power smoothing, contributing to DC bus voltage stability during transients, and improving the overall power quality.

V.3.3.2. BESS Sizing

The Battery Energy Storage System (BESS) is dimensioned to provide both adequate power delivery capability and sufficient energy storage capacity for anticipated operational requirements. Its bidirectional converter boasts a power rating of 10 kW, enabling the BESS to rapidly charge or discharge at rates sufficient to cover a significant portion of the 10-kW peak load or absorb substantial surpluses from renewable generators. The energy capacity target is set to provide approximately 3 hours of autonomy at the average microgrid load of 5 kW, translating to a usable stored energy requirement of 15 kWh. A nominal system voltage of 420V for the battery bank is chosen for compatibility with typical bidirectional converter designs, which can be achieved by connecting a suitable number of lower-voltage battery cells or modules in series, such as 35 units of 12V nominal batteries.

To deliver the 15 kWh of usable energy, the nominal Amp-hour capacity is calculated to be approximately 55.80 Ah.

$$Ah_{BESS\_nominal} = \frac{15000\ \text{Wh}}{420\ V \times 0.64} \approx 56\ \text{Ah} \qquad \text{(V-1)}$$

Furthermore, to protect the battery from excessive stress and prolong its operational life, the Energy Management System (EMS) will manage the BESS to operate primarily within a State of Charge (SOC) range of 20% SOC_{min} to 80% SOC_{max}.

V.3.4. Fuel Cell System: Description and Sizing

The Fuel Cell (FC) system is integrated into the DC-microgrid to provide long-duration backup power, as auxiliary power generation system, particularly during extended periods of low renewable energy availability when the BESS may become depleted.

V.3.4.1. Role and Configuration

The Fuel Cell (FC) system, specifically a Proton Exchange Membrane Fuel Cell (PEMFC) type, is integrated into the DC-microgrid as a crucial auxiliary power generation system. Unlike renewable energy sources which depend on variable environmental conditions, the FC's primary function is to provide reliable, dispatchable backup power for several hours when needed. It ensures continuity of supply to critical loads during extended periods of low renewable energy availability or when the BESS is significantly depleted and cannot meet the demand.

The FC system is connected to the common DC bus via a unidirectional DC/DC boost converter. This converter is necessary to step up the relatively lower and variable voltage output of the FC stack to the stable DC bus voltage and to control the power drawn from the FC. An associated hydrogen storage system is assumed to supply fuel to the FC; its operational duration is therefore limited by the available fuel, not by environmental intermittency like solar or wind.

V.3.4.2. FC System Sizing

The fuel cell system has a rated power output of 5 kW. The sizing of the system is determined by the average load demand and the FC system's function as an auxiliary power generation system, with the capacity to operate for several hours. The 5-kW capacity of the FC system is directly proportional to the microgrid's designed average load demand of 5 kW. Upon activation, this functionality enables the FC to provide comprehensive support to the microgrid's standard power requirements for a designated duration, thus ensuring that the typical operational demands can be fulfilled even in circumstances where renewable energy inputs are unavailable and the BESS contribution has been fully utilized.

V.3.5. DC Load Profile: Description and Parameters

A realistic and representative DC load profile is essential for simulating the microgrid's dynamic behavior and rigorously evaluating the performance of the control strategies and the Energy Management System.

The DC load profile is designed to emulate the aggregated demand of consumers connected to the microgrid, with its shape reflecting typical consumption patterns observed in applications such as small commercial establishments or isolated communities. Generally, this profile features low power consumption during overnight and early morning hours, followed by a gradual increase as daily activities commence. It also typically includes one or more peaks during daytime or evening hours, corresponding to peak activity or residential demand, alongside periods of moderate or fluctuating load throughout the day. A 24-hour profile exhibiting these general characteristics is constructed to provide a realistic challenge for the microgrid's energy management.

For the purpose of quantitative analysis and system evaluation in this study, the generic 24-hour load profile shape is scaled to achieve specific parameters. A Peak Load Demand of approximately 9 kW is established; this maximum instantaneous demand serves as a critical design point for ensuring the microgrid can meet high power requirements through the coordinated dispatch of all available generation and storage assets. Furthermore, an Average Load Demand of approximately 5 kW over the 24-hour cycle is defined.

V.4. LOCAL CONTROL STRATEGIES FOR INDIVIDUAL MICROGRID COMPONENTS

The synergistic operation of the DC-microgrid necessitates robust and efficient control of each constituent energy source and storage unit. This section details these control strategies, integrating the advanced AI-based control for the DFIG-RSC developed in Chapter IV and proposing intelligent control for other critical interfaces, such as the DFIG-GSC and MPPT of PV.

V.4.1. Wind Turbine Based On DFIG System Control

The WT-DFIG system, as a primary fluctuating renewable source, requires sophisticated control for both its rotor-side and grid-side converters to maximize energy capture and ensure stable DC bus integration.

V.4.1.1. Rotor Side Converter Control: Implementation of Classification Neural Network DPC (CNN-DPC)

The control of the DFIG's RSC is pivotal for optimizing power extraction from the wind and managing local reactive power exchange at AC grid. As comprehensively demonstrated in Chapter IV, the developed CNN-DPC strategy significantly outperformed conventional C-DPC by substantially reducing power ripple and current THD, thereby enhancing power quality. This CNN-DPC, which directly classifies the optimal voltage vector for the RSC, is thus adopted for the DFIG within the integrated microgrid. Its function will be to precisely track the active power reference P_{s-ref} ,derived from the MPPT algorithm or pitch control limits detailed in Chapter III, and the reactive power reference Q_{AC-ref}.The overall control structure of the DFIG-based wind energy conversion system incorporating the CNN-DPC scheme is illustrated in Figure IV-15.

V.4.1.2. Grid Side Converter Control: Proposed Fuzzy Logic-based Direct Power Control (Fuzzy-DPC)

The Grid-Side Converter (GSC) plays a critical role in the WT-DFIG system. Its primary functions are to maintain unity power factor operation by ensuring zero reactive power exchange with the AC grid $Q_g = 0$, and to manage the active power P_g supplied to or drawn from the grid, to meet the demands of a connected DC Microgrid (DC-MG). To enhance the GSC's performance beyond that achievable with classical Direct Power Control (DPC) methods in section III.5, this work proposes an advanced control strategy. The development of this strategy is inspired by the principles discussed in [60]. The detailed control of the proposed GSC strategy is depicted in Figure V-3.

- **Controller Design**

The GSC Fuzzy-DPC is designed to regulate the active power (P_g) exchanged by the GSC. It also aims to control the reactive power (Q_g). The FLC effectively replaces conventional hysteresis comparators and the associated switching table.

The FLC is architected with three crisp inputs: the active power error, defined as $eP_g = P_{g-ref} - P_g$; the reactive power error, $eQ_g = Q_{g-ref} - Q_g$; and the angular sector of the AC voltage vector, θ_g. The FLC produces a single crisp output, which is the index of the optimal voltage vector to be applied by the GSC.

Table V-1 : GSC Fuzzy-DPC rule.

eQ_g	eP_g	N					
		I	II	III	IV	V	VI
P	P	V_3	V_4	V_5	V_6	V_1	V_2
	Z	V_5	V_6	V_1	V_2	V_3	V_4
Z	P	V_2	V_3	V_4	V_5	V_6	V_1
	Z	V_1	V_2	V_3	V_4	V_5	V_6

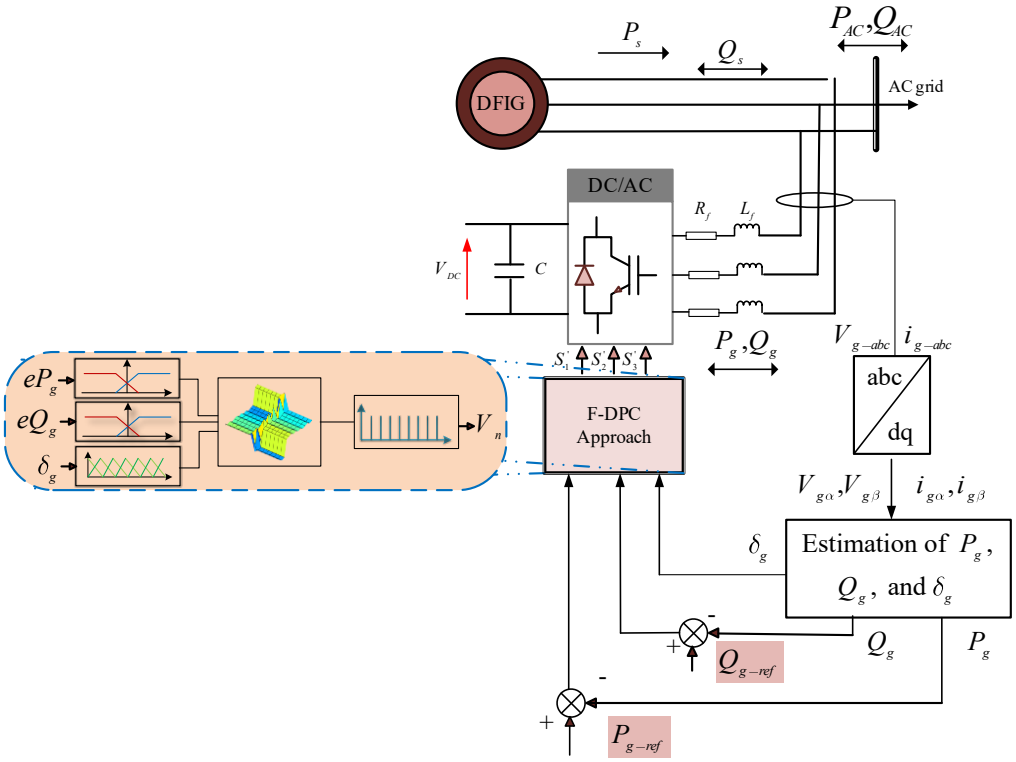

Figure V-3 : Block diagram of GSC Fuzzy-DPC implementation.

- **FLC Implementation**
  - **Fuzzification:** The input active power error eP_g is fuzzified using two Membership Functions (MFs), for example, Negative (N) and Positive (P), typically employing trapezoidal. The input reactive power error eQ_g also utilizes two MFs, such as Negative (N) and Positive (P), with similar MF. The input AC voltage vector angle θ_g is fuzzified into six linguistic variables (e.g., θ_1 to θ_6) using triangular MFs.
  - **Rule Base:** The core control logic is embedded in a set of 24 IF-THEN rules. This number arises from the combination of input MFs (2 MFs for e_{P_g} × 2 MFs for e_{Q_g} × 6 MFs for θ_{vg}). The rules are presented in Table V-1. These rules map the linguistic

combinations of input conditions to the optimal output voltage vector. The Mamdani inference system was employed for processing these rules.

- **Defuzzification:** The aggregated fuzzy output, representing the combined conclusion from all active rules, is defuzzied using the Bisector method. The output variable, representing the selected voltage vector to be applied, is characterized by singleton MFs.

V.4.2. Photovoltaic System MPPT Control

To maximize the power extracted from the PV array under varying solar irradiance and temperature conditions, effective Maximum Power Point Tracking (MPPT) is essential. This work considers both a conventional Perturb and Observe (P&O) algorithm and a Fuzzy Logic-Based MPPT (Fuzzy-MPPT), drawing inspiration from the methods discussed in [61, 152].

V.4.2.1. Conventional Perturb and Observe (P&O) MPPT Algorithm

The Perturb and Observe (P&O) algorithm is a prevalent MPPT technique favored for its simple implementation. It works by incrementally changing the PV array's operating voltage, via the DC/DC boost converter's duty cycle, and observing the impact on output power. If power increases, the voltage change continues in the same direction; otherwise, the direction is reversed. Despite its simplicity, P&O can cause oscillations around the MPP in stable conditions and may struggle to track effectively during rapid atmospheric shifts, as noted [61].

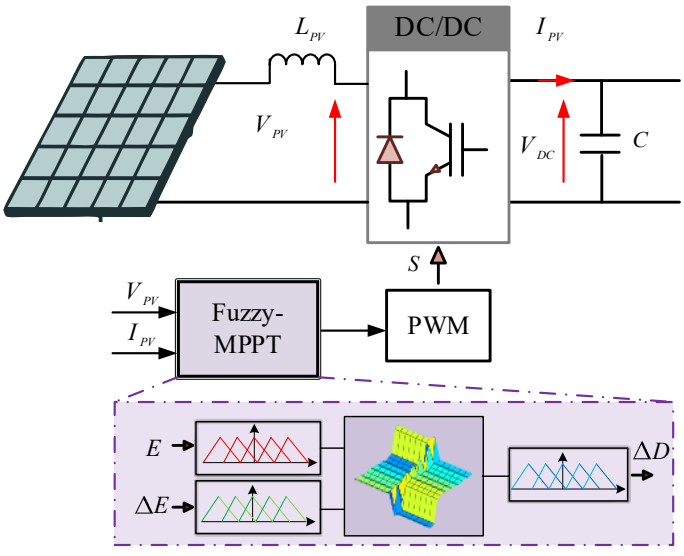

Figure V-4 : Overall scheme of PV and its Fuzzy-MPPT.

V.4.2.2. Fuzzy Logic-Based MPPT (Fuzzy-MPPT)

To overcome the drawbacks of conventional P&O, a Fuzzy Logic-Based MPPT (Fuzzy-MPPT) is proposed. FLCs surpass at handling PV array non-linearities and offer superior tracking, especially under fluctuating irradiance and partial shading. This Fuzzy-MPPT aims for faster, more accurate MPP tracking, reduced oscillations, and greater robustness to atmospheric dynamics compared to P&O. The design follows [152] and the overall structure of the Fuzzy-MPPT is illustrated in Figure V-4.

- **FLC Design for PV MPPT**
  - **Input Variables:** Two inputs are derived from PV power P_{pv} and voltage V_{pv}:
    - Error $E(k) = \frac{\Delta P_{pv}(k)}{\Delta V_{pv}(k)}$: Slope of the P-V curve.
    - Change in Error $\Delta E(k) = E(k) - E(k-1)$.
  - **Output Variable:** The change in the DC/DC boost converter's duty cycle ΔD.
  - **Fuzzification & Membership Functions**: Inputs $(E, \Delta E)$ and output (ΔD) are converted to linguistic variables, including NB, NS, ZE, PS, PB, using MFs triangular and trapezoidal.
  - **Fuzzy Rule Base:** IF-THEN rules are established from heuristic knowledge of PV behavior and MPPT, as exemplified in Table V-2.
  - **Inference & Defuzzification:** A Mamdani inference system is used, with defuzzification center of gravity method yielding a duty cycle crisp ΔD.

Table V-2 : Fuzzy-MPPT rule.

E/dE	NB	NS	ZE	PS	PB
NB	ZE	ZE	PB	PB	PB
NS	ZE	ZE	PS	PS	PS
ZE	PS	ZE	ZE	ZE	NS
PS	NS	NS	NS	ZE	ZE
PB	NB	NB	NB	ZE	ZE

V.4.3. Battery Energy Storage System Control

The BESS plays a critical role in the DC-microgrid by providing short-term energy balancing, smoothing power fluctuations from renewable sources, and supporting the DC bus voltage during transient conditions. Its control is principal for achieving these functions effectively and safely.

The primary control objectives for the BESS are:

- To maintain DC bus voltage stability by rapidly absorbing surplus power or supplying deficit power as needed.
- To manage its State of Charge (SOC) within predefined safe operating, 20\% to 80\%, to prevent overcharging or deep discharging, thereby maximizing battery lifespan.
- To respond to power dispatch commands $P_{bat-ref}$ from the Energy Management System (EMS).

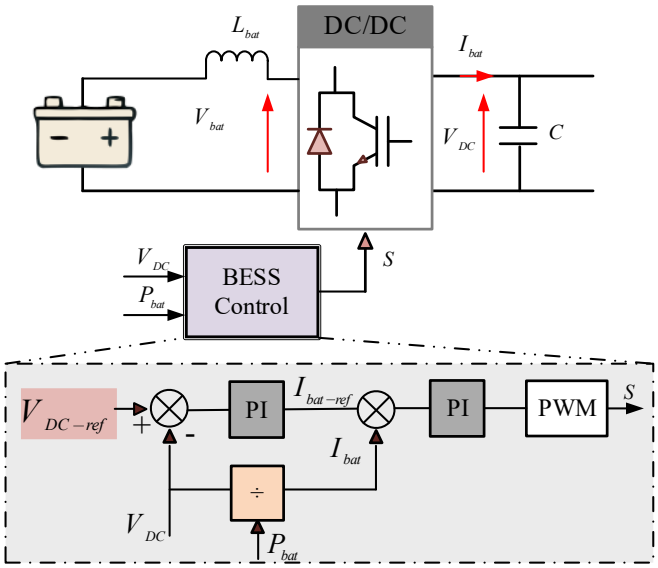

Figure V-5 : Global structure of BESS control.

The BESS is connected to the DC bus via a bidirectional DC/DC buck-boost converter, whose control employs a cascaded loop structure [85]. The overall converter control scheme is illustrated in Figure V-5.

- **Inner Current Control Loop:** A fast-acting inner loop, employing a Proportional-Integral (PI) controller, regulates the battery current I_{bat} to accurately follow the reference current $I_{bat-ref}$ generated by the outer loop. This loop directly manipulates the duty cycles of the bidirectional converter's switches and is crucial for precise current control during charging and discharging.
- **Outer Voltage Control Loop:** The outer control loop is responsible for strategically determining the battery current reference, $I_{bat-ref}$, which dictates the overall charging or discharging power of the BESS. It actively stabilizes the DC bus voltage V_{dc} through a Proportional-Integral (PI) controller that processes the error between the DC bus voltage reference and its measured value, providing a current component for rapid voltage support.

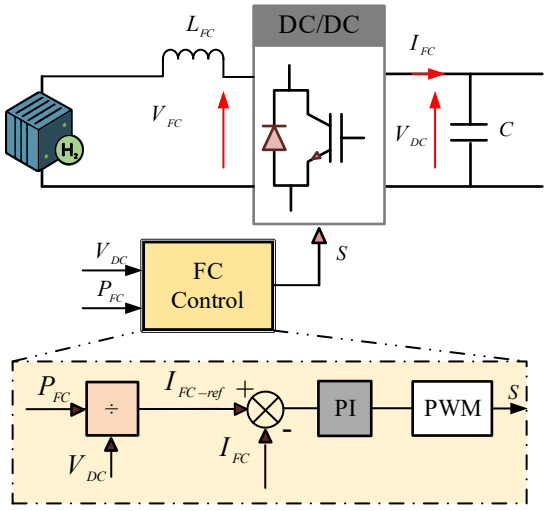

Figure V-6 : Global structure of FC control.

V.4.4. Fuel Cell System Control

The Fuel Cell system serves as a longer-term backup power source in the microgrid, primarily activated during extended periods of low renewable generation or when the BESS is significantly depleted. Its control is also important.

The control objectives for the FC system are:

- To dispatch electrical power P_{FC} according to the commands received from the EMS.
- To manage its operational constraints, such as ensuring slow power ramp rates to protect the FC stack from rapid load changes.

The FC system is connected to the DC bus via a unidirectional DC/DC boost converter. Its control typically involves: A PI controller that regulates the FC output current to match the reference power setpoint current setpoint I_{FC-ref} provided by the EMS. The controller achieves this by adjusting the duty cycle of the boost converter [62], as shown in Figure V-6.

V.5. ENERGY MANAGEMENT SYSTEM DESIGN

The Energy Management System (EMS) is the central supervisory controller orchestrating the DC-microgrid's power sources (WT-DFIG, PV), storage (BESS), and loads, including interaction with the AC grid via the Grid Side Converter (GSC). Its primary objectives are to maximize renewable energy use, ensure DC bus stability through power flow management, maintain BESS State of Charge (SOC) within 20%-80% (incorporating hysteresis), optimize Fuel Cell (FC) operation, and coordinate grid power exchange. A rule-based strategy is employed for its transparency and implementation ease.

The EMS logic relies on several predefined setpoints and calculated variables:

- **Net Power** P_{net}: This crucial variable represents the instantaneous power balance on the DC bus from renewable sources and the load. It is calculated as:

$$P_{net} = P_{PV} + P_r - P_{Load} \quad \text{(V-2)}$$

A positive P_{net} indicates surplus power available for BESS charging or export. A negative P_{net} indicates a power deficit that needs to be met by BESS discharging, FC operation, or grid import.

- **BESS SOC Thresholds and Operational States:** To manage BESS health and guide operational decisions, distinct SOC states are defined, incorporating hysteresis in transitions to prevent rapid cycling: Critically Low SOC_{min}, Low state SOC_{low}, Normal SOC_{normal}, High SOC_{high}, and Full SOC_{max}. The hysteresis-based definitions of the Low [153], Normal, and High SOC thresholds are illustrated in the flowchart in Figure V-7.

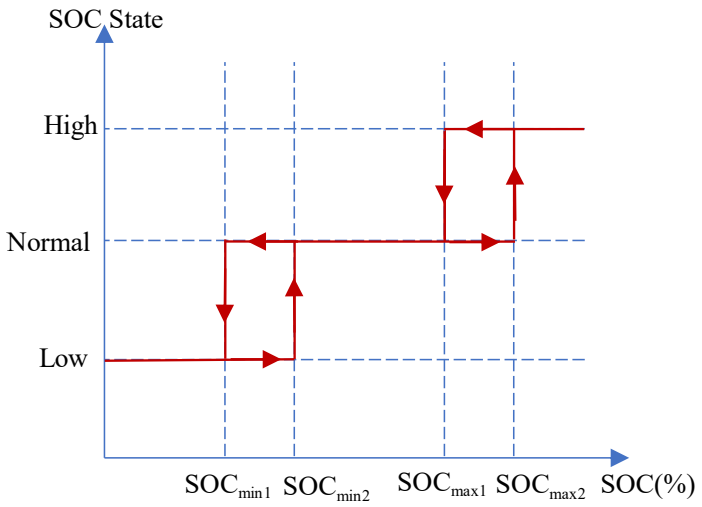

Figure V-7 : SOC Thresholds and Hysteresis Transitions in BESS.

- **Maximum Power Limits:** These define the operational boundaries for the controllable units: Maximum power limits for BESS charge/discharge $\left(P_{bat-max}^{charge}, P_{bat-max}^{discharge}, P_{bat-low}^{discharge}\right)$, and FC (P_{FC-max}).
- **Power Sharing Ratios:** When both BESS and FC are to contribute to covering a deficit**:** Proportion of deficit supplied by BESS $R_{btt} = \frac{P_{bat-max}^{discharge}}{P_{FC-max} + P_{bat-max}^{discharge}}$, Proportion of deficit supplied by FC.$R_{FC} = \frac{P_{FC-max}}{P_{FC-max} + P_{bat-max}^{discharge}}$.

The core operational logic of the EMS is designed to manage power flow across various system conditions, determined primarily by P_{net} and the BESS SOC state. The decision-making

process, detailed in the flowchart in Figure V-8, can be summarized into the following primary scenarios:

With surplus power $P_{net} > 0$ and a full BESS $SOC \geq SOC_{max}$, all surplus is exported to the grid; if surplus power exists but the BESS can still charge $SOC < SOC_{max}$, the BESS absorbs this surplus up to its limit, with any remainder exported, and in both these surplus cases, the Fuel Cell (FC) is off. During a power deficit $P_{net} \leq 0$, if the BESS is critically low $SOC \leq SOC_{min}$, it avoids discharging, the FC attempts to meet the deficit up to its maximum P_{FC-max},, and the grid imports any remaining shortfall. For a deficit with a usable BESS $SOC > SOC_{min}$: at SOC_{high}, the BESS primarily covers the deficit; at SOC_{normal}, the BESS and FC share the load based on predefined ratios, and at SOC_{low}, the FC is prioritized, with the BESS contributing secondarily under a reduced discharge limit $P_{bat-low}^{discharge}$, before relying on grid import for any further unmet deficit.

The total active power P_{AC} exchanged with the external AC grid, considers both the power flow through the DFIG stator P_s and the power flows through the GSC P_g, which is directly managed by the EMS. The relationship is given by:

$$P_{AC} = P_g + P_s \tag{V-3}$$

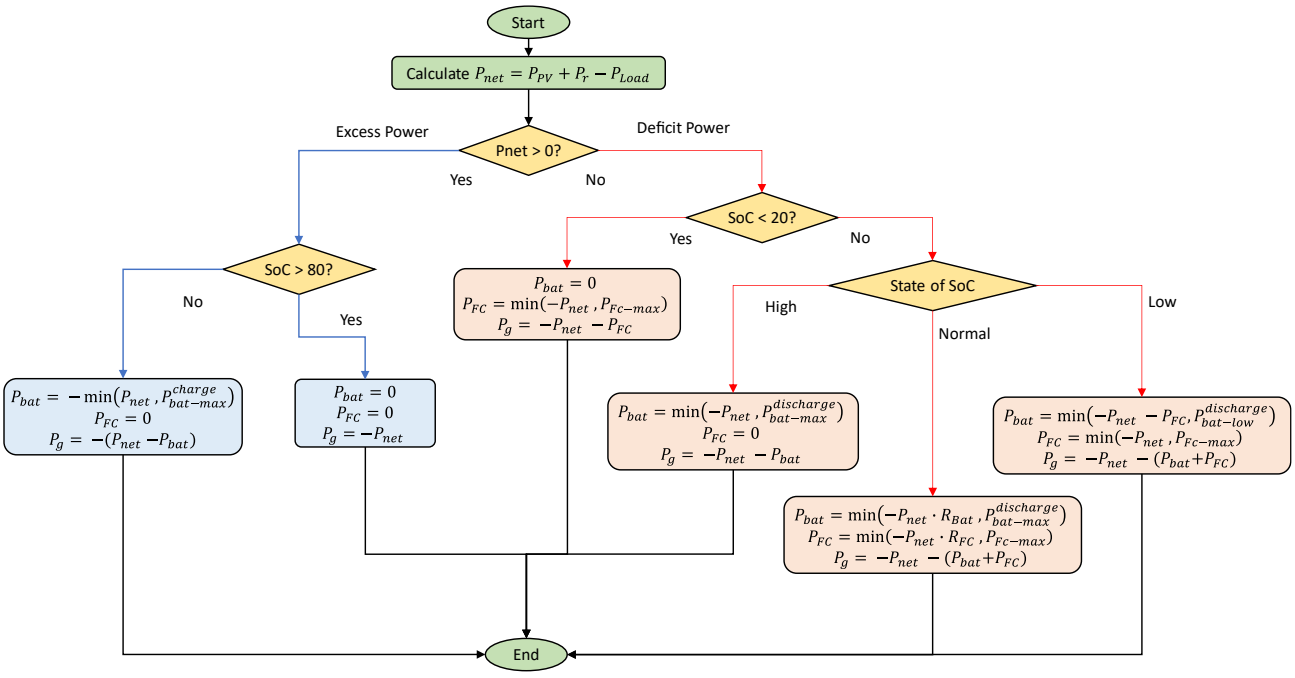

Figure V-8: Flowchart of EMS.

V.6. RESULTS AND DISCUSSION

This section presents a detailed analysis and discussion of the simulation results obtained from the integrated DC-microgrid. The system's performance, operating under the developed local control strategies and coordinated by the rule-based Energy Management System (EMS), was evaluated using MATLAB/Simulink. The microgrid was subjected to dynamic environmental conditions and a variable DC load profile, as established in Section V.3, to assess its real-world applicability and the efficacy of the control background.

The operational context for the simulation is defined by the environmental inputs and load demands. Figure V-9 illustrates the time-varying profiles of wind speed (v), solar irradiance (G), and the consequent DFIG mechanical speed (Ω_m) over the 24-hour simulation period. The wind speed fluctuates significantly, ranging from a low of approximately 5.2 m/s to a peak of 11.8 m/s, compelling the WT-DFIG to operate across its entire speed range, including MPPT and pitch-controlled regions. The DFIG's rotational speed, (Ω_m), is observed to effectively track these wind variations, demonstrating responsive control. The solar irradiance follows a typical diurnal pattern, reaching a maximum of 1000 W/m^2 around noon. The imposed DC load power and the local AC reactive power demand (Q_{AC-ref}) for the DFIG are presented in Figure V-10. The DC load exhibits distinct peaks, for instance, reaching ~9.5 kW during evening hours, while the (Q_{AC-ref}) for the DFIG is utilized to test reactive power control capabilities, including absorption, generation, and unity power factor.

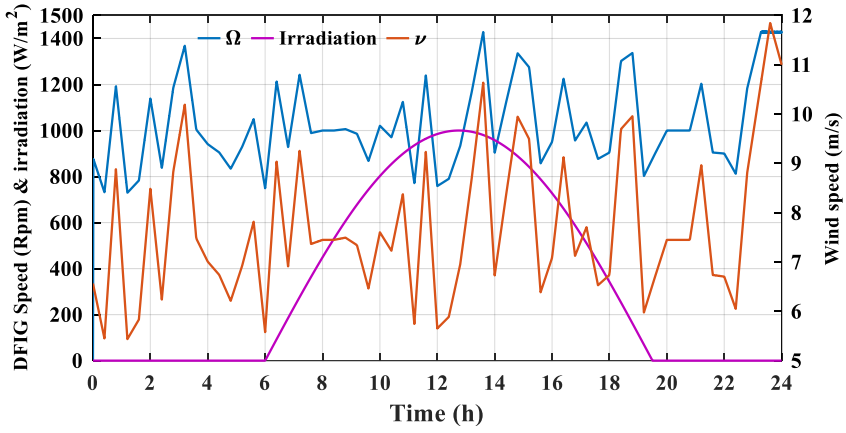

Figure V-9 : Wind and DFIG speed and irradiation.

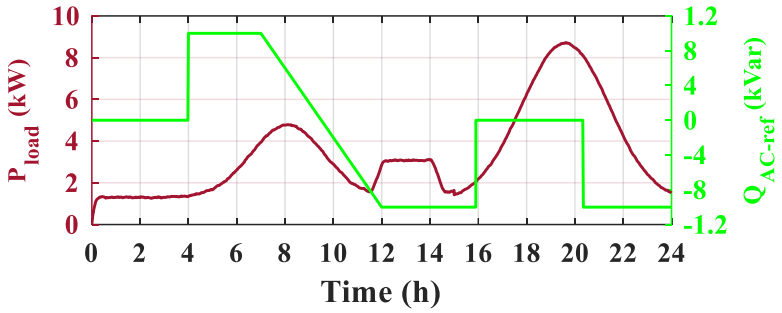

Figure V-10 : DC load power and local reactive power demands.

The aerodynamic performance of the wind turbine is crucial for its energy capture. Figure V-11 details the power coefficient (C_p), tip-speed ratio (λ), and blade pitch angle (β). During wind speeds below the rated value, (β) is consistently held at 0°, allowing (λ) to be regulated around its optimal value 9, thereby maximizing (C_p) to values 0.5. As wind speeds exceed the rated threshold, the pitch control system actively increases (β) to limit the aerodynamic torque and cap the generated power.

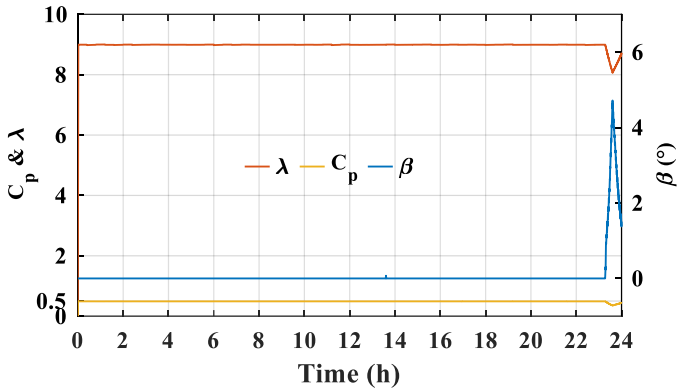

Figure V-11 C_p, λ and β responses.

The active power generated by the WT-DFIG system at the stator terminals (P_s) is shown in Figure V-12. This output closely mirrors the wind energy availability, with the CNN-DPC controlled RSC ensuring efficient power extraction and smooth operation, reaching the system's rated power of 7.5 kW during high wind periods and being appropriately curtailed by pitch control when necessary. The local compensated AC reactive power (Q_{AC}), depicted in Figure V-13, demonstrates excellent tracking of its reference. The DFIG's rotor power (P_r), which is exchanged with the DC bus, is presented in Figure V-14. Its magnitude and direction, positive during super-synchronous operation and negative during sub-synchronous operation are consistent with the DFIG's operational mode and slip.

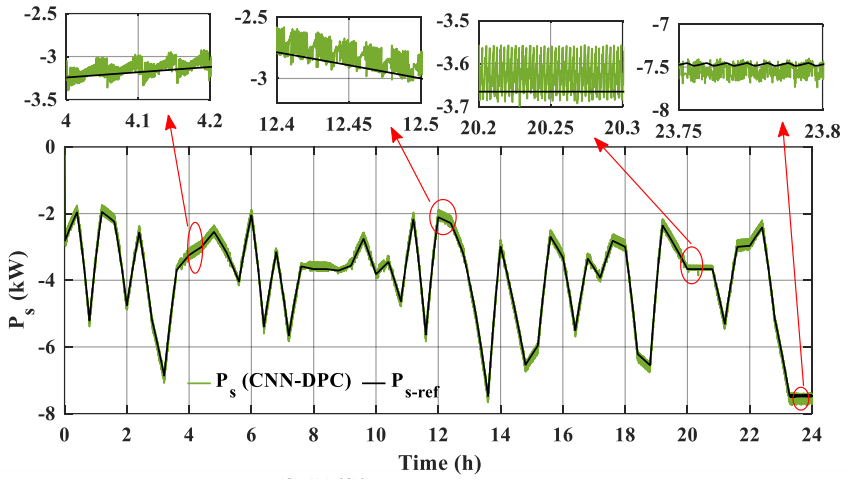

Figure V-12 : Generated power by WT-DFIG.

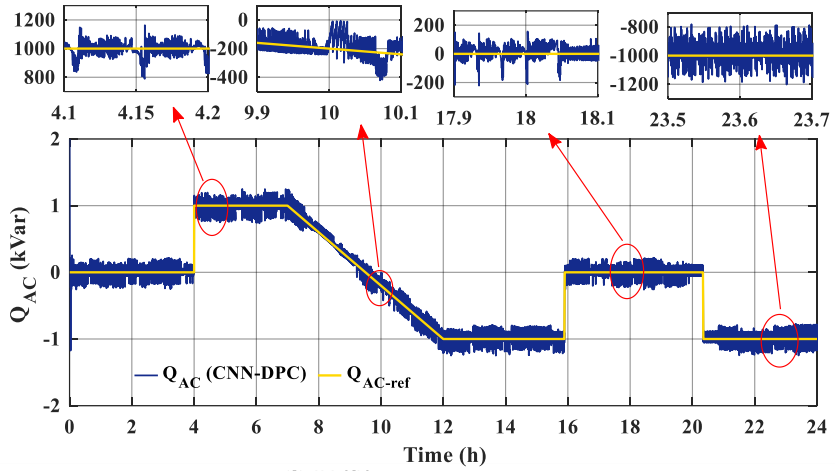

Figure V-13 : Local compensated reactive power.

The contribution from the solar resource is shown in Figure V-15, which displays the power generated by the PV system (P_{PV}). The output power profile accurately follows the diurnal irradiance curve, peaking at approximately 5.5 kW. This performance validates the effectiveness of the Fuzzy-MPPT controller in maximizing energy yield from the PV array. The net available power at the DC microgrid bus (P_{Net}) is illustrated in Figure V-16. This P_{Net} profile shows periods of significant power surplus and deficit, highlighting the dynamic balancing task faced by the EMS.

The Energy Management System coordinates the BESS and FC to address these imbalances. Figure V-17 details the BESS charging and discharging power. The BESS is observed to absorb surplus power, for instance, charging at rates up to 6.5 kW when P_{Net} is high and the SOC is below 80%. Conversely, it discharges to supply the load during deficits, delivering power up to its converter limit if required by the EMS. The Fuel Cell power (P_{FC}) profile is shown in Figure V-18. The FC system is activated by the EMS during prolonged deficits or when the BESS SOC reaches

critical lower levels. The FC is seen to dispatch a consistent 5 kW to support the evening peak load as renewable generation wanes and BESS SOC is low.

The interaction of the DC microgrid with the external AC grid, managed via the DFIG's GSC, is depicted in Figure V-19, showing the active power (P_g) exchanged. This flow is governed by the GSC's Fuzzy-DPC, which primarily ensures the stability of the DFIG's DC link and responds to EMS directives for overall system power balance with the AC grid. For example, the system draws up to 3.5 kW from the grid during severe deficits and exports surplus when all local storage options are saturated. The stability of the DC bus voltage (V_{dc}) itself, along with the BESS terminal voltage (V_{bat}), is critically important and is presented in Figure V-20. Despite the dynamic power exchanges, V_{dc} is maintained its 880 V reference. The BESS voltage, V_{bat}, varies predictably with its SOC. The corresponding BESS State of Charge (SOC) profile is shown in Figure V-21, confirming that the EMS successfully maintains the SOC within the targeted 20% to 80% operational window, thereby ensuring battery health. For instance, the SOC reaches 80% around hour 16 due to high daytime renewable generation and is drawn down to near 20% by hour 20 before renewable generation and grid support facilitate recharging.

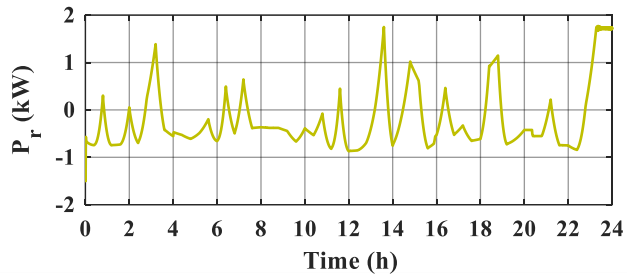

Figure V-14 : Power of DFIG's rotor.

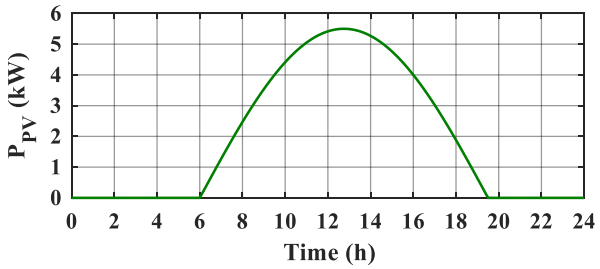

Figure V-15 : PV power.

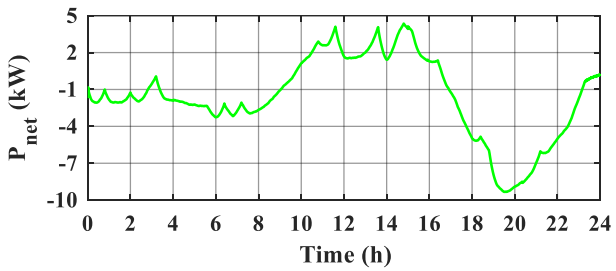

Figure V-16 : Available power at DC-Microgrid.

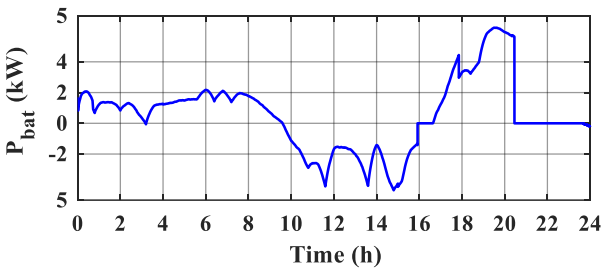

Figure V-17 : Battery power.

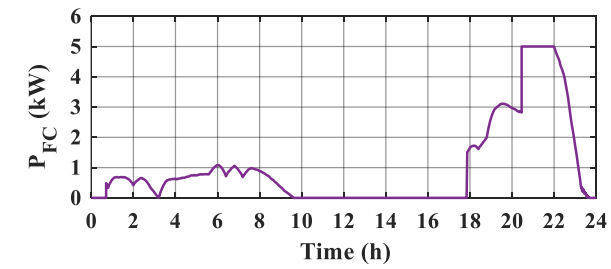

Figure V-18 : Fuel cell power.

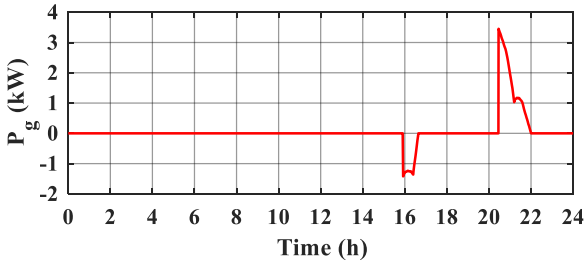

Figure V-19 : Power exchange between the DC-MG and AC grid at GSC.

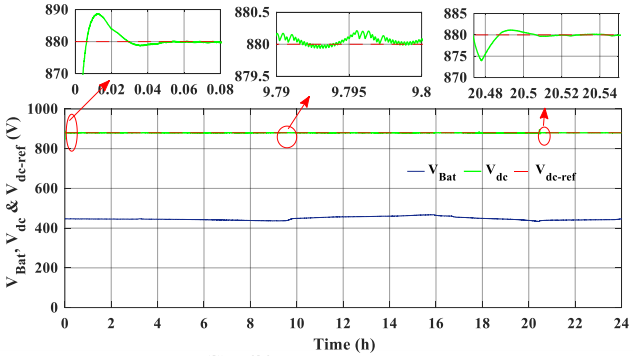

Figure V-20 : Battery and DC bus voltages.

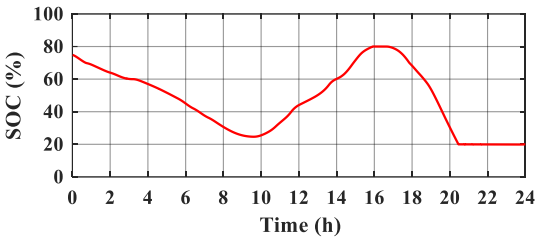

Figure V-21 : State of Charge of battery.

The power quality at the AC grid interface managed by the GSC is a key outcome of the advanced Fuzzy-DPC strategy. The GSC active power (P_g) tracking its reference under Fuzzy-DPC is illustrated in Figure V-22. The tracking is precise, and power ripples are significantly attenuated, a marked improvement over classical DPC. Figure V-23 demonstrates the GSC reactive power (Q_g) effectively tracking its reference, which is typically 0 Var for unity power factor operation at the GSC-grid interface. The Fuzzy-DPC ensures Q_g remains very close to zero with minimal oscillations, confirming excellent reactive power control and contribution to grid power quality. Figure V-24 shows the total active power exchanged with the AC grid.

The collective results presented in strongly validate the performance of the integrated DC-microgrid. The advanced local controllers (CNN-DPC for RSC, Fuzzy-DPC for GSC and PV MPPT) contribute to high efficiency and power quality at the component level. The EMS, through its rule-based logic and SOC management, successfully coordinates these distributed resources and storage element to ensure a reliable and stable power supply to the DC load under highly variable operating conditions, while respecting all predefined operational constraints.

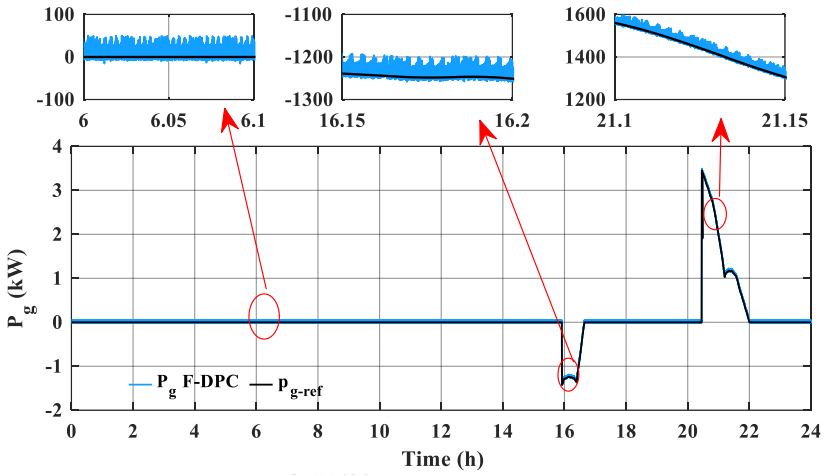

Figure V-22 : P_g with reference using F-DPC.

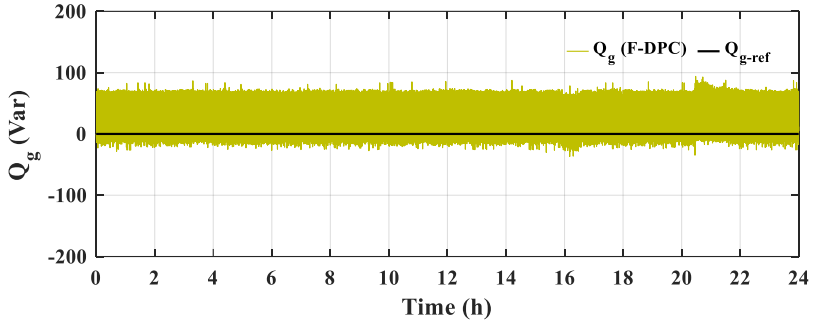

Figure V-23 : Q_g with reference using F-DPC.

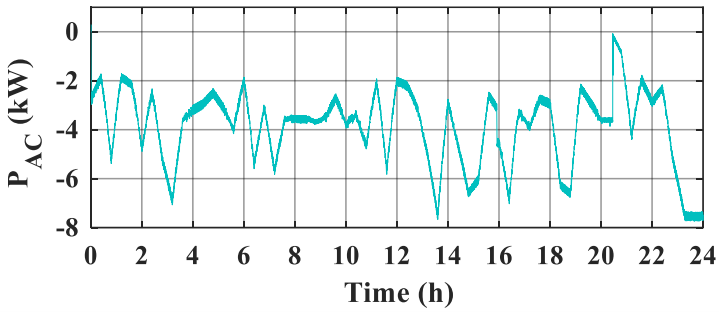

Figure V-24 : AC grid power.

V.7. CONCLUSION

This chapter comprehensively addressed the critical aspects of managing and controlling an integrated DC-microgrid composed of diverse renewable energy sources (WT-DFIG, PV array) and energy storage technologies (BESS), and auxiliary power generation systems (FC). It covered a detailed description and systematic sizing of these components, the implementation and refinement of advanced local control strategies for the key generation units, and the design, validation, and performance analysis of a rule-based Energy Management System (EMS).

Extensive simulation results conducted under realistic and dynamic operating conditions affirmed the viability and effectiveness of the proposed integrated system. Advanced intelligent controllers, including CNN-DPC/Fuzzy-DPC for the DFIG and Fuzzy-MPPT for the PV system, demonstrated robust and superior performance. The DFIG system, under coordinated control, provided high-quality generated active power, and managed local compensated reactive power effectively. The PV system achieved high energy capture efficiency even with fluctuating solar irradiance. Additionally, the GSC's Fuzzy-DPC ensured stable DC-link voltage for the DFIG and managed power exchange with the AC interface efficiently, with significantly reduced power ripples.

The rule-based Energy Management System, incorporating multi-zone SOC-dependent logic with hysteresis for the BESS, proved highly effective in orchestrating complex power flows. It consistently maintained the DC bus voltage around its 880V reference with minimal deviations across all simulated conditions. The BESS SOC was strictly managed within the 20%-80% operational window, safeguarding battery health and ensuring availability for energy buffering. The EMS successfully prioritized power from the WT-DFIG and PV array, resulting in a high renewable energy penetration. The Fuel Cell was carefully dispatched, primarily during critical, prolonged energy deficits, conserving fuel and minimizing operational wear. Overall, the adopted sizing for the WT-DFIG, PV, BESS, and FC components were demonstrated to be adequate for meeting the defined variable DC load profile with significant reliability and autonomy.

While this research demonstrates significant advancements, certain limitations illuminate promising avenues for future investigation. The current rule-based EMS, though effective, could be enhanced by exploring more advanced optimization algorithms (e.g., Model Predictive Control, Reinforcement Learning) for dynamic, adaptive decision-making. A detailed techno-economic analysis, considering various costs and benefits, is crucial for practical viability. Furthermore, experimental validation using Hardware-in-the-Loop (HIL) or laboratory-scale testbeds is an essential next step to verify real-world performance. Future work should also investigate communication latencies and cybersecurity vulnerabilities, expand the system scope to include AC loads and ancillary services, and integrate advanced diagnostics and fault-tolerant control capabilities for enhanced resilience.

This chapter made a notable contribution by presenting a holistically designed, sized, and controlled integrated DC-microgrid. It successfully demonstrated the synergistic integration of advanced AI-based local controllers with an effective, rule-based Energy Management System. The comprehensive simulation results validated the system's ability to achieve high renewable energy

penetration, maintain stringent DC bus voltage regulation, ensure optimal energy storage operation, and deliver high-quality power under dynamic conditions. The findings strongly support the thesis that intelligent control strategies, applied at both component and system levels, are pivotal for unlocking the full potential of complex hybrid renewable energy systems, providing valuable insights for future DC-microgrid design and operation.

GENERAL CONCLUSION AND PERSPECTIVES

This thesis has comprehensively addressed the critical aspects of developing and implementing advanced control algorithms for renewable energy systems, with a particular focus on enhancing the performance of Doubly-Fed Induction Generator (DFIG)-based wind turbines and their effective integration into a DC microgrid also incorporating photovoltaic (PV) generation, battery energy storage (BESS), and a fuel cell (FC) backup system. The research journey began with an exploration of the global imperative for renewable energy and the inherent control challenges (Chapter I), followed by the meticulous mathematical modeling of the diverse microgrid components (Chapter II). A critical evaluation of classical control strategies for DFIGs (Chapter III) highlighted their limitations, primarily excessive power ripple and harmonic distortion, thereby motivating the core research of this work.

Chapter IV represented a significant step forward by developing, implementing, and comparatively evaluating four novel Artificial Intelligence (AI)-based Direct Power Control (DPC) strategies for the DFIG's Rotor Side Converter (RSC). These strategies such as, Fuzzy Hysteresis DPC (FH-DPC), Neural Hysteresis DPC (NH-DPC), Prediction Neural Network DPC (PNN-DPC), and Classification Neural Network DPC (CNN-DPC), all demonstrated substantial improvements in power quality over conventional C-DPC. The CNN-DPC strategy, in particular, was identified as the most promising due to its superior performance in ripple and THD reduction, coupled with an efficient design methodology.

The culmination of this research was presented in Chapter V, which focused on the management and control of the fully integrated DC microgrid. This chapter detailed the application of the selected CNN-DPC for the DFIG-RSC, introduced a Fuzzy Logic-based DPC for the DFIG's Grid Side Converter (GSC), a Fuzzy-MPPT for the PV system, and appropriate controllers for the BESS and FC systems. A systematic sizing methodology for all microgrid components was established, and a comprehensive rule-based Energy Management System (EMS) was designed and validated. Extensive simulations under dynamic environmental conditions and variable load profiles demonstrated the integrated system's robust performance. Key findings from this system-level evaluation include the successful coordination of all energy sources and storage by the EMS, stringent maintenance of the BESS State of Charge within safe operational limits (20%-80%), stable DC bus voltage regulation around its 880V reference, and high renewable energy penetration. The

advanced local controllers, particularly the CNN-DPC for the RSC and Fuzzy-DPC for the GSC, proved effective in delivering high-quality power and ensuring efficient operation of their respective components. The overall adopted sizing for the WT-DFIG, PV, BESS, and FC components were also shown to be adequate for reliably meeting the defined variable DC load profile.

The primary scientific and technical contributions of this thesis can be summarized as:

- ✓ The development and rigorous validation of novel AI-based DPC strategies (FH-DPC, NH-DPC, PNN-DPC, and particularly the superior CNN-DPC) for DFIG Rotor Side Converters, leading to significant enhancements in power quality (reduced power ripples by up to 80% and stator current THD by up to 85%) compared to conventional methods.
- ✓ The design and implementation of intelligent controllers for other key microgrid components, namely a Fuzzy-DPC for the DFIG Grid Side Converter and a Fuzzy-MPPT for the PV system, contributing to improved operational efficiency.
- ✓ The comprehensive design, systematic sizing, and successful simulation of an integrated DC microgrid featuring multiple renewable energy sources (WT-DFIG, PV) and energy storage systems (BESS), and auxiliary power generation systems (FC).
- ✓ The development and validation of an effective rule-based Energy Management System that successfully orchestrates complex power flows within the DC microgrid, ensuring stability, reliability, and optimal utilization of renewable resources.
- ✓ A clear demonstration, through extensive simulation results, of the synergistic benefits of advanced AI-based local control strategies combined with a robust EMS, achieving high renewable energy penetration, stringent DC bus voltage regulation, and the delivery of high-quality power under dynamic operating conditions.

Despite the significant advancements demonstrated, this research has certain limitations which also illuminate promising avenues for future investigation:

- ✓ **Energy Management System Sophistication:** The current rule-based EMS, while effective and transparent, could be enhanced by exploring more advanced optimization algorithms, such as Model Predictive Control (MPC) or Reinforcement Learning. These techniques could offer more dynamic and adaptive decision-making capabilities, potentially leading to further improvements in economic dispatch and operational efficiency.
- ✓ **Techno-Economic Analysis:** A detailed techno-economic analysis, considering capital and operational costs, component lifetime, and potential revenue streams, was beyond the scope of this control-focused thesis but is crucial for assessing the practical viability and market competitiveness of the proposed system.

- ✓ **Experimental Validation:** The findings of this research are based on simulations. Experimental validation using Hardware-in-the-Loop (HIL) platforms or laboratory-scale testbeds is an essential next step to verify real-world performance, controller robustness, and implementation feasibility.
- ✓ **Diagnostics and Fault Tolerance:** Integrating advanced diagnostics and fault-tolerant control capabilities would enhance the resilience and reliability of the microgrid, ensuring continued operation or safe shutdown during component failures or unexpected disturbances.

This thesis has made a notable contribution by presenting a holistically designed, sized, and intelligently controlled integrated DC microgrid. It has successfully demonstrated the synergistic integration of advanced AI-based local controllers with an effective, rule-based Energy Management System. The comprehensive simulation results have validated the system's ability to achieve high renewable energy penetration, maintain stringent DC bus voltage regulation, ensure optimal energy storage operation, and deliver high-quality power under dynamic conditions. The findings strongly support the thesis that intelligent control strategies, applied at both component and system levels, are pivotal for unlocking the full potential of complex hybrid renewable energy systems, providing valuable insights for future DC microgrid design and operation. The continued advancement and application of AI in this domain promise a more efficient, reliable, and sustainable energy future.

REFERENCES

[1] M. Dunford and M. Han, "Energy Dilemmas: Climate Change, Creative Destruction and Inclusive Carbon-Neutral Modernization Path Transitions," International Critical Thought, vol. 15, no. 1, pp. 76-100, 2025, doi: 10.1080/21598282.2025.2448920.

[2] M. M. Vanegas Cantarero, "Of renewable energy, energy democracy, and sustainable development: A roadmap to accelerate the energy transition in developing countries," *Energy Research & Social Science,* vol. 70, 2020, doi: 10.1016/j.erss.2020.101716.

[3] S. D. Ahmed, F. S. M. Al-Ismail, M. Shafiullah, F. A. Al-Sulaiman, and I. M. El-Amin, "Grid Integration Challenges of Wind Energy: A Review," *IEEE Access,* vol. 8, pp. 10857-10878, 2020, doi: 10.1109/access.2020.2964896.

[4] Q. Hassan, S. Algburi, A. Z. Sameen, H. M. Salman, and M. Jaszczur, "A review of hybrid renewable energy systems: Solar and wind-powered solutions: Challenges, opportunities, and policy implications," *Results in Engineering,* vol. 20, 2023, doi: 10.1016/j.rineng.2023.101621.

[5] M. Shafiullah, S. D. Ahmed, and F. A. Al-Sulaiman, "Grid Integration Challenges and Solution Strategies for Solar PV Systems: A Review," *IEEE Access,* vol. 10, pp. 52233-52257, 2022, doi: 10.1109/access.2022.3174555.

[6] A. A. Chhipą *et al.*, "Modeling and Control Strategy of Wind Energy Conversion System with Grid-Connected Doubly-Fed Induction Generator," *Energies,* vol. 15, no. 18, 2022, doi: 10.3390/en15186694.

[7] A. A. B. Mohd Zin, M. Pesaran H.A, A. B. Khairuddin, L. Jahanshaloo, and O. Shariati, "An overview on doubly fed induction generators′ controls and contributions to wind based electricity generation," *Renewable and Sustainable Energy Reviews,* vol. 27, pp. 692-708, 2013, doi: 10.1016/j.rser.2013.07.010.

[8] K. Tamvada and R. Babu, "Control of doubly fed induction generator for power quality improvement: an overview," *International Journal of System Assurance Engineering and Management,* vol. 13, no. 6, pp. 2809-2832, 2022, doi: 10.1007/s13198-022-01754-7.

[9] R. K. Behara and A. K. Saha, "Artificial Intelligence Control System Applied in Smart Grid Integrated Doubly Fed Induction Generator-Based Wind Turbine: A Review," *Energies,* vol. 15, no. 17, 2022, doi: 10.3390/en15176488.

[10] Q. Wang, Y. Li, and R. Li, "Integrating artificial intelligence in energy transition: A comprehensive review," *Energy Strategy Reviews,* vol. 57, 2025, doi: 10.1016/j.esr.2024.101600.

[11] A. W. Adegboyega, S. Sepasi, H. O. R. Howlader, B. Griswold, M. Matsuura, and L. R. Roose, "DC Microgrid Deployments and Challenges: A Comprehensive Review of Academic and Corporate Implementations," *Energies,* vol. 18, no. 5, 2025, doi: 10.3390/en18051064.

[12] S. Ali, Z. Zheng, M. Aillerie, J.-P. Sawicki, M.-C. Péra, and D. Hissel, "A Review of DC Microgrid Energy Management Systems Dedicated to Residential Applications," *Energies,* vol. 14, no. 14, 2021, doi: 10.3390/en14144308.

[13] Energy Institute, "Statistical review of world energy 2024 (73rd ed.)," 2024.

[14] IEA (International Energy Agency), "World Energy Outlook 2024," 2024.

[15] V. Smil, *Energy and civilization: a history*. MIT press, 2017.

[16] A. Cherp and J. Jewell, "The concept of energy security: Beyond the four As," *Energy Policy,* vol. 75, pp. 415-421, 2014, doi: 10.1016/j.enpol.2014.09.005.

[17] NOAA, "Global Monitoring Laboratory-Carbon Cycle Greenhouse Gases," *US Department of Commerce,. https://gml. noaa. gov/ccgg/. Accessed,* vol. 14, 2024.
[18] IPCC (Intergovernmental Panel on Climate Change), "Climate change 2022: Impacts, adaptation and vulnerability," 2022.
[19] World Bank, "Tracking SDG7: The energy progress report 2023," 2023.
[20] IRENA (International Renewable Energy Agency), "Renewable capacity statistics 2024," 2024.
[21] Lazard, "Lazard's levelized cost of energy analysis – Version 17.0," 2024.
[22] REN21, "Renewables 2023 global status report," 2023.
[23] L. Deguenon, D. Yamegueu, S. Moussa kadri, and A. Gomna, "Overcoming the challenges of integrating variable renewable energy to the grid: A comprehensive review of electrochemical battery storage systems," *Journal of Power Sources,* vol. 580, 2023, doi: 10.1016/j.jpowsour.2023.233343.
[24] M. Salehi, M. Khanali, and H. Ghasemi-Mobtaker, "Techno-economic analysis of renewable hybrid system microgrids for minimizing grid power outages in residential areas," *Cleaner Engineering and Technology,* vol. 25, 2025, doi: 10.1016/j.clet.2025.100924.
[25] P. Moore, O. A. Alimi, and A. Abu-Siada, "A Review of System Strength and Inertia in Renewable-Energy-Dominated Grids: Challenges, Sustainability, and Solutions," *Challenges,* vol. 16, no. 1, 2025, doi: 10.3390/challe16010012.
[26] M. A. Basit, S. Dilshad, R. Badar, and S. M. Sami ur Rehman, "Limitations, challenges, and solution approaches in grid-connected renewable energy systems," *International Journal of Energy Research,* vol. 44, no. 6, pp. 4132-4162, 2020, doi: 10.1002/er.5033.
[27] J. V. Ringwood, S. Zhan, and N. Faedo, "Empowering wave energy with control technology: Possibilities and pitfalls," *Annual Reviews in Control,* vol. 55, pp. 18-44, 2023, doi: 10.1016/j.arcontrol.2023.04.004.
[28] J. Bhukya and P. Singh, "Enhancing stability via coordinated control of generators, wind farms, and energy storage: Optimizing system parameters," *Journal of Energy Storage,* vol. 96, 2024, doi: 10.1016/j.est.2024.112513.
[29] D. Chen, X. Lin, and Y. Qiao, "Perspectives for artificial intelligence in sustainable energy systems," *Energy,* vol. 318, 2025, doi: 10.1016/j.energy.2025.134711.
[30] J. Verma, L. Sandys, A. Matthews, and S. Goel, "Readiness of artificial intelligence technology for managing energy demands from renewable sources," *Engineering Applications of Artificial Intelligence,* vol. 135, 2024, doi: 10.1016/j.engappai.2024.108831.
[31] GWEC, "GLOBAL WIND REPORT 2024," 2024.
[32] L. T. C. Montoya, M. Y. Hayyani, M. Issa, A. Ilinca, H. Ibrahim, and M. Rezkallah, "Wind power plant planning and modeling," in *Hybrid renewable energy systems and microgrids*: Elsevier, 2021, pp. 259-312.
[33] A. D. Hansen, "Chapter 8 - Wind turbine technologies," in *Wind Energy Engineering (Second Edition)*, T. M. Letcher Ed.: Academic Press, 2023, pp. 89-98.
[34] I. L. Pioro, M. A. Makarem, and C. O. Zvorykin, "Wind-Energy Utilization and Sustainability," *Encyclopedia of Renewable Energy, Sustainability and the Environment,* p. 211, 2024.
[35] M. Ó. Óskarsdóttir, "A general description and comparison of horizontal axis wind turbines and vertical axis wind turbines," 2014.
[36] Z. Zhao, D. Wang, T. Wang, W. Shen, H. Liu, and M. Chen, "A review: Approaches for aerodynamic performance improvement of lift-type vertical axis wind turbine," *Sustainable Energy Technologies and Assessments,* vol. 49, 2022, doi: 10.1016/j.seta.2021.101789.

[37] B. P. Ganthia, S. K. Barik, and B. Nayak, "Wind turbines in energy conversion system: Types & techniques," in *Renewable energy and future power systems*: Springer, 2021, pp. 199-217.
[38] A. Mansouri, A. El Magri, R. Lajouad, I. El Myasse, E. K. Younes, and F. Giri, "Wind energy based conversion topologies and maximum power point tracking: A comprehensive review and analysis," *E-prime-advances in electrical engineering, electronics and energy,* vol. 6, p. 100351, 2023.
[39] M. A. Hannan *et al.*, "Wind Energy Conversions, Controls, and Applications: A Review for Sustainable Technologies and Directions," *Sustainability,* vol. 15, no. 5, 2023, doi: 10.3390/su15053986.
[40] M. I. Hossain, W. Qarony, S. Ma, L. Zeng, D. Knipp, and Y. H. Tsang, "Perovskite/Silicon Tandem Solar Cells: From Detailed Balance Limit Calculations to Photon Management," *Nanomicro Lett,* vol. 11, no. 1, p. 58, Jul 16 2019, doi: 10.1007/s40820-019-0287-8.
[41] M. A. Green and S. P. Bremner, "Energy conversion approaches and materials for high-efficiency photovoltaics," *Nat Mater,* vol. 16, no. 1, pp. 23-34, Dec 20 2016, doi: 10.1038/nmat4676.
[42] E. Kabalcı, "Review on novel single-phase grid-connected solar inverters: Circuits and control methods," *Solar Energy,* vol. 198, pp. 247-274, 2020, doi: 10.1016/j.solener.2020.01.063.
[43] M. Taguchi, "Review—Development History of High Efficiency Silicon Heterojunction Solar Cell: From Discovery to Practical Use," *ECS Journal of Solid State Science and Technology,* vol. 10, no. 2, 2021, doi: 10.1149/2162-8777/abdfb6.
[44] P. Verlinden *et al.*, "Photovoltaic device innovation for a solar future," *Device,* vol. 1, no. 1, 2023, doi: 10.1016/j.device.2023.100013.
[45] M. Bošnjaković, "Advance of Sustainable Energy Materials: Technology Trends for Silicon-Based Photovoltaic Cells," *Sustainability,* vol. 16, no. 18, 2024, doi: 10.3390/su16187962.
[46] S. A. Kalogirou, "Photovoltaic Systems," in *Solar Energy Engineering*, 2024, pp. 495-557.
[47] M. Y. Ali Khan, H. Liu, Z. Yang, and X. Yuan, "A Comprehensive Review on Grid Connected Photovoltaic Inverters, Their Modulation Techniques, and Control Strategies," *Energies,* vol. 13, no. 16, 2020, doi: 10.3390/en13164185.
[48] D. Michaelson and J. Jiang, "Review of integration of small modular reactors in renewable energy microgrids," *Renewable and Sustainable Energy Reviews,* vol. 152, 2021, doi: 10.1016/j.rser.2021.111638.
[49] M. B. Hossain, M. R. Islam, K. M. Muttaqi, D. Sutanto, and A. P. Agalgaonkar, "Advancement of fuel cells and electrolyzers technologies and their applications to renewable-rich power grids," *Journal of Energy Storage,* vol. 62, 2023, doi: 10.1016/j.est.2023.106842.
[50] N. A. A. Qasem, G. A. Q. Abdulrahman, and D. Osinkin, "A Recent Comprehensive Review of Fuel Cells: History, Types, and Applications," *International Journal of Energy Research,* vol. 2024, no. 1, 2024, doi: 10.1155/2024/7271748.
[51] S. Dwivedi, "Solid oxide fuel cell: Materials for anode, cathode and electrolyte," *International Journal of Hydrogen Energy,* vol. 45, no. 44, pp. 23988-24013, 2020, doi: 10.1016/j.ijhydene.2019.11.234.
[52] A. H. Fathima and K. Palanisamy, "Energy Storage Systems for Energy Management of Renewables in Distributed Generation Systems," in *Energy Management of Distributed Generation Systems*, 2016, ch. Chapter 7.
[53] T. Chen *et al.*, "Applications of Lithium-Ion Batteries in Grid-Scale Energy Storage Systems," *Transactions of Tianjin University,* vol. 26, no. 3, pp. 208-217, 2020, doi: 10.1007/s12209-020-00236-w.

[54] X. Gao *et al.*, "Comprehensive insights into solid-state electrolytes and electrode-electrolyte interfaces in all-solid-state sodium-ion batteries," *Energy Storage Materials,* vol. 60, 2023, doi: 10.1016/j.ensm.2023.102821.

[55] M. A. Hannan *et al.*, "Battery energy-storage system: A review of technologies, optimization objectives, constraints, approaches, and outstanding issues," *Journal of Energy Storage,* vol. 42, 2021, doi: 10.1016/j.est.2021.103023.

[56] M. Melikoglu, "Pumped hydroelectric energy storage: Analysing global development and assessing potential applications in Turkey based on Vision 2023 hydroelectricity wind and solar energy targets," *Renewable and Sustainable Energy Reviews,* vol. 72, pp. 146-153, 2017, doi: 10.1016/j.rser.2017.01.060.

[57] X. Li and A. Palazzolo, "A review of flywheel energy storage systems: state of the art and opportunities," *Journal of Energy Storage,* vol. 46, 2022, doi: 10.1016/j.est.2021.103576.

[58] F. Naseri, S. Karimi, E. Farjah, and E. Schaltz, "Supercapacitor management system: A comprehensive review of modeling, estimation, balancing, and protection techniques," *Renewable and Sustainable Energy Reviews,* vol. 155, 2022, doi: 10.1016/j.rser.2021.111913.

[59] A. Boudia, S. Messalti, A. Harrag, and M. Boukhnifer, "New hybrid photovoltaic system connected to superconducting magnetic energy storage controlled by PID-fuzzy controller," *Energy Conversion and Management,* vol. 244, 2021, doi: 10.1016/j.enconman.2021.114435.

[60] O. Djoudi, "Contrôle d'une machine asynchrone à double alimentation connectée à un micro réseau et dédiée aux énergies renouvelables," Ph.D, Université A.MIRA-BEJAIA, 2024.

[61] Y. Sahri, "Contribution à la commande non linéaire et à la gestion d'énergie d'un système hybride d'énergies renouvelables," Ph.D, Université A.MIRA-BEJAIA, 2022.

[62] S. Tamalouzt, "Contribution à l'étude, conception et la commande des convertisseurs électromagnetiques double alimentés," Ph.D, Université A.MIRA-BEJAIA, 2017.

[63] K. F. Sayeh, S. Tamalouzt, D. Ziane, Y. Sahri, B. Deffaf, and S. Lalouni Belaid, "Control of a Wind Turbine based on DFIG by Improved Direct Torque Control using Fuzzy Logic," *Journal of Renewable Energies,* 2024, doi: 10.54966/jreen.v1i1.1173.

[64] K. F. Sayeh, S. Tamalouzt, and Y. Sahri, "Improvement of power quality in WT-DFIG systems using novel direct power control based on fuzzy logic control under randomness conditions," *International Journal of Modelling and Simulation,* vol. 45, no. 1, pp. 55-67, 2023, doi: 10.1080/02286203.2023.2270757.

[65] K. F. Sayeh, S. Tamalouzt, D. Ziane, A. Bekhiti, Y. Belkhier, and S. O. Oyedepo, "Utilizing Fuzzy Logic Control and Neural Networks Based on Artificial Intelligence Techniques to Improve Power Quality in Doubly Fed Induction Generator-Based Wind Turbine System," *International Journal of Energy Research,* vol. 2025, no. 1, 2025, doi: 10.1155/er/5985904.

[66] K. F. Sayeh, S. Tamalouzt, Y. Sahri, S. Lalouni Belaid, and A. Bekhiti, "Artificial intelligence-based direct power control for power quality improvement in a WT-DFIG system via neural networks: Prediction and classification techniques," *Journal of the Franklin Institute,* vol. 362, no. 1, 2025, doi: 10.1016/j.jfranklin.2024.107401.

[67] K. F. sayeh *et al.*, "Fuzzy Logic-Enhanced Direct Power Control for Wind Turbines with Doubly Fed Induction Generators," *Results in Engineering,* vol. 24, 2024, doi: 10.1016/j.rineng.2024.103557.

[68] S. Kassir, "An Integrated Smart Energy Management and Model-Free Control Approaches for Islanded Residential Microgrids," Ph.D, Nantes Université; Université Libanaise, 2023.

[69] F. Shahnia, "Microgrids and their control," in *Hybrid Renewable Energy Systems and Microgrids*: Elsevier, 2021, pp. 399-462.

[70] K. Cabana-Jiménez, J. E. Candelo-Becerra, and V. Sousa Santos, "Comprehensive Analysis of Microgrids Configurations and Topologies," *Sustainability,* vol. 14, no. 3, 2022, doi: 10.3390/su14031056.

[71] M. Abbasi, E. Abbasi, L. Li, R. P. Aguilera, D. Lu, and F. Wang, "Review on the Microgrid Concept, Structures, Components, Communication Systems, and Control Methods," *Energies,* vol. 16, no. 1, 2023, doi: 10.3390/en16010484.

[72] M. Rezkallah, A. Chandra, B. Singh, and S. Singh, "Microgrid: Configurations, Control and Applications," *IEEE Transactions on Smart Grid,* vol. 10, no. 2, pp. 1290-1302, 2019, doi: 10.1109/tsg.2017.2762349.

[73] M. Ahmed, L. Meegahapola, A. Vahidnia, and M. Datta, "Stability and Control Aspects of Microgrid Architectures–A Comprehensive Review," *IEEE Access,* vol. 8, pp. 144730-144766, 2020, doi: 10.1109/access.2020.3014977.

[74] S. M. Hashemi and V. Vahidinasab, "Energy Management Systems for Microgrids," in *Microgrids*, (Power Systems, 2021, ch. Chapter 3, pp. 61-95.

[75] D. Kumar, F. Zare, and A. Ghosh, "DC Microgrid Technology: System Architectures, AC Grid Interfaces, Grounding Schemes, Power Quality, Communication Networks, Applications, and Standardizations Aspects," *IEEE Access,* vol. 5, pp. 12230-12256, 2017, doi: 10.1109/access.2017.2705914.

[76] B. Modu, M. P. Abdullah, M. A. Sanusi, and M. F. Hamza, "DC-based microgrid: Topologies, control schemes, and implementations," *Alexandria Engineering Journal,* vol. 70, pp. 61-92, 2023, doi: 10.1016/j.aej.2023.02.021.

[77] W. Dwiono, B. R. Trilaksono, T. D. Rachmildha, and A. Rizqiawan, "Enhancing the Dynamic Performance of Hybrid Photovoltaic-Battery DC Microgrid Through Piece-Wise Affine Model-Based Controller With Mode Transition Function," *IEEE Access,* vol. 12, pp. 169910-169927, 2024, doi: 10.1109/access.2024.3476624.

[78] A. Kavousighahfarokhi *et al.*, "Advancing voltage control in DC microgrids: a comparative study with IGWO-based H∞ control," *International Journal of Dynamics and Control,* vol. 12, no. 9, pp. 3339-3353, 2024, doi: 10.1007/s40435-024-01428-1.

[79] N. Ali, X. Shen, H. Armghan, and Y. Du, "Hierarchical control combined with higher order sliding mode control for integrating wind/tidal/battery/hydrogen powered DC offshore microgrid," *Journal of Energy Storage,* vol. 82, 2024, doi: 10.1016/j.est.2024.110521.

[80] Z. Zhu, X. Liu, X. Kong, L. Ma, K. Y. Lee, and Y. Xu, "PV/Hydrogen DC microgrid control using distributed economic model predictive control," *Renewable Energy,* vol. 222, 2024, doi: 10.1016/j.renene.2023.119871.

[81] S. K. Ramu, I. Vairavasundaram, B. Palaniyappan, A. Bragadeshwaran, and B. Aljafari, "Enhanced energy management of DC microgrid: Artificial neural networks-driven hybrid energy storage system with integration of bidirectional DC-DC converter," *Journal of Energy Storage,* vol. 88, 2024, doi: 10.1016/j.est.2024.111562.

[82] P. K. Behera and M. Pattnaik, "Design and real-time implementation of wind–photovoltaic driven low voltage direct current microgrid integrated with hybrid energy storage system," *Journal of Power Sources,* vol. 595, 2024, doi: 10.1016/j.jpowsour.2023.234028.

[83] A. G. Alharbi, A. G. Olabi, H. Rezk, A. Fathy, and M. A. Abdelkareem, "Optimized energy management and control strategy of photovoltaic/PEM fuel cell/batteries/supercapacitors DC microgrid system," *Energy,* vol. 290, 2024, doi: 10.1016/j.energy.2023.130121.

[84] Y. Sahri *et al.*, "Performance improvement of Hybrid System based DFIG-Wind/PV/Batteries connected to DC and AC grid by applying Intelligent Control," *Energy Reports,* vol. 9, pp. 2027-2043, 2023, doi: 10.1016/j.egyr.2023.01.021.

[85] S. Tamalouzt, N. Benyahia, T. Rekioua, D. Rekioua, and R. Abdessemed, "Performances analysis of WT-DFIG with PV and fuel cell hybrid power sources system associated with

hydrogen storage hybrid energy system," *International Journal of Hydrogen Energy,* vol. 41, no. 45, pp. 21006-21021, 2016, doi: 10.1016/j.ijhydene.2016.06.163.

[86] I. Kazi Shariful, "Stability and control of wind energy integrated power systems," Swinburne University of Technology, 2019.

[87] A. Petersson, "Analysis, Modeling and Control of Doubly-Fed Induction Generators for Wind Turbines," Chalmers University of Technology, 2005.

[88] A. K. El-Naggar, "Advanced Modeling and Analysis of the Doubly-Fed Induction Generator Based Wind Turbines," The University of Duisburg-Essen, 2017.

[89] A. Pant, "Modelling and Design of Grid Connected Doubly Fed Induction Generator," Texas Tech University 2020.

[90] L. L. Jiang, "Modeling and optimization of photovoltaic systems under partially shaded and rapidly changing conditions," Nanyang Technological University, 2014.

[91] S. Bouacha, "A Study on Photovoltaic Power Plant Connected to the Distribution Network," École Nationale Polytechnique 2021.

[92] S. Lavety, R. K. Keshri, and M. A. Chaudhari, "A dynamic battery model and parameter extraction for discharge behavior of a valve regulated lead-acid battery," *Journal of Energy Storage,* vol. 33, 2021, doi: 10.1016/j.est.2020.102031.

[93] M. Bašić, D. Vukadinović, V. Višnjić, and I. Rakić, "Dynamic Equivalent Circuit Models of Lead-Acid Batteries – A Performance Comparison," *IFAC-PapersOnLine,* vol. 55, no. 4, pp. 189-194, 2022, doi: 10.1016/j.ifacol.2022.06.031.

[94] N. Attik, "Contribution to the modeling and control of renewable energy systems, application to a hybrid PV/wind/storage system," UNIVERSITY FERHAT ABBAS SETIF -1-, 2023.

[95] Y. Qi, "Modelling and controlling of polymer electrolyte fuel cell systems," Lund University, 2021.

[96] A. Adjati, "Etude des machines asynchrones à double étoile en pompage hybride à énergies renouvelables," Uinversity of bejaia, 2022.

[97] M. Blal, A. Benatiallah, A. NeÇaibia, S. Lachtar, N. Sahouane, and A. Belasri, "Contribution and investigation to compare models parameters of (PEMFC), comprehensives review of fuel cell models and their degradation," *Energy,* vol. 168, pp. 182-199, 2019, doi: 10.1016/j.energy.2018.11.095.

[98] S. Tamalouzt, K. Idjdarene, T. Rekioua, and R. Abdessemed, "Direct torque control of wind turbine driven doubly fed induction generator," *Rev. Roum. Sci. Techn.– Électrotechn. et Énerg,* vol. 61, no. 3, p. 244, 2016.

[99] S. Tamalouzt, T. Rekioua, and R. Abdessemed, "Direct torque and reactive power control of grid connected doubly fed induction generator for the wind energy conversion," in *2014 International conference on electrical sciences and technologies in Maghreb (CISTEM)*, 2014: IEEE, pp. 1-7.

[100] J. Pande, P. Nasikkar, K. Kotecha, and V. Varadarajan, "A Review of Maximum Power Point Tracking Algorithms for Wind Energy Conversion Systems," *Journal of Marine Science and Engineering,* vol. 9, no. 11, 2021, doi: 10.3390/jmse9111187.

[101] G. Rashmi and M. M. Linda, "A novel MPPT design for a wind energy conversion system using grey wolf optimization," *Automatika,* vol. 64, no. 4, pp. 798-806, 2023, doi: 10.1080/00051144.2023.2218168.

[102] Y. Sahri, S. Tamalouzt, and S. Belaid Lalouni, "Enhanced Direct Power Control Strategy of a DFIG-Based Wind Energy Conversion System Operating Under Random Conditions," *Periodica Polytechnica Electrical Engineering and Computer Science,* vol. 65, no. 3, pp. 196-206, 2021, doi: 10.3311/PPee.16656.

[103] L. Xu and P. Cartwright, "Direct Active and Reactive Power Control of DFIG for Wind Energy Generation," *IEEE Transactions on Energy Conversion,* vol. 21, no. 3, pp. 750-758, 2006, doi: 10.1109/tec.2006.875472.
[104] F. Mazouz, S. Belkacem, I. Colak, S. Drid, and Y. Harbouche, "Adaptive direct power control for double fed induction generator used in wind turbine," *International Journal of Electrical Power & Energy Systems,* vol. 114, 2020, doi: 10.1016/j.ijepes.2019.105395.
[105] A. Bouafia, "Techniques de commande predictive et floue pour les systemes d'electronique de puissance: application aux redresseurs a mli," Universite de setif, 2010.
[106] H. Benbouhenni, "A 24-sectors direct power control-feedforward neural network method of DFIG integrated to dual-rotor wind turbine," *International Journal of Applied Power Engineering (IJAPE),* vol. 10, no. 4, 2021, doi: 10.11591/ijape.v10.i4.pp291-306.
[107] I. Yaichi, A. Semmah, and P. Wira, "Neuro-second order sliding mode control of a DFIG based wind turbine system," *Journal of Electrical and Electronics Engineering,* vol. 13, no. 1, pp. 63-68, 2020.
[108] S. Massoum, A. Meroufel, A. Massoum, and P. Wira, "A direct power control of the doubly-fed induction generator based on the SVM strategy," *Elektrotehniski Vestnik,* vol. 84, no. 5, pp. 235-240, 2017.
[109] S. K. Sahoo, "Comparison of SVM and DPC for reactive power control of DFIG based wind energy systems," *Journal of Renewable Energy and Smart Grid Technology,* vol. 11, no. 1, pp. 1-8, 2016.
[110] M. Verij Kazemi, A. Sadeghi Yazdankhah, and H. Madadi Kojabadi, "Direct power control of DFIG based on discrete space vector modulation," *Renewable Energy,* vol. 35, no. 5, pp. 1033-1042, 2010, doi: 10.1016/j.renene.2009.09.008.
[111] I. Yaichi, A. Semmah, P. Wira, and S. M. El-Amine, "An improved direct power control based on SVM strategy of the doubly fed induction generator," in *2019 7th International Renewable and Sustainable Energy Conference (IRSEC)*, 2019: IEEE, pp. 1-8.
[112] D. Zhi and L. Xu, "Direct Power Control of DFIG With Constant Switching Frequency and Improved Transient Performance," *IEEE Transactions on Energy Conversion,* vol. 22, no. 1, pp. 110-118, 2007, doi: 10.1109/tec.2006.889549.
[113] A. A. Z. Diab, "Model predictive direct power control of rotor side converter for DFIGs driven by variable speed wind turbines," in *2018 25th International Workshop on Electric Drives: Optimization in Control of Electric Drives (IWED)*, 2018: IEEE, pp. 1-6.
[114] F. S. Guedes, N. Rocha, A. M. Maciel, and A. J. Sguarezi Filho, "A Simple and Powerful Model Predictive Direct Power Control for DFIG," presented at the 2021 Brazilian Power Electronics Conference (COBEP), 2021.
[115] N. Kalamian, M. Verij Kazemi, and S. A. Gholomian, "Direct Power Control of Dfig by Using Nonlinear Model Predictive Controller," *Asian Journal of Control,* vol. 18, no. 3, pp. 985-999, 2016, doi: 10.1002/asjc.1170.
[116] X. Yang, G. Liu, A. Li, and L. V. Dai, "A Predictive Power Control Strategy for DFIGs Based on a Wind Energy Converter System," *Energies,* vol. 10, no. 8, 2017, doi: 10.3390/en10081098.
[117] A. Benzouaoui, H. Khouidmi, and B. Bessedik, "Parallel model predictive direct power control of DFIG for wind energy conversion," *International Journal of Electrical Power & Energy Systems,* vol. 125, 2021, doi: 10.1016/j.ijepes.2020.106453.
[118] Z. Di, W. Yanjun, Z. Jinlong, and Q. Hanhong, "A Novel Predictive Direct Power Control of Doubly Fed Induction Generator based on ADRC method," in *2019 22nd International Conference on Electrical Machines and Systems (ICEMS)*, 2019: IEEE, pp. 1-4.

[119] A. Daoud and N. Derbel, "Direct power control of DFIG using sliding mode control approach," *Modeling, Identification and Control Methods in Renewable Energy Systems,* pp. 193-204, 2019.
[120] Y. Djeriri, P. Wira, A. Semmah, and I. Yaichi, "Super-twisting Sliding Mode Control of a Doubly-fed Induction Generator Based on the SVM Strategy," *Periodica Polytechnica Electrical Engineering and Computer Science,* vol. 63, no. 3, pp. 178-190, 2019, doi: 10.3311/PPee.13726.
[121] H. Lhachimi, Y. Sayouti, and Y. El Kouari, "Optimal improvement of direct power control strategy based on sliding mode controllers," *Computers & Electrical Engineering,* vol. 71, pp. 637-656, 2018, doi: 10.1016/j.compeleceng.2018.08.013.
[122] M. Mazen Alhato, S. Bouallègue, and H. Rezk, "Modeling and Performance Improvement of Direct Power Control of Doubly-Fed Induction Generator Based Wind Turbine through Second-Order Sliding Mode Control Approach," *Mathematics,* vol. 8, no. 11, 2020, doi: 10.3390/math8112012.
[123] R. Sadeghi, S. M. Madani, M. Ataei, M. R. Agha Kashkooli, and S. Ademi, "Super-Twisting Sliding Mode Direct Power Control of a Brushless Doubly Fed Induction Generator," *IEEE Transactions on Industrial Electronics,* vol. 65, no. 11, pp. 9147-9156, 2018, doi: 10.1109/tie.2018.2818672.
[124] A. Shah and A. Mehta, "Sliding Mode Direct Power Control of a Grid-Connected DFIG Using an Extended State Observer," *Emerging Trends in Sliding Mode Control: Theory and Application,* pp. 325-349, 2021.
[125] F. Mazouz, S. Belkacem, and G. Boukhalfa, "Second Order Sliding Mode Control Based DPC of DFIG Using SVM," in *Artificial Intelligence and Heuristics for Smart Energy Efficiency in Smart Cities*, (Lecture Notes in Networks and Systems, 2022, ch. Chapter 75, pp. 743-750.
[126] F. Mazouz, S. Belkacem, G. Boukhalfa, and I. Colak, "Backstepping Approach Based on Direct Power Control of a DFIG in WECS," presented at the 2021 10th International Conference on Renewable Energy Research and Application (ICRERA), 2021.
[127] S. Mensou, A. Essadki, T. Nasser, and B. Bououlid Idrissi, "A direct power control of a DFIG based-WECS during symmetrical voltage dips," *Protection and Control of Modern Power Systems,* vol. 5, no. 1, 2020, doi: 10.1186/s41601-019-0148-y.
[128] A. Mehdi, A. Reama, H. E. Medouce, S. E. Rezgui, and H. Benalla, "Direct active and reactive power control of DFIG based wind energy conversion system," in *2014 International Symposium on Power Electronics, Electrical Drives, Automation and Motion*, 2014: IEEE, pp. 1128-1133.
[129] M. Verij Kazemi, M. Moradi, and R. Verij Kazemi, "Minimization of powers ripple of direct power controlled DFIG by fuzzy controller and improved discrete space vector modulation," *Electric Power Systems Research,* vol. 89, pp. 23-30, 2012, doi: 10.1016/j.epsr.2012.02.008.
[130] M. Verij Kazemi, P. Norio Takahashi, M. Moradi, and R. Verij Kazemi, "Fuzzy logic control to improve the performance of the direct power control based DFIG," *COMPEL: The International Journal for Computation and Mathematics in Electrical and Electronic Engineering,* vol. 33, no. 1/2, pp. 254-272, 2013, doi: 10.1108/compel-08-2012-0131.
[131] H. Z. Boroujeni, M. F. Othman, A. H. Shirdel, R. Rahmani, P. Movahedi, and E. S. Toosi, "Improving waveform quality in direct power control of DFIG using fuzzy controller," *Neural Computing and Applications,* vol. 26, no. 4, pp. 949-955, 2014, doi: 10.1007/s00521-014-1725-7.
[132] M. Pichan, H. Rastegar, and M. Monfared, "Two fuzzy-based direct power control strategies for doubly-fed induction generators in wind energy conversion systems," *Energy,* vol. 51, pp. 154-162, 2013, doi: 10.1016/j.energy.2012.12.047.

[133] E. Heydari, M. Rafiee, and M. Pichan, "Fuzzy-genetic algorithm-based direct power control strategy for DFIG," *Iranian Journal of Electrical and Electronic Engineering,* vol. 14, no. 4, pp. 353-361, 2018.
[134] S. Khateri-Abri, S. Tohidi, and N. Rostami, "Improved Direct Power Control of DFIG Wind Turbine by using a Fuzzy Logic Controller," in *2019 10th International Power Electronics, Drive Systems and Technologies Conference (PEDSTC)*, 2019: IEEE, pp. 458-463.
[135] S. Tamalouzt, "Performances of direct reactive power control technique applied to three level-inverter under random behavior of wind speed," *Rev. Roum. Sci. Techn.–Électrotechn. et Énerg,* vol. 64, no. 1, pp. 33-38, 2019.
[136] S. Tamalouzt *et al.*, "Enhanced Direct Reactive Power Control-Based Multi-Level Inverter for DFIG Wind System under Variable Speeds," *Sustainability,* vol. 13, no. 16, 2021, doi: 10.3390/su13169060.
[137] H. Benbouhenni, "Application of five-level NPC inverter in DPC-ANN of doubly fed induction generator for wind power generation systems," *International Journal of Smart Grid,* vol. 3, no. 3, pp. 128-137, 2019.
[138] H. Benbouhenni, Z. Boudjema, and A. Belaidi, "Power Control of DFIG in WECS Using DPC and NDPC-NPWM Methods," *Mathematical Modelling of Engineering Problems,* vol. 7, no. 2, pp. 223-236, 2020, doi: 10.18280/mmep.070208.
[139] R. A. de Marchi, P. S. Dainez, F. J. Von Zuben, and E. Bim, "A Multilayer Perceptron Controller Applied to the Direct Power Control of a Doubly Fed Induction Generator," *IEEE Transactions on Sustainable Energy,* vol. 5, no. 2, pp. 498-506, 2014, doi: 10.1109/tste.2013.2293621.
[140] B. Habib, "Robust Direct Power Control of a DFIG Fed by a Five- Level NPC Inverter Using Neural SVPWM Technique," *Tecnica Italiana-Italian Journal of Engineering Science,* vol. 65, no. 1, pp. 119-128, 2021, doi: 10.18280/ti-ijes.650118.
[141] H. Benbouhenni, A. Belaidi, and Z. Boudjema, "Sensorless twelve sectors implementation of neural DPC controlled DFIG for reactive and active powers ripples reduction," *Majlesi Journal of Energy Management,* vol. 7, no. 2, pp. 13-21, 2018.
[142] R. Andreoli de Marchi, P. Sergio Dainez, F. J. Von Zuben, and E. Bim, "A Neural Network Controller For The Direct Power Control Of Doubly Fed Induction Generator," *Eletrônica de Potência,* vol. 18, no. 3, pp. 1038-1046, 2013, doi: 10.18618/rep.2013.3.10381046.
[143] H. Benbouhenni, Z. Boudjema, and A. Belaidi, "Direct power control with NSTSM algorithm for DFIG using SVPWM technique," *Iranian Journal of Electrical & Electronic Engineering,* vol. 17, no. 1, pp. 1-11, 2021.
[144] Y. Sahri *et al.*, "New intelligent direct power control of DFIG-based wind conversion system by using machine learning under variations of all operating and compensation modes," *Energy Reports,* vol. 7, pp. 6394-6412, 2021.
[145] Z. Janková, P. Dostál, and M. Yazdi, "Type-2 Fuzzy Expert System Approach for Decision-Making of Financial Assets and Investing under Different Uncertainty," *Mathematical Problems in Engineering,* vol. 2021, pp. 1-16, 2021, doi: 10.1155/2021/3839071.
[146] *Fuzzy Logic* (Studies in Fuzziness and Soft Computing). 2015.
[147] D. Cai, W. Wu, M. Cescon, W. Liu, L. Ji, and D. Shi, "Data-enabled learning and control algorithms for intelligent glucose management: The state of the art," *Annual Reviews in Control,* vol. 56, 2023, doi: 10.1016/j.arcontrol.2023.100897.
[148] I. Yaichi, A. Semmah, and P. Wira, "Control of Doubly Fed Induction Generator Using Artificial Neural Network Controller," *Revue Roumaine Des Sciences Techniques — SÉrie Électrotechnique Et ÉnergÉtique,* vol. 68, no. 1, pp. 46-51, 2023, doi: 10.59277/rrst-ee.2023.68.1.8.

[149] S. A. Zaid *et al.*, "From MPC-Based to End-to-End (E2E) Learning-Based Control Policy for Grid-Tied 3L-NPC Transformerless Inverter," *IEEE Access,* vol. 10, pp. 57309-57326, 2022, doi: 10.1109/access.2022.3173752.

[150] H. T. El-madany, F. H. Fahmy, N. M. A. El-Rahman, and H. T. Dorrah, "Spacecraft power system controller based on neural network," *Acta Astronautica,* vol. 69, no. 7-8, pp. 650-657, 2011, doi: 10.1016/j.actaastro.2011.05.028.

[151] A. Bakeer, I. S. Mohamed, P. B. Malidarreh, I. Hattabi, and L. Liu, "An Artificial Neural Network-Based Model Predictive Control for Three-Phase Flying Capacitor Multilevel Inverter," *IEEE Access,* vol. 10, pp. 70305-70316, 2022, doi: 10.1109/access.2022.3187996.

[152] H. Bounechba, A. Bouzid, K. Nabti, and H. Benalla, "Comparison of Perturb & Observe and Fuzzy Logic in Maximum Power Point Tracker for PV Systems," *Energy Procedia,* vol. 50, pp. 677-684, 2014, doi: 10.1016/j.egypro.2014.06.083.

[153] H. Rezk, R. M. Ghoniem, S. Ferahtia, A. Fathy, M. M. Ghoniem, and R. Alkanhel, "A Comparison of Different Renewable-Based DC Microgrid Energy Management Strategies for Commercial Buildings Applications," *Sustainability,* vol. 14, no. 24, 2022, doi: 10.3390/su142416656.

APPENDIX

The system and simulation parameters are given in the tables below [61, 62, 85].

Table A.1: Wind Turbine Parameters

Parameter	Value
Rated power P_n	7.5 kW
Rated speed Ω_n	296 rpm
Blade radius R_t	3.24 m
Gear ratio G	5.065

Table A.2: DFIG Parameters

Parameter	Value
Rated power P_n	7.5 kW
Rated speed Ω_n	970 rpm
Voltage U_m	440 V
Number of pole pairs P	3
Stator resistance R_s	1.02 Ω
Rotor resistance R_r	0.8 Ω
Stator inductance L_s	0.093 H
Rotor inductance L_r	0.081 H
Mutual inductance M	0.0664 H

Table A.3: PV Module Parameters (SIEMENS SM 110-24)

Parameter	Value
Maximum power P_{mpp}	110 W
Current at max power point I_{mpp}	3.15 A
Voltage at max power point V_{mpp}	35 V
Short-circuit current I_{sc}	3.45 A
Open-circuit voltage V_{oc}	43.5 V
Current temp. coefficient α_{sc}	1.4 mA/°C
Voltage temp. coefficient β_{oc}	-152 mV/°C
Total number of panels	50

Table A.4: Battery model parameters.

Parameter	Value
Single battery voltage U_{batt}	12 V
Single battery capacity C_{batt}	56 Ah
Total number of batteries	35

Table A.5: PEMFC system model parameters

Parameter	Value
Number of cells N_s	48
Operating temperature T	5-35 °C
Fuel cell power P_{FC}	500 W
Rated current I_{FC}	20 A
Standard reference potential E_0	1.229 V
Faraday's constant F	96,487 C·mol^{-1}
Entropy change ΔS^0	164.03 J·mol^{-1}·K^{-1}
Gas constant R	8.3143 J·mol^{-1}·K^{-1}
Tafel equation constant a	-0.1373 V·K^{-1}
Tafel equation constant b	$1.93 \cdot 10^{-4}$ V·A^{-1}·K^{-1}
Membrane equivalent contact resistance R_C	0.0003 Ω
Activation overvoltage constant η_0	20.145 V
Equivalent capacitance C	3 F
Adjustable parameter b_0	23

Abstract

The global shift to renewable energy, particularly wind power via Doubly-Fed Induction Generators (DFIGs), is hindered by power quality challenges inherent in classical control methods like Conventional Direct Power Control (C-DPC), which exhibit significant power ripple and high harmonic distortion. This thesis addresses these issues by developing and validating novel Artificial Intelligence (AI)-based control strategies for DFIGs and their integration into a comprehensive DC microgrid. Main objectives included modeling microgrid components (WT-DFIG, PV, BESS, FC), critically assessing classical DFIG control, and designing four distinct AI-DPC strategies for the DFIG's Rotor Side Converter (RSC): Fuzzy Hysteresis DPC (FH-DPC), Neural Hysteresis DPC (NH-DPC), Prediction Neural Network DPC (PNN-DPC), and Classification Neural Network DPC (CNN-DPC). Additional intelligent controllers were developed for other components, specifically Fuzzy Logic-DPC for the DFIG's Grid Side Converter (GSC) and Fuzzy-MPPT for the PV system, alongside a rule-based Energy Management System (EMS) for the microgrid. The developed AI-DPC strategies for the DFIG-RSC demonstrated substantial improvements over C-DPC, achieving significant reductions in power ripples and stator current Total Harmonic Distortion (THD), with CNN-DPC proving particularly effective. Simulations of the complete AI-controlled DC microgrid (DFIG, PV, battery, fuel cell) under dynamic conditions validated robust performance. The EMS effectively managed power flow, maintained DC bus stability, ensured battery health, and maximized renewable energy utilization. This research offers validated AI-driven solutions, enhancing DFIG performance and demonstrating effective design and control of an integrated DC microgrid, thereby advancing sustainable energy systems.

Keywords: DC Microgrid; Doubly-Fed Induction Generator (DFIG); Artificial Intelligence (AI); Power Quality; Direct Power Control (DPC); Energy Management System (EMS); Renewable Energy.

Résumé

Le passage mondial aux énergies renouvelables, en particulier l'énergie éolienne via les générateurs à induction à alimentation double (DFIG), est entravé par les problèmes de qualité de l'énergie inhérents aux méthodes de contrôle classiques telles que le contrôle conventionnel direct de la puissance (C-DPC), qui présentent une ondulation importante de la puissance et une distorsion harmonique élevée. Cette thèse aborde ces questions en développant et en validant de nouvelles stratégies de contrôle basées sur l'intelligence artificielle (IA) pour les DFIG et leur intégration dans un micro-réseau DC complet. Les principaux objectifs comprenaient la modélisation des composants du micro-réseau (WT-DFIG, PV, BESS, FC), l'évaluation critique du contrôle DFIG classique et la conception de quatre stratégies AI-DPC distinctes pour le convertisseur côté rotor (RSC) du DFIG : Fuzzy Hysteresis DPC (FH-DPC), Neural Hysteresis DPC (NH-DPC), Prediction Neural Network DPC (PNN-DPC) et Classification Neural Network DPC (CNN-DPC). D'autres contrôleurs intelligents ont été développés pour d'autres composants, en particulier le Fuzzy Logic-DPC pour le convertisseur côté réseau (GSC) du DFIG et le Fuzzy-MPPT pour le système PV, ainsi qu'un système de gestion de l'énergie (EMS) basé sur des règles pour le micro-réseau. Les stratégies AI-DPC développées pour le DFIG-RSC ont démontré des améliorations substantielles par rapport au C-DPC, réalisant des réductions significatives des ondulations de puissance et de la distorsion harmonique totale (THD) du courant du stator, le CNN-DPC s'avérant particulièrement efficace. Les simulations du micro-réseau CC complet contrôlé par l'IA (DFIG, PV, batterie, pile à combustible) dans des conditions dynamiques ont validé des performances robustes. Le SGE a géré efficacement le flux d'énergie, maintenu la stabilité du bus CC, assuré la santé de la batterie et maximisé l'utilisation des énergies renouvelables. Cette recherche offre des solutions validées basées sur l'IA, améliorant les performances du DFIG et démontrant une conception et un contrôle efficaces d'un micro-réseau CC intégré, faisant ainsi progresser les systèmes énergétiques durables.

Mots-clés : Mots-clés : Micro-réseau CC ; générateur à induction à double alimentation (DFIG) ; intelligence artificielle (IA) ; qualité de l'énergie ; contrôle direct de la puissance (DPC) ; système de gestion de l'énergie (EMS) ; énergie renouvelable.

ملخص

إن التحول العالمي نحو الطاقة المتجددة، ولا سيما طاقة الرياح من خلال المولدات الحثية مزدوجة التغذية (WT-DFIG)، يواجه تحديات تتعلق بجودة الطاقة، نتيجة للقصور في طرق التحكم التقليدية مثل التحكم المباشر بالطاقة التقليدي، والتي تُظهر تموجات طاقة كبيرة وتشوهًا عاليًا في التوافقيات. تتناول هذه الرسالة هذه الإشكالات من خلال تطوير وتقييم استراتيجيات تحكم جديدة تعتمد على الذكاء الاصطناعي للمولدات، ودمجها ضمن شبكة ميكروية تيار مستمر متكاملة. شملت الأهداف الأساسية نمذجة مكونات الشبكة المصغّرة (طاقة الرياح من خلال المولدات الحثية مزدوجة التغذية -طاقة رياح، الطاقة الشمسية ، نظام تخزين الطاقة بالبطاريات ، خلية الوقود)، وتقييم التحكم الكلاسيكي في WT-DFIG بشكل نقدي، وتصميم أربع استراتيجيات تحكم ذكية متميزة للتحكم في محول جانب الدوّار للمولد، وهي: التحكم المباشر باستخدام المنطق الضبابي لهستيري (FH-DPC)، التحكم الهستيري باستخدام الشبكات العصبية (NH-DPC)، التحكم التنبؤي باستخدام الشبكة العصبية (PNN-DPC)، والتحكم التصنيفي باستخدام الشبكة العصبية (CNN-DPC). كما تم تطوير متحكمات ذكية إضافية لمكونات أخرى، مثل متحكم المنطق الضبابي للتحكم المباشر بالطاقة لمحول جانب الشبكة فيWT-DFIG، ونظام تعقب نقطة القدرة القصوى بالمنطق الضبابي لنظام الطاقة الشمسية ، إلى جانب نظام إدارة طاقة قائم على القواعد. أظهرت استراتيجيات التحكم الذكية المقترحة لمحولات جانب الدوّار للمولد تحسنًا ملحوظًا مقارنة بـ تحكم التقليدي من حيث تقليل تموجات الطاقة والتشوه التوافقي الكلي لتيار الجزء الثابت، حيث أثبتت CNN-DPC فاعلية كبيرة بشكل خاص. وقد أثبتت المحاكاة الخاصة بالشبكة المصغّرة التي تعمل كليًا بالتحكم الذكي تحت ظروف تشغيل ديناميكية كفاءة واستقرار الأداء. أدار نظام إدارة طاقة تدفق الطاقة بكفاءة، وحافظ على استقرار ناقل التيار المستمر، وضمان صحة البطارية، وزيادة الاستفادة من مصادر الطاقة المتجددة. تقدم هذه الأطروحة حلولًا عملية قائمة على الذكاء الاصطناعي، تعزز أداء مولدات DFIG، وتُظهر فاعلية التصميم والتحكم في الشبكات المصغّرة المعتمدة على التيار المستمر، مما يسهم في تعزيز أنظمة الطاقة المستدامة.

الكلمات المفتاحية: شبكة مصغرة تيار مستمر؛ مولد حثي مزدوج التغذية؛ الذكاء الاصطناعي؛ جودة القدرة؛ التحكم المباشر في القدرة؛ نظام إدارة الطاقة ؛ الطاقة المتجددة.